Title
Mixed Conduction in Rare-Earth Phosphates

Author
Ray, Hannah Leung

Publication Date
2012

Peer reviewed|Thesis/dissertation

Mixed Conduction in Rare-Earth Phosphates

by

Hannah Leung Ray

A dissertation submitted in partial satisfaction of the

requirements for the degree of

Doctor of Philosophy

in

Engineering - Materials Science and Engineering

in the

Graduate Division

of the

University of California, Berkeley

Committee in charge:
Professor Lutgard C. De Jonghe, Chair
Professor Mark D. Asta
Professor Jeffrey A. Reimer

Fall 2012

Abstract

Mixed Conduction in Rare-Earth Phosphates

by
Hannah Leung Ray

Doctor of Philosophy in Materials Science and Engineering
University of California, Berkeley

Professor Lutgard C. De Jonghe, Chair

The goal of this work is to gain a better fundamental understanding of mixed electronic and protonic conduction in rare earth phosphates. Specifically, the controlled introduction of a small amount of electronic conductivity is found to enhance the proton conductivity of the (La,Ce) orthophosphates. This discovery could change the way that materials for electrolyte applications are designed.

Rare earth orthophosphates for the past 20 years have been investigated for their applications as intermediate temperature fuel cell electrolytes. They are known to conduct protons, electron-holes, and oxygen vacancies, under different conditions. The rare earth phosphates are tunable in many different ways. The materials can be aliovalently doped; their metal to phosphorous ratio can be varied; and using different synthesis methods can have a large effect on their conduction properties. In addition, the (La,Ce) orthophosphates are an ideal model system for investigating mixed conduction. Systematically varying the Ce content tunes the contribution of electronic component of the total conduction.

In this work, the defect chemistry of the system is discussed; several synthesis methods for the rare earth phosphate compositions are carried out; different methods for identifying the dominant charge carriers are described; and the effect of increasing the Ce content upon the total conductivity in single atmospheres and in the fuel cell configuration is measured.

Acknowledgements

I would like to thank my family, friends, colleagues, and my advisor. Through them, I learned so much more than classes and research alone could tell me.

First, thank you to Lut for being such a great advisor and for always reminding me of the big picture. Thanks for helping me think through all the problems, big and small, and for giving me a hand or a push whenever I needed it.

Thanks Mark and Jeff for reading this for me, and for useful conversations, encouragement, and advice over the past several years.

Thanks Mom and Dad for being the best role model scientists for me to look up to ever since Day 1.

Jane Young, her sisters, kids and grandkids—the awesomest family. I love you.

Katrina, Jessica, Kat, and Shira—my oldest friends.

The folks at Wes—Joe Bruno, Andrea Roberts, Mike Calter, Manny, Wei, Sarah, Zak.

The folks at NREL—Xiaonan Li, Dro, Talia, Rebecca, Russell, Pearl, Boris, Linda, and the SULI program—thanks for inspiring me to apply for grad school in the first place!

Thanks Nicole, Mona, Lei, Phil, Marca, Joel, Jian, Isaac, Jon, Mike, Ruigang, Guojing, Nana, Grace, Aaron, Gabe, Joe, James, Tal, Kinson, Natascha, Bernd, Martin, David, Chris, Virat, Rachel, Que Anh, Yash, Kevin, Tommy, Jerome, Albert, Roh, Fatima, Naomi, Liz, Jesse, Doug, Franklin, Jodi, Devesh, Kate, Amanda, Christine, and Caterina, and all the folks at LBL, UC Berkeley, and on soccer fields for your support and companionship.

Thanks Pi House folks and Ladies' Night—Leah, Tina, David, Molly, Claire, and T for keeping me from going nuts.

Thank you all for shaping me into the person I am today.

Contents

List of Figures

List of Tables

Chapter 1.

Introduction

1.1 Motivation

The focus of this work will be on the fundamentals of electrochemical diffusion and migration processes in rare-earth phosphate proton conductors: dense ceramic materials first designed for use as fuel cell electrolytes. The rare earth phosphates characterized in this work have low ionic conductivity and therefore would require ultrathin membranes when used in an actual device. Interestingly, the material system allows tuning of mixed ionic and electronic conduction. Unusual enhancements in the proton conductivity are observed for the first time in this study, which may lead to a shift in materials design for fuel cell electrolytes.

The work is funded by the Office of Basic Energy Sciences in the Department of Energy, and is motivated by our interest in helping to address the energy conversion and storage problems faced by the world today. Our reasons for studying electrochemical energy storage, fuel cell devices in particular, and the fundamentals of mixed conduction will be discussed first in this Chapter, followed by an introduction to the rare earth phosphate chemistry, defect equilibria, and transport processes in the material.

1.1.1 Electrochemical Energy Storage and Conversion

There is increasing demand for energy as the global population grows and the human development index rises in emerging economies. Due to concerns about anthropogenic climate change (*1*), there is a real motivation to decrease the carbon intensity of the energy generation that will be added to address this demand. The majority of delivered energy today is produced using fossil fuels: currently only about 3% of the total energy supplied globally is renewable (not including biomass or hydropower). However, the renewable generation capacity is increasing quickly—about half of the new electricity generating capacity installed in recent years has been from renewable additions (*2*).

The fastest growing renewable technologies are the photovoltaic and wind electricity generators, both of which suffer from intermittency. The amount of power delivered by the wind and sun varies by the minute, by the hour, by daily cycles, and by season. Thus, there is always a mismatch between the power supplied and the power needed. When the devices are grid-connected, their intermittency can lead to fluctuations in the frequency and voltage of the entire power system. Today, intermittency is smoothed by injecting power into the grid from spinning reserves: power plants that must be continuously running so that they can generate electricity when called upon. As more intermittent sources are connected to the grid, more spinning reserves are needed to compensate them. The spinning reserves can be powered by renewable sources such as (hydropower) but

they can also be gas turbines or nuclear powered. This makes the carbon footprint of the "renewable" sources nonzero, and it decreases the efficiency of the grid.

One solution to this problem could be in developing large-scale energy storage technologies. Energy storage could be co-sited with wind or solar generation, and could make the power produced there dispatchable. Storage technology could also be stationed at the point of use (distributed generation), which would make construction of additional transmission and distribution infrastructure unnecessary. Energy storage has the potential to improve grid management by providing frequency regulation, balancing services, cold start services, contingency reserves and load leveling (*3*).

This recognized need for energy storage has stimulated interest in many technologies, including compressed air, flywheels, biofuels, hydropower, and electrochemical energy storage and conversion technologies such as photoelectrochemical fuels, supercapacitors, batteries and fuel cells. All of these technologies have distinct advantages and disadvantages for different applications, since their response rates, energy capacity, ability to deep cycle, and other performance properties, are different. A variety of different device characteristics are needed for different grid applications. Storage times from 0.001 to 1000 minutes can be required, and system size from 10kW to 100MW can be required for different applications. A good discussion of the technical and economic considerations for electrical energy storage can be found in Ref. (*3*).

The particular electrochemical conversion device of interest to this work is the fuel cell. Fuel cells have been used for grid applications before. They can respond quickly enough to correct rapid fluctuations in electricity demand or supply and regulate frequency. They can be used for distributed energy storage, load shifting, substation grid support, or voltage transient support, depending on the system size (25-200 kW) (kW to MW) (1-100MW) (*3*). Fuel cells can be improved by further materials research into electrolyte materials that can operate in the temperature range 300-600°C, a range that could reduce catalyst cost and enable the use of fuels other than hydrogen.

1.1.2 Fuel Cells

A fuel cell is a device that converts the Gibbs free energy of an electrochemical reaction into electricity. The reagents for the electrochemical reaction are generally oxygen gas and a fuel of some type: hydrogen gas is the most common fuel, but natural gas, diesel, and simple alcohols can also be used. The products of the reaction are water and, if the fuel contains carbon, carbon dioxide. The chemical fuels are not stored within the fuel cell: they must be flowed continuously into the device during operation. As shown in Equation 1.1, the chemical driving force for the production of energy is given by the Gibbs free energy for the reaction,

(1.1) $\Delta G = \Delta H - T\Delta S$

Where ΔG is the standard Gibbs free energy change, ΔH is the standard enthalpy change, and ΔS is the standard entropy change for the combustion reaction of the fuel (*4*).

The fuel cell decouples the oxidation and reduction reactions between two gases by physically separating them with a selective ion-conducting membrane called an electrolyte. The oxidation and reduction half-reactions for each of the reagents occur at the electrodes on either side of the membrane, producing or consuming ions and electrons. The electrons produced at the anode are used to power an external load, then cycled back to the cathode. The ions produced by the redox reaction at one electrode must be transported across the membrane to recombine with the electrons on the other side. The equation that describes the relationship between the chemical and electrical energy is

(1.2) $\Delta G = -nFE^0$

Where n is the number of electrons transferred in the overall, balanced reaction, F is the Faraday constant, and E^0 is the reversible potential for the cell and ΔG is the free energy change for the reaction. (*5*)

Schematics of a few different hydrogen-oxygen fuel cells are shown in Figure 1.2 and the anode, cathode and overall reactions are given by

(1.3) $H_2 \rightarrow 2H^+ + 2e^-$
(1.4) $\frac{1}{2} O_2 + 2H^+ + 2e^- \rightarrow H_2O$
(1.5) $H_2 + \frac{1}{2} O_2 \rightarrow H_2O$

These reactions define the maximum voltage that can be produced from the cell. The theoretical open-circuit potential of a fuel cell, the Nernst potential, is produced at thermodynamic equilibrium, at approaching zero current. At standard temperature T^0=25°C, the Nernst potential is defined by the standard reversible potential for the chemical reaction, E^0, and the activities of the reactants.

(1.6) $$E_N = E^0 - \frac{RT}{nF} \ln\left(\frac{\Pi(a^{vi}{}_{products})}{\Pi(a^{vi}{}_{reagents})}\right)$$

where E_N is the open-circuit potential, E^0 is the standard potential for the reaction given by Eq. 1.2, R is the gas constant, T is the temperature in Kelvin, n is the number of electrons transferred, F is the Faraday constant, a is the activity of the reactive species, and v_i is the stoichiometric coefficient in the balanced chemical reaction.

At an arbitrary temperature, T, E^0 must be replaced by E_T

(1.7) $$E_T = E^0 + \frac{\Delta S}{nF}(T - T_0)$$

Where ΔS is the entropy change for the chemical reaction. For a hydrogen-oxygen fuel cell operating at 600°C, the Nernst potential is about 1.1 V. Thus, the maximum voltage obtainable from a single fuel cell can be derived from simple accounting of the concentrations of the chemical reactants and their free energy content. (*5*)

1.1.2.1 Fuel cell efficiency

One reason for choosing to use fuel cells for energy conversion is their high theoretical efficiency (ε). The efficiency of a conversion process is given by the amount of useful energy extracted from the process divided by the total energy evolved.

(1.8) ε = useful energy / total energy

Fuel cells extract useful energy from a chemical reaction. The total energy evolved from a chemical reaction is the enthalpy, ΔH. The amount of useful energy evolved (the maximum work), is given by the Gibbs free energy change, ΔG. Thus, the reversible efficiency of a fuel cell must be given by

(1.9) $\varepsilon = \Delta G/\Delta H$

For a hydrogen-oxygen fuel cell operating at room temperature, this gives a maximum efficiency of about 83%.

In contrast, the maximum theoretical efficiency of a heat engine is given by the Carnot equation,

(1.10) $\varepsilon = (T_H - T_L)/T_H$

Where T_H is the maximum temperature of the heat engine and T_L is the rejection temperature of the heat engine. For a heat engine operating at 400°C and rejecting heat at 50°C, the maximum reversible efficiency is 52%. The Carnot efficiency increases as the temperature increases, while the efficiency of the fuel cell decreases with temperature. (*5*)

The real efficiency of a fuel cell will always be lower than the theoretical efficiency due to parasitic voltage losses. The usual sources of these voltage losses are electrode activation losses due to electrochemical reactions, ohmic losses due to ionic and electronic conduction, and concentration losses due to mass transport. Different types of voltage losses dominate at different current densities. This is illustrated in an i-V curve for a generic fuel cell, Figure 1.1. In the present work, the test material is the electrolyte, and this is the limiting factor in the cell design. The i-V curves measured in this work are therefore dominated by ohmic losses from the very resistive electrolyte material. In many of the samples that will be discussed here, further voltage is lost through an internal leakage current—electrons transferring through the electrolyte rather than doing work in the external circuit. However, for reasons that will be discussed in Chapter 5, this loss in efficiency could lead to an interesting increase in power output.

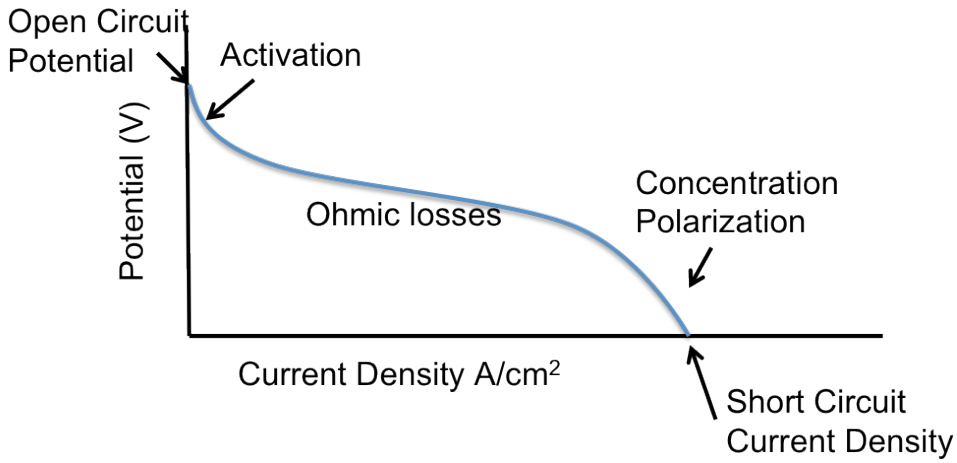

Figure 1.1. Current-Voltage curve for a generic fuel cell. The voltage of the cell decreases with increasing current density due to parasitic voltage losses. The sources of these losses are activation of electrode processes, resistive drops in the electrolyte, and concentration polarization due to mass-transfer processes.

1.1.2.2 Fuel cell types

There are five major types of fuel cells, and they are classified by their electrolytes: phosphoric acid fuel cells (PAFC), polymer electrolyte membrane fuel cells (PEMFC), alkaline fuel cells (AFC), molten carbonate fuel cells (MCFC), and solid oxide fuel cells (SOFC). The electrolyte membrane discussed in this work is new type: a solid-state proton-conducting electrolyte (PCFC). The properties of these different types of fuel cell are listed in Table 1.

	PEMFC	PAFC	AFC	MCFC	SOFC	PCFC
Electrolyte	Polymer membrane	Liquid H_3PO_4 (immobilized)	Liquid KOH (immobilized)	Molten carbonate	Ceramic	Ceramic
Charge Carrier	H_3O^+	H_3O^+	OH^-	CO_3^{2-}	O^{2-}	H^+
Operating temperature	80C	200C	60-220C	650C	600-1000C	300-600C
Catalyst	Platinum	Platinum	Platinum	Nickel	Perovskites (ceramic)	Under development
Fuel Compatibility	H_2, CH_3OH	H_2	H_2	H_2, CH_4	H_2, CH_4, CO	H_2, CH_4,
Power Density (mW/cm^2)	300-1000	150-300	150-400	100-300	250-350	Under development
Power Range (kW)	0.001-1000	50-1000	1-100	100-100,000	10-100,000	Under development

Table 1.1. Description of major fuel cell types (*5*).

The focus of this work will be on the solid-state proton-conducting membranes: PEMFCs, SOFCs, and the new PCFCs. Unlike the PAFC, AFC, and MCFC electrolytes, these solid-state membranes do not have to be replenished, and are not corrosive. The PEMFCs can have

high power density even at room temperature—they are therefore appropriate for portable applications. Their disadvantages are that they rely on expensive Pt catalysts that are easily poisoned by carbon monoxide and sulfur, and that the whole system requires water management in order to keep the membrane moist. The SOFCs are attractive because they operate at high temperature and thus can use many different fuels, non-Pt catalysts, and the waste heat can be used for combined heat and power applications if the cells are sited at the point of use. The main disadvantages of SOFCs are related to high temperature materials issues: the entire device, the gas seals, and the balance of plant must all be compatible with high-temperature operation.

Proton conducting ceramics designed for use as PCFC electrolytes combine the advantages of the SOFC and PEMFC membrane materials while removing many of the disadvantages. Unlike PEMs, PCs are dense ceramics and do not rely on water for transport. This eliminates the need for water management and operation at temperatures <100°C. Instead, protons are incorporated into the ceramics as interstitial-like defects, and move through the sample by making and breaking hydrogen bonds with oxygen. While SOFCs depend on oxide ion transport, which usually requires operating temperatures over 800°C, the lower activation energy for proton transport allows operation at intermediate temperatures (300-600°C). Operation at these temperatures would enable the use of non-noble metal catalysts in each device, as well as stainless steel and cheaper gasket materials in the fuel cell plant. In addition, since protons are transported from anode to cathode in PC fuel cells, water forms on the oxygen side of the membrane and the fuel is not diluted as in SOFCs (*6*). This is pictured in Figure 1.2. Examples of common ceramic proton conducting materials are the perovskites $BaZrO_3$ $BaCeO_3$, and $SrCeO_3$ (*7*), and the solid acid $CsHSO_4$ (*8*). However, our project has focused on the rare earth phosphates $LaPO_4$ and $CePO_4$ with the monazite structure.

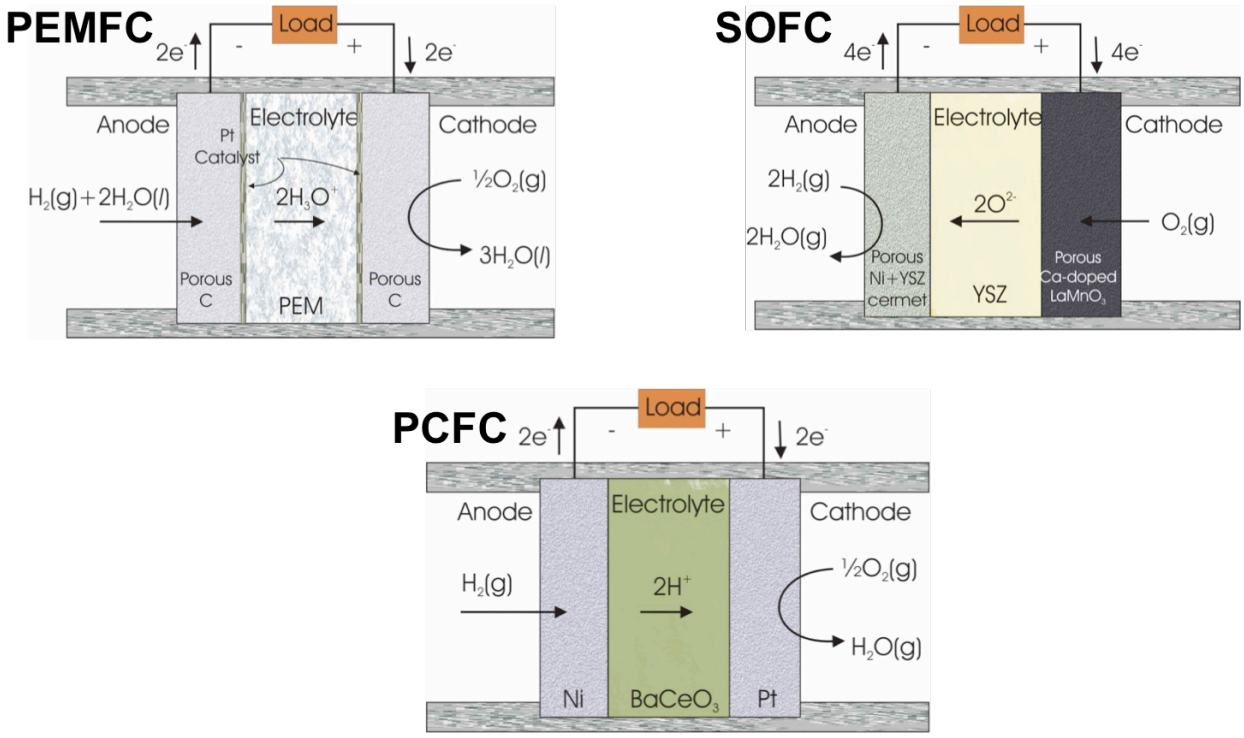

Figure 1.2. A comparison of the conductive species and locations of the reagents and products of the hydrogen oxidation reaction for PEM, SOFC, and PCFC fuel cells. Water dilutes the fuel in both PEMFCs and SOFCs, but does not in PCFCs.

1.1.3 Fundamentals of mixed conduction

Our final motivation for this work is to develop a more fundamental understanding of the effects of mixed conduction in a material. Mixed conduction occurs when two or more different types of charge carrier simultaneously move in a material. Mixed ionic and electronic conducting materials (MIEC) are used for many applications such as fuel cell electrodes, fuel cell electrolytes, battery electrodes, catalysts, gas separation membranes, and chemical sensors.

The simplest question that arises when considering an MIEC is: if there are two different charge carriers moving in a material, do they interact with each other at all, or do they move about as though the other were absent? The follow-up question is: if they do interact, then is the interaction beneficial or detrimental? Possible procedures for addressing these questions can be formulated from either a top-down, general approach, or from a bottom-up, material-specific approach. An example of each approach is briefly presented here.

The most general formulation of the MIEC problem can be taken from the equations of irreversible thermodynamics given by Onsager. For a system that contains only one mobile charged species x, the flux the species J_x is driven by the gradient in electrochemical potential for that species, $\Delta\eta_x$.

(1.11) $J_x = (L_x)\Delta\eta_x$

Where J_x is the flux of species x, L_x is a constant, and $\Delta\eta_x$ is the gradient in electrochemical potential for species x.

When this system is expanded to include two mobile, charged species (ions and electrons, for example), then cross-terms appear in the equations, and the motions become coupled. For example, the gradient in ionic electrochemical potential $\Delta\eta_i$ can drive both the flux of ions J_i and the flux of electrons J_e if the coupling coefficient L_{ie} is nonzero. Onsager (*9*) gives that $L_{ie} = L_{ei}$.

(1.12) $$\begin{pmatrix} J_i \\ J_e \end{pmatrix} = \begin{pmatrix} L_{ii} & L_{ie} \\ L_{ei} & L_{ee} \end{pmatrix} \begin{pmatrix} \Delta\eta_i \\ \Delta\eta_e \end{pmatrix}$$

Thus, the most general question for the MIEC problem becomes simply: are the cross-coefficients for this system zero or nonzero? If they are nonzero, then they could be positive or negative—leading to either an increase or a decrease in flux. Wagner (*10*), Yoo (*11, 12*), Virkar (*13*), and Liu (*14*), have presented transport models that preserve the option of having nonzero cross terms. However, direct measurement of these cross terms is nontrivial.

A bottom-up formulation of the MIEC problem gives a specific hypothesis as to the nature of the possible carrier interactions. In materials that are aliovalently doped, there can be an attraction between the dopant and the charge carriers. This dopant association can depress the charge carrier conductivity. Introduction of a second charge carrier could conceivably relax the charge carrier-dopant attraction and lead to an increase in conductivity. First-principles modeling work is currently being carried out by our group that quantifies the possible decrease in activation energy that could be obtained from this type of interaction (*15*).

Charge carrier interaction is critical for the entire family of proton-conducting ceramics. For reasons that will be discussed in Sections 1.3-1.4 on defect chemistry, these materials can all become mixed conductors upon equilibration with the correct gaseous atmosphere. Recently, several studies have been carried out that highlight mixed conduction in the perovskite proton conductors. Yoo et al. observed that two diffusion coefficients were necessary to model transient behavior of hydration and dehydration (*12*). Sanders et al. carried out steam permeation experiments that demonstrated large conductivity enhancements when the contributions of protons, holes, and oxygen vacancies to the total flux was varied (*16*). Virkar et al. reported that a mixed conductor might have better stability than a purely ionic conductor due to reduced interfacial polarization (*17*). Various transport models have been proposed for these systems, but none are general enough to fit all proton-conducting materials. It is important that this phenomenon of mixed conduction be better understood in these materials, because carrier interactionos could lead to power enhancements, flux enhancements, and as-yet unimagined applications.

In this work, mixed protonic and electronic conduction is investigated using ac impedance, dc chronoamperometry, and i-V curves in the fuel cell configuration, on a material for which the electronic contribution to the current is tunable. This rare earth phosphate material system is introduced next.

1.2 Material System: Rare Earth Phosphates

The materials under investigation in this work are the rare earth phosphates. The fundamental formula unit of these materials is a metal cation coordinated to a phosphate anion $[PO_4]^{3-}$. In the phosphate anion, the P is in a pentavalent state. The anion takes on a tetrahedral shape, with four P-O σ bonds forming via sp^3 hybridization, and a small contribution from π bonding (*18*). In the metal phosphate materials, as the phosphorous to metal ratio increases, the phosphate tetrahedra can condense to form P-O-P bridging bonds, connecting two or more tetrahedra. Figure 1.3 shows some ball and stick models of several metal phosphates that have different metal to phosphate ratios. In the orthophosphate, the metal cation is coordinated to an isolated phosphate tetrahedron. As the phosphorous content of the material increases, the phosphate tetrahedra condense to form $[P_2O_7]^{4-}$ links, then long interconnected chains of tetrahedra. Thus, the chemistry of the rare earth phosphates is very flexible. They can take on variety of possible crystalline and amorphous structures. If these structures are carefully tuned, then the relationship between structure and conduction properties can be determined. However, different processing methods must be used to obtain the different structures, and these processes often change the microstructures of the phosphates. This will be discussed in detail in Chapter 2. The rare earth orthophosphates were found to be the most stable, easily processed, and reproducible; thus, these were the focus of the electrochemical measurements described in Chapters 3-5.

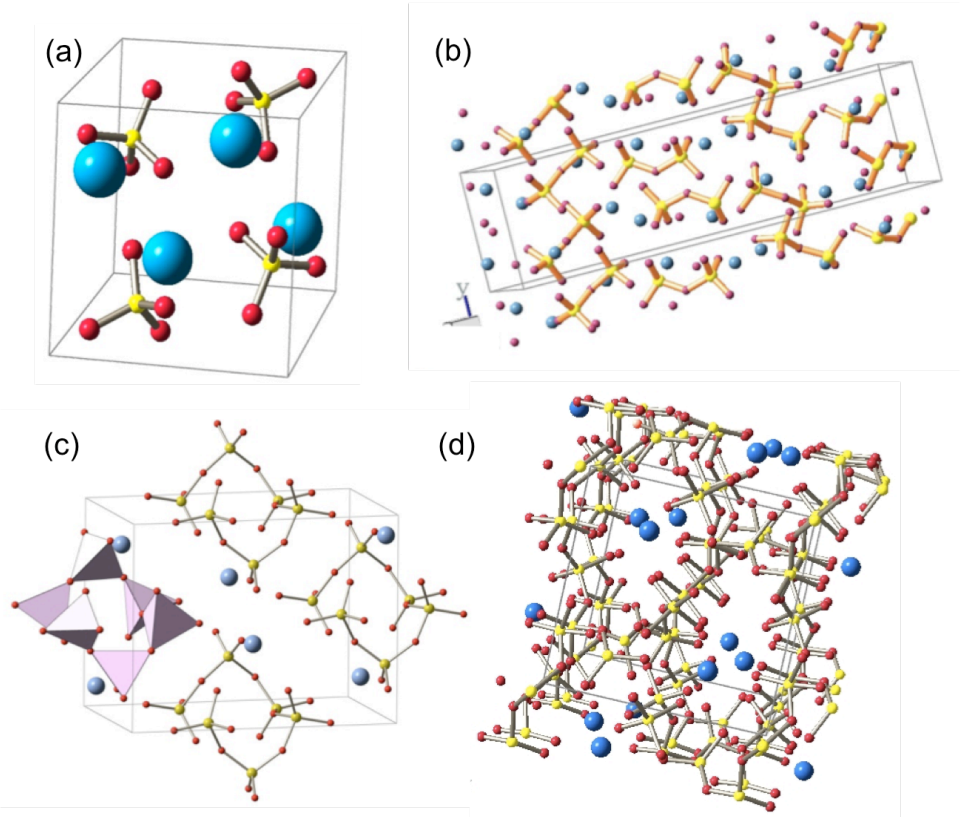

Figure 1.3. The metal phosphates can take on many configurations. As the metal to phosphate ratio decreases, the connectivity of the phosphate tetrahedra increases. (a) Monazite orthophosphates have isolated phosphate tetrahedra. (b) Calcium pyrophosphates have the P_2O_7 anion of two condensed phosphate tetrahedra. (c) The orthorhombic lanthanum metaphosphate and (d) ultraphosphate both show very long chains of phosphate tetrahedral, linked via pyrophosphate bonds in which an oxygen is shared with a neighboring tetrahedron.

The rare earth orthophosphates are attractive materials for fuel cell electrolytes because they are thermodynamically stable, with a melting temperature over 2000°C; they are also chemically inert, stable to CO_2 (*19*) abundant, nontoxic, and, most importantly, proton conducting. Norby and Christiansen (*20*) were the first to report proton conduction in lanthanum orthophosphates in 1995. The highest conductivity reported in this paper was moderate: only $3x10^{-4}$ S/cm for Sr-doped $LaPO_4$ in wet air at 800°C. However, this finding led to a surge of interest in the rare earth phosphates. Kitamura and Amezawa (*21-24*) carried out in-depth studies of doped $LaPO_4$, $CePO_4$, and LaP_3O_9. LaP_3O_9 conducted at $5x10^{-4}$ S/cm at 550°C. They recorded the relationship between proton conductivity and oxygen and water partial pressure. Dopant type and doping levels were varied, defect structures investigated, and a defect model proposed. These groups and others used classic powder processing methods as well as glass-ceramic processing methods to obtain dense samples (*25, 26*).

Harley et al. (*6*) recognized that the typical processing conditions used to obtain the samples might lead to amorphous, phosphate-rich grain boundary phases, and that these phases might enhance proton conductivity. Figure 1.4 shows a phase diagram of the La_2O_3-P_2O_5 system. Perfect $LaPO_4$ compositions would have exactly 50% La_2O_3-50% P_2O_5, and

would be stable to very high temperature. However, if excess phosphates were present, then the common sintering treatment at 1200-1400°C would give a mixture of $LaPO_4$ liquid phases, which would solidify into mixtures of $LaPO_4$ and LaP_3O_9, or to $LaPO_4$ and an amorphous grain boundary. Harley et al showed that systematic addition of excess phosphate led to an increase in conductivity. This observation spurred further studies of the role of excess amorphous phases in proton transport. Studies of glassy (*27, 28*) and glass-ceramic (*29-31*) rare earth phosphate compositions were carried out. Proton conductivity was found to increase with increasing phosphorous content, but the stability and reproducibility of the glasses decreased. The highest proton conductivity achieved in these types of materials was $3x10^{-5}$ S/cm at 550°C for ultraphosphate glasses and $2x10^{-5}$ S/cm at 550°C for La metaphosphate glass-ceramics.

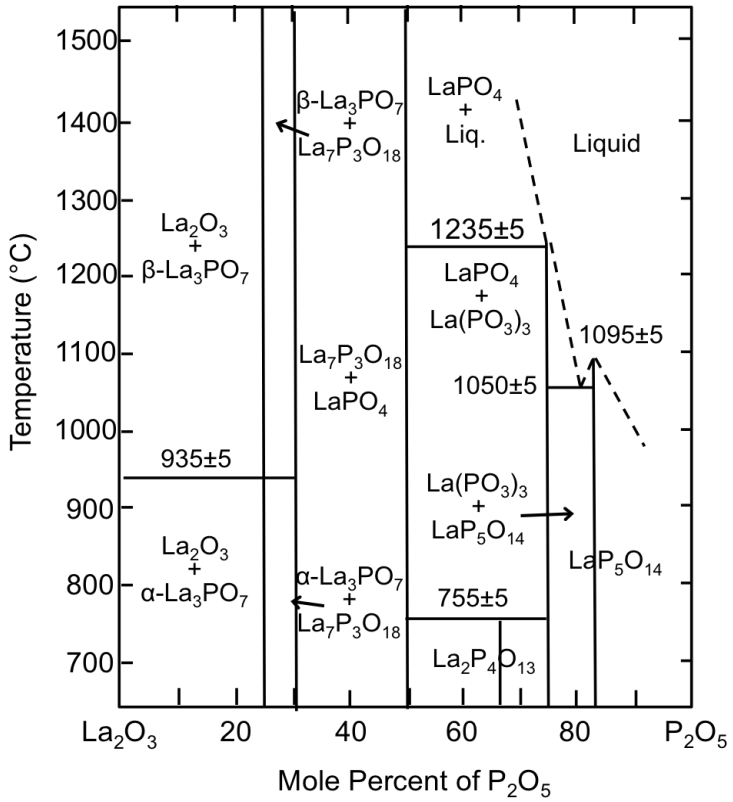

Figure 1.4. Phase diagram of the La_2O_3-P_2O_5 system from Park and Kriedler (*34*). The $LaPO_4$ monazite is a line phase at the 50-50 La-P composition, which has a melting temperature of >2000°C. However, if the composition is slightly off–stoichiometry, liquid phases and metaphosphate phases can form, as will be shown in this study.

Studies of $CePO_4$ have shown that this material under oxidizing conditions dominantly conducts electronically, but is a proton conductor under reducing conditions (*23*). The electronic contribution to the conduction makes it attractive as a hydrogen permeation membrane. Preliminary experiments for this application were carried out and gave H_2 fluxes of $1x10^{-8}$ mol H_2/cm^2 sec, performance similar to the perovskite oxides (*32*). $CePO_4$ is isostructural with $LaPO_4$, but displays very different conduction behavior. This makes possible the study of (La,Ce)PO_4 alloys. One study by Kitamura mixed $La_{0.99}Ce_{0.01}PO_4$ in hopes of finding mixed conductivity, but found that it behaved the same as $LaPO_4$ (*33*).

These differences between $LaPO_4$ and $CePO_4$ can be explained using a defect chemical model for the rare earth phosphates. The model proposed by Kitamura et al is presented in the next section.

1.3 Introduction to Defect Chemistry

The electrical conduction properties of a material are defined by the number and types of mobile, charged, point defects it has. A point defect in a ceramic can be ionic or electronic. Ionic defects occupy lattice atomic positions—they can be vacancies, interstitials, or substitutional ions. Electronic defects create an electron in the conduction band and/or an electron hole in the valence band. These can be highly localized on an atom, representing a valence state change, or they can be delocalized (*35*). The unique chemical composition, bonding, and crystal structure of a material determines the thermodynamic stability of different types of defects within it. In order to understand the electrical behavior of a solid, one must first have a good understanding of its defects.

Point defects can be either intrinsic or extrinsic. Intrinsic defects form in an undoped, pure compound, while extrinsic defects form in response to doping. Intrinsic defects form at temperatures > 0K. Their formation is thermally activated, and favored by entropy. A thermodynamically defined number of intrinsic defects will exist at a given temperature. Extrinsic defects are created by intentionally introducing impurities in to a material. For extrinsic defects, the doping level, rather than the temperature, sets the total concentration of the defects. Doping the material with an aliovalent cation creates a mismatch in charge relative to the perfect lattice and requires charge compensation by extrinsic charged defects (vacancies, interstitials, or electronic defects). The concentration of extrinsic defects usually outweighs that of the intrinsic defects; thus, the extrinsic defects dominate the total conductivity (*36*).

A simple example of extrinsic doping is illustrated in Figure 1.5 for the case of the metal oxide. In the figure, the defects are described using Kroger-Vink notation, which requires a brief explanation. The main body of the notation identifies whether the defect is a vacancy, (V), an ion (A or OH), or an electronic defect (e or h). The subscript identifies the site that the defect occupies: this can be on a normal lattice site (M or O) or an interstitial site (i). Finally, the superscript describes whether the defect is neutral (X), positively (•) or negatively (‘) charged relative to the perfect crystal. In Figure 1.5, the perfect crystal, MO_2, is doped with the aliovalent dopant A_2O_3. Since M is tetravalent and A is trivalent, there arises an effective negative charge A_M’ relative to the perfect lattice. This charge can be compensated by oxygen vacancies, V_O^{**}, electron-holes, h^*, or hydroxyls, OH^*. Note that each defect combination must obey net charge neutrality. Figure 1.5 also shows how the defects might exchange for one another when in contact with different atmospheres (O_2, H_2O, and H_2). The content of the gaseous atmosphere helps to determine the thermodynamic stability of each defect. Since these are equilibrium reactions, several different types of point defect may exist in the material at the same time. Thus, the doping level sets the overall defect concentration, but the material’s interaction with the gaseous atmosphere sets the relative concentrations of oxygen vacancies, electron-holes, and protons.

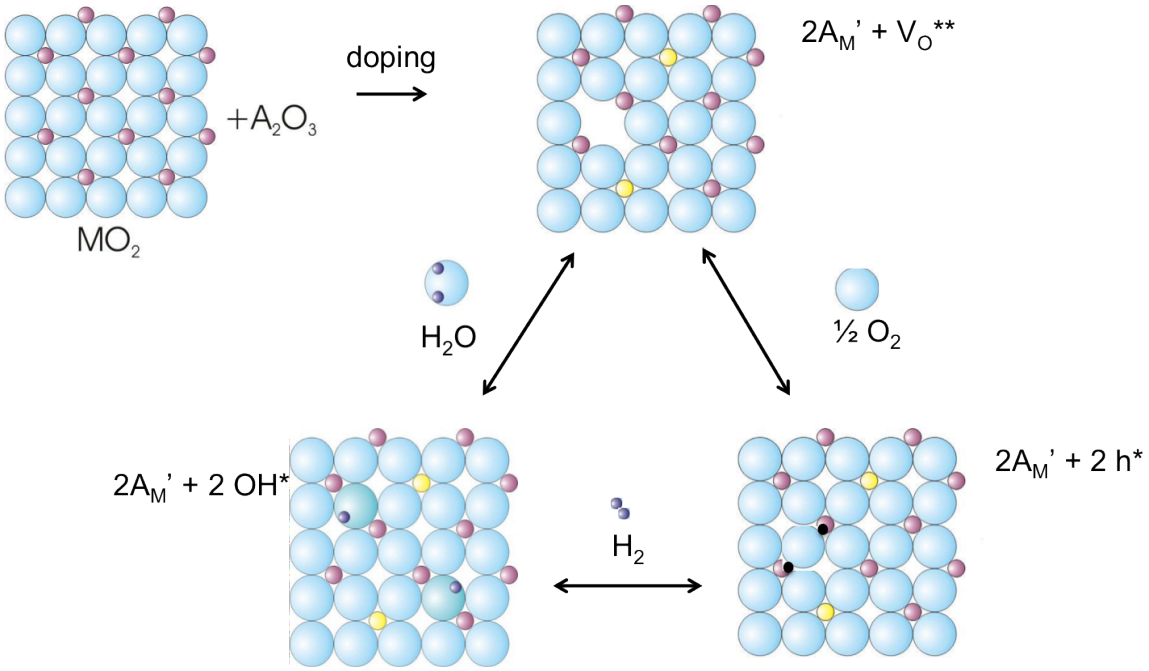

Figure 1.5. An example of extrinsic doping in a metal oxide MO_2 by the aliovalent compound A_2O_3. The dopant introduces an effective negative charge, represented by A_M' that must be compensated by additional defects in order to maintain net charge neutrality. The possible defects are oxygen vacancies, V_O^{**}, electron-holes, h^*, or hydroxyls, OH^*. The doping level sets the overall concentration of defects, but the relative levels of the three types of defect vary depending on the gaseous atmosphere. Images from (*37*).

After understanding the defect chemistry of the simple oxide system, we can now look at the similar, but slightly more complex orthophosphate materials. For this defect system, the model proposed by Kitamura is followed. In $LaPO_4$, replacing a La^{3+} cation with a divalent Sr^{2+} cation results in an effective negative charge, Sr_{La}'. This charge is compensated by the same types of defects as in the oxide system: oxygen vacancies, electron-holes, and protons. However, the defects are structurally different from those in the simple oxide. Figure 1.6 shows the exchanges between the different types of defects for the phosphate system. Here, an oxygen vacancy manifests itself as a pyrophosphate link: two phosphate tetrahedra, $2[PO_4]^{3-}$, lose an O and condense to form a $[P_2O_7]^{4-}$ anion. Protons bond to the oxygen corners of the phosphate tetrahedra: the protonic defect can be represented as hydrogen phosphate, $[HPO_4]^{2-}$. Finally, p-type electronic charge carriers can charge-compensate the dopant. These are incorporated into the valence band, or, if they are highly localized, they create a split-off band.

Now that the concept of defects in the rare earth phosphate system has been illustrated, the rigorous defect model can be discussed.

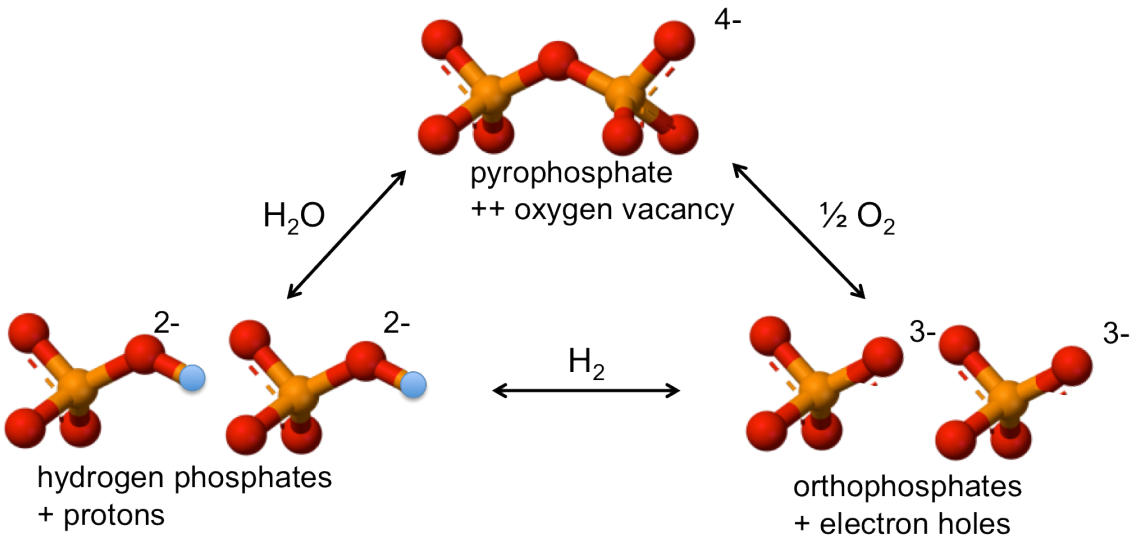

Figure 1.6. Defect chemistry of rare earth phosphates. Depending on the H_2O, O_2, and H_2 content of the atmosphere, pyrophosphate defects, hydrogen phosphate defects, and orthophosphates with associated electron-holes can exchange for each other.

1.4 Rare Earth Phosphate Defect Model

The defect model discussed here and pictured in the previous section follows the work of Amezawa and Kitamura (*21, 23*). These groups observed the structural defects that appeared in doped $LaPO_4$ upon exposure to dry, oxidizing conditions (air); wet, oxidizing conditions (humidified air); and wet, reducing conditions (humidified hydrogen). By comparing deviations in the structures to undoped $LaPO_4$ samples, they proposed the defect chemical model given by Equations 13-16. As must any full defect chemical model, this system of defect equilibria obeys the laws of mass balance, charge balance, and site ratio balance.

(1.13) $$2SrHPO_4 \xrightarrow{LaPO_4} (P_2O_7)^{\cdot\cdot}_{2PO_4} + 2Sr'_{La} + H_2O$$

(1.14) $$(P_2O_7)^{\cdot\cdot}_{2PO_4} + H_2O_{(g)} \leftrightarrow 2(HPO_4)^{\cdot}_{PO_4}$$

(1.15) $$\tfrac{1}{2}O_2 + 2(HPO_4)^{\cdot}_{PO_4} \leftrightarrow 2(PO_4)^{X}_{PO_4} + H_2O + 2h^{\cdot}$$

(1.16) $$(P_2O_7)^{\cdot\cdot}_{2PO_4} + \tfrac{1}{2}O_2 \leftrightarrow 2h^{\cdot} + 2(PO_4)^{X}_{PO_4}$$

Equation 1.13 states that doping the pure $LaPO_4$ crystal with $SrHPO_4$ creates the effective negatively charge Sr_{La}'. Since the materials are synthesized in dry, oxidizing conditions, the first extrinsic charge compensating defect is the pyrophosphate species, $[P_2O_7]^{4-}$. Note that in the Kroger-Vink notation used for the defect model, this species has a 2+ effective charge, just like an oxygen vacancy defect in the MO_2 oxides. This is because the 4- charged

pyrophosphate occupies two phosphate sites that in the perfect crystal would together have a 6- charge.

The next three defect equilibria show how the oxygen vacancies, protons, and electron-holes can exchange with each other when water and oxygen are present in the gaseous atmosphere. Note that all of these reactions are equilibrium reactions—they are reversible and can be driven to the left or the right depending on the partial pressures of oxygen and water in the atmosphere.

Equation 1.14 shows the hydration of a pyrophosphate defect. Water adds to a pyrophosphate defect $[P_2O_7]_{2PO4}^{**}$ to form two protonated phosphate tetrahedra: two $[HPO_4]^{2-}$ species sited on two $[PO_4]^{3-}$ sites. This gives an effectively positive charged species, $[HPO_4]_{PO4}^{*}$.

Equation 1.15 shows the exchange between a protonic and an electronic defect. If the hydrated sample is exposed at high temperature to dry, oxidizing conditions, then $[HPO_4]_{PO4}^{*}$ can interact with oxygen to form water and introduce a p-type charge carrier, h^{*}. Note that in these equilibria, the location of the p-type electronic defect h^{*} is not specified; depending on the cation type present in the material, this hole can be delocalized, or it can be localized on a Ce cation. This will be discussed further in Section 1.5.3.

Equation 1.16 shows that exchange between oxygen vacancies $[P_2O_7]_{2PO4}^{**}$ and p-type electronic carriers is also possible. At high pressures of oxygen, the pyrophosphate defect can be oxidized back to two phosphate tetrahedra with the incorporation of h^{*}.

Equivalent defect equilibria are possible under reducing conditions, but these require interaction with H_2O/H_2. Exchanges between electron-holes and oxygen vacances, and electron-holes and protonic defects are expressed in Equations 1.17-1.18.

(1.17) $$h^{\bullet} + (PO_4)_{PO_4}^{X} + \tfrac{1}{2}H_2 \leftrightarrow \tfrac{1}{2}(P_2O_7)_{2PO_4}^{\bullet\bullet} + \tfrac{1}{2}H_2O$$

(1.18) $$h^{\bullet} + (PO_4)_{PO_4}^{X} + \tfrac{1}{2}H_2 \leftrightarrow (HPO_4)_{PO_4}^{\bullet}$$

Having the defect equilibria in the form of balanced chemical reactions is useful because these can translate into a system of equations that can give quantifiable values for defect concentrations and equilibrium constants of reactions. For example, Equation 1.14 would become

(1.19) $$K_1 = \frac{[(HPO_4)_{PO_4}^{\bullet}]^2}{pH_2O \times [(P_2O_7)_{2PO_4}^{\bullet\bullet}]}$$

Where species in brackets denote concentrations of the charge carrier, and *p* denotes the partial pressure. If the entire system of equations is solved, then the obtained values can then be plotted in a Brouwer diagram where the relative defect concentrations are plotted

vs. pH_2O or pO_2. Measurement of the equilibrium constants and defect concentrations turns out to be nontrivial. In Chapter 3, we will discuss how transient dc chronoamperometry measurements can be used to probe these equilibria qualitatively, but that it is difficult to calculate the entire set of equilibrium constants. However, these quantities can be calculated from first principles; this is ongoing work in our group (*38*).

1.5 Defect Transport

Now that the defect equilibria for this model have been discussed, we consider the mechanism for transport of these defects in the orthophosphate system.

1.5.1 Oxygen vacancy conduction

In the rare earth phosphate materials, oxygen vacancy conduction is thought to have a minor contribution to the total current. Since the oxygen vacancy is actually a pyrophosphate link, and the pyrophosphates are very stable complexes, their activation energy for movement is high. When compared to the protonic and electronic conduction in an ac impedance or dc chronoamperometry measurement, the oxygen vacancy conduction will be negligible. In all of the conduction experiments carried out in this work, the oxygen contribution will be assumed to be zero.

However, when equilibrated over very long periods of time (weeks) with hydrogen gas, it has been experimentally observed that the structural (Raman) signals for pyrophosphate do shrink and disappear. The pyrophosphates must be mobile to some extent, since they are eventually replaced by other defects. The slowness of the exchange makes it difficult to estimate carrier concentrations for the other charge carriers. For example, if the oxygen vacancy defect is frozen in it restricts proton incorporation in the samples. This is an added complication that must be considered in the analysis.

1.5.2 Proton conduction

The mechanism for proton conduction in lanthanum orthophosphates is now better understood due to first-principles modeling. As described in the defect model, protons in $LaPO_4$ are hydrogen-bonded to oxygen corners of the phosphate tetrahedra. The proton hops from oxygen to oxygen, transferring between different tetrahedra. This pathway is depicted in Figure 1.7, a series of images calculated using density functional theory and the nudged elastic band technique (*39, 40*). A successful proton hop requires the initial O-H site and the O corner of the adjacent phosphate tetrahedron to move close enough together for the hydrogen bond to transfer. Thus, several molecular motions are required for protons to move: oscillations of the O-H bonds, rotations of the tetrahedra, and transfer of the hydrogen bond from one oxygen to the next. The activation barrier for this process ranges between 0.68-0.80eV depending on the direction of the proton movement in this highly asymmetric unit cell.
Discrepancies between the calculated activation energies and the experimentally measured energies (generally 1-1.1 eV) are attributed to proton-dopant association. Further first-

principles studies by our group have shown that protonic carriers can be electronically "trapped" by the effective negative charge density surrounding a dopant site (*41*). Escaping this electronic attraction adds ~0.2eV to the activation energy barrier.

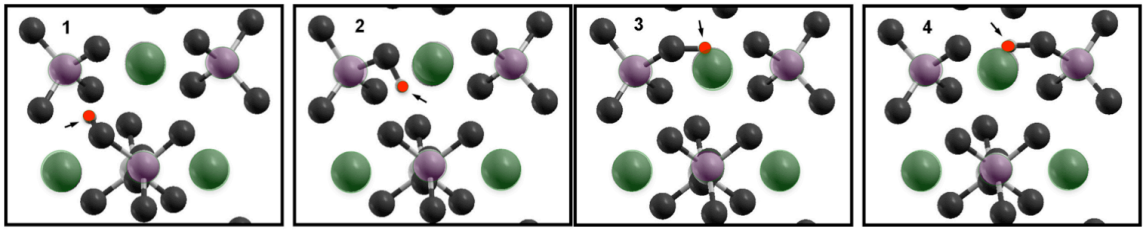

Figure 1.7. Proton transport in $LaPO_4$. The La^{3+} cations are pictured in green, the phosphorous in purple, the oxygen grey, and the protons in red. This figure is a series of snapshots of the proton's path through a $LaPO_4$ crystal from the NEB model proposed in (*39*). The proton moves through the system via intertetrahedral hops aided by slight rotations of the tetrahedra.

1.5.3 Hole Conduction

Electronic conduction in the rare earth phosphates is experimentally measured to be p-type (*42*), and occurs via different mechanisms depending on the cations present in the material. Electronic conduction in $LaPO_4$ is extremely low and only dominates the total conduction at high temperatures in dry, oxidizing conditions. This is thought to be because the band gap of $LaPO_4$ is ~ 4 eV, and the creation of electronic defects unfavorable. In contrast, when a critical amount of Ce is introduced into the material, electronic conduction begins to dominate. As will be discussed at length in Chapter 4, the electronic contribution to the total conductivity begins to vary in a predictable manner with the Ce concentration above this critical threshold.

The increased stability of the electron-hole in Ce-containing samples is attributed to the ability of the Ce cation to exist in either the 3+ or the 4+ valence state. When Ce is in the 3+ state, it retains a lone 4f electron in its valence band. A first-principles calculation of the $CePO_4$ band structures reveals that this 4f electron state is highly localized (*43*). Therefore, the electron-hole's transport mechanism is thought to be small-polaron hopping between Ce^{3+} cation sites. Small-polaron hopping is a transport mechanism for localized/correlated electrons commonly seen in transition metal oxides. It is a thermally activated process, and as will be discussed in Chapters 3 and 4, this is consistent with the Arrhenius behavior in the conductivity experimentally observed.

Thus, protons and holes can be simultaneously present in a material, given the appropriate gaseous environment. Both travel through the sample via a hopping mechanism, and both can be electronically trapped near a dopant (*15*), (*41*). They do not occupy the same sites in the material, but they do exchange for each other. Since the doping level sets the maximum carrier concentration, one additional proton must mean one less hole, in observance of electroneutrality. The final question that is addressed in this work regards how these two charge carriers interact with each other when measured in the fuel cell configuration.

1.5.4 Mixed Conduction

The idea that conductivity enhancements could be found in a mixed conductor was discussed in Section 1.1.3. Now that the rare earth phosphate material and its defect structures have been presented, we can briefly discuss how this idea was addressed in this work. In Chapter 4, we will show that the (La,Ce)PO_4 materials are measured to have electronic conductivity levels that vary in a predictable way. In order to probe the effect of this electronic conductivity on the proton conductivity, a series of membranes with varying levels of Ce were synthesized, and their i-V characteristics in the fuel cell condition were measured. A simple schematic of the experimental setup is shown in Figure 1.8. The membrane separates the hydrogen oxidation and oxygen reduction half-reactions, and the potentiostat measures the external current at various applied voltages.

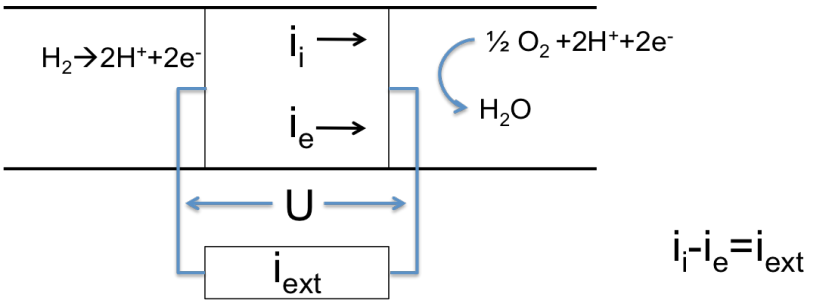

Figure 1.8. Schematic of the fuel cell measurement used to test the mixed conducting samples. In the image, i_i is the ionic current in the membrane, i_e is the electronic leakage current, U is the measured potential, and i_{ext} is the measured external current.

Transport models for ions and electrons in mixed conductors in the fuel cell condition have been presented by several groups (*14, 44, 45*). Much information can be gleaned from a fuel cell i-V curve. As in any dc measurement, the total current measured for the device will always be the sum of the ionic and electronic current. However, when the potential V = E_N, the theoretical Nernst potential, then the driving force for transport of ionic defects should go to zero. Then the current should be purely electronic. Similarly, when the potential V = 0, then the driving force for transport of electronic defects is zero, and the current should be purely ionic. The open-circuit potential (OCV) is also a useful value to track as a function of Ce content. When the current approaches zero, then the steady-state ionic and electronic currents balance, and an estimate of the transference number (the fraction of the current carried by a particular species) can be made from the OCV. This technique and its implications about power and conductivity enhancement will be discussed in Chapter 5.

1.6 Summary

There has been a recent surge in the deployment of renewable electricity generation due to concerns about climate change, energy security, and water resources; government policies that incentivize renewables; the declining costs of renewable technologies; and changes in the prices of fossil fuels. Since many of these generators are intermittent, it is important to concurrently install energy storage technologies to stabilize the grid. Fuel cells are capable of providing several types of ancillary services. Research on proton-conducting ceramics for new fuel cell electrolytes could lead to lower cost, intermediate temperature devices that are fuel flexible.

In the interest of developing new materials for electrochemical energy conversion and storage devices, we are investigating the fundamentals of mixed protonic and electronic conducting rare earth phosphates. The rare earth orthophosphate system is ideal for probing the interactions of protonic and electronic charge carriers, because alloying the (La,Ce)PO_4 materials allows tuning of the electronic conductivity level. An understanding of the defect chemistry, electronic structure, and transport properties of these materials is gained from defect model of Kitamura et al. and first-principles models of proton and hole

electronic structures. The synthesis, microstructure, and electrochemical behavior of the rare earth phosphates are herein described.

Chapter 2 of this work will present the synthesis and microstructural characterization of several types of rare earth phosphates, and the characteristic defects that they display on doping. Chapter 3 will describe the techniques used to identify the charge carriers in the doped $LaPO_4$ and $CePO_4$ materials. Chapter 4 describes microstructural characterization and total conductivity measurements of the series of alloys $La_{0.98-x}Ce_xSr_{0.02}PO_4$. Chapter 5 presents the fuel cell measurements of this series and discusses the interactions of electronic and ionic charge carriers.

Chapter 2.

Synthesis and Microstructural Characterization of Rare Earth Phosphates

This chapter reports on a broad range of characterization methods and materials, a number of which were exploratory only.

Introduction

The rare earth phosphates are a versatile material system that can have a variety of different physical and chemical properties. Phosphates can be tuned in the same way as oxides: by changing the cations, doping, and using various synthesis methods to obtain different microstructures. In addition to this, the metal to phosphorous ratio can be tuned. At low phosphorous contents, the anion is an isolated phosphate tetrahedron coordinated to the metal cation. Increasing the phosphorous content increases the connectivity of the phosphate tetrahedra, creating O-P-O linkages characteristic of pyrophosphates, or more complex species such as phosphate ring structures, and long chains of phosphate tetrahedra that are interconnected in various configurations (*1*). The materials can be thought of to some extent as "inorganic polymers." Recently, much attention has been paid to the rare earth orthophosphates, with the metal to phosphorous ratio M:P = 1:1. Due to their high melting temperatures, optical emissivity, and resistance to corrosion, they are studied for diverse applications such as lasers, scintillators, thermal protection coatings, catalysts, nuclear storage materials, and, of interest to this work, ionic conductors (*2*).

As discussed in Chapter 1, the proton conduction properties of the lanthanum and cerium orthophosphates, and the lanthanum metaphosphates have been studied by Kitamura, Amezawa, and Norby (*3*-*7*). The ideal defect chemical model proposed by Kitamura predicts the formation of pyrophosphate-type defects that are compensated by protons, oxygen vacancies, or electron-holes. First-principles models show that in an ideal crystal unit cell, protons should move through the materials by hopping between the oxygen corners of the phosphate tetrahedra, with an activation energy of about 0.80 eV (*8*).

However, compiling the conductivity data from various groups using different synthesis techniques shows that ionic conductivities for nominally similar compositions may differ by a factor of 10 or more. A study by our group (*9*) shows that small variations in stoichiometry, whether introduced intentionally or unintentionally, can have a profound influence on the thermal behavior, the sintered microstructure, and therefore the conduction properties of a sample. Thus, close attention needs to be paid to the composition and microstructures of phosphate materials before interpreting conduction measurements.

Recently, several in-depth studies of the thermal behavior of rare earth phosphates prepared using different techniques have been published (*2, 10-18*). These give some insight into the typical phases encountered when synthesizing phosphates using various techniques. The technique used in the Amezawa papers and which is followed here for the orthophosphate syntheses involves precipitation from aqueous solutions. Solution synthesis can result in particles with adsorbed water, hydrogen phosphates, metal trioxyphosphates, or phosphoric acid, which are difficult to remove except with very high temperature heat treatments (*2, 10, 13*). The presence of any excess phosphates on the original particles can affect the kinetics of grain growth during sintering. Hernandez et al. (*13*) and Harley et al. (*9*) both obtain very large-grained microstructures upon intentional addition of excess phosphates. In addition, phosphate-containing compounds are known to be subject to phosphorous loss through the formation of volatile P_4O_{10} compounds. During high temperature treatments, for example during sintering, these escaping gases give rise to intragranular voids. Stoichiometric phosphate compounds are also subject to P_4O_{10} losses at high temperatures, which can push them off stoichiometry (*13*). Park and Kriedler (*12*), who construct a full phase diagram of the La_2O_3-P_2O_5 system, heat treat various lanthanum phosphates inside of sealed ampoules in order to avoid loss of phosphorous.

Despite these known challenges with phosphate chemistry, it is useful to study the higher phosphorous containing compounds, specifically the cerium pyrophosphates and metaphosphates, for their protonic conduction. Since protons move by physically hopping between phosphate tetrahedra, compounds containing long phosphate chains could provide connected pathways for conduction. Gaining a better understanding of the crystal symmetries of these compounds can also help to identify extra phases, and confirm the defect equilibria predicted by Kitamura.

In this chapter, we explore and characterize the lanthanum and cerium orthophosphates, the cerium pyrophosphates, and the cerium metaphosphates obtained using various synthesis methods. Methods such as aqueous precipitation of ceramic powders, spark plasma sintering, and glass-ceramic processing are discussed, and their effects on the microstructures of the samples are compared.

Experimental

2.1 Synthesis of Rare Earth Phosphates

2.1.1 Orthophosphates $LaPO_4$, $CePO_4$, $(La,Ce)PO_4$

To synthesize the $LaPO_4$ and $CePO_4$ powders, 2 molar aqueous solutions of $Ce(NO_3)_3{\cdot}6H_2O$ (Alfa Aesar) or $La(NO_3)_3{\cdot}6H_2O$ (Alfa Aesar) were added dropwise to a 2 molar aqueous solution of $NH_4H_2PO_4$ (Acros Organics) in a 1:1 metal to phosphorus ratio. For some of the samples, the pH was controlled using buffer solutions of citric acid and sodium citrate. The pH was set to 3, 4, 5, and 6. For syntheses without buffers, the pH of the solution was measured to be about 1.

The resulting precipitates (fine white solids) were collected using centrifugation, washed with water, filtered, and dried. The collected precipitates had the hydrated rhabdophane phase of the rare earth orthophosphate. The powders were heat treated at 800°C for 2 hours in order to transform them to the monoclinic monazite phase. The powders were ground with an agate mortar and pestle, and passed through a 325 mesh sieve.

For mixed La/Ce/Sr phosphate compositions, appropriate amounts of the $LaPO_4$, $CePO_4$, and $SrHPO_4$ (99.99% purity, Aldrich) powders were combined in an attritor mill with isopropyl alcohol, and milled for 2 hours at 450 rpm, using a silicon nitride actuator and crucible. To determine the solubility limit of the Sr dopant, a series of $Ce_{1-x}Sr_xPO_4$ samples was made with x = 0.02, x = 0.05, and x = 0.1. The resulting powder mixtures were dried, pressed at 145 MPa into 13 mm diameter pellets, and sintered for 5 hours at 1450°C. Sintered pellets had densities ranging from 80-95%.

2.1.2 Pyrophosphate: CeP_2O_7

Cerium oxide (CeO_2, Alfa Aesar) and concentrated phosphoric acid (85%), (J.T. Baker) were mixed at a Ce:P ratio of 1:2. The mixture was heated at 150°C until it formed a yellow paste. The solid was washed, collected by centrifuge, and calcined at 300°C for 2.5 hours. The obtained powder was crushed and pressed into pellets, and the pellets were heat treated at various temperatures. Heat treatments at 300°C and below were not high enough to fully crystallize the precipitates. At heat treatments of 500-700°C, the cubic phases of CeP_2O_7 formed, but at heat treatments above 700°C, the material began to transform to mixtures of monoclinic monazite and the orthorhombic metaphosphate.

2.1.3 Metaphosphate: CeP_3O_9

Glasses of nominal composition $Ce_{1-x}Sr_xP_3O_9$ where x=0, 0.16, and 0.32 were prepared by combining the appropriate amounts of reagent-grade cerium oxide (Alfa Aesar), strontium hydroxide hydrate, (Aldrich) and 85% phosphoric acid (J.T. Baker) in a covered platinum crucible and heating to 1300°C for 30 min, and then pouring the melt onto a steel plate preheated to about 350°C. The glasses were orange and translucent. The glasses were cut into 1 mm thick wafers using a diamond saw. To crystallize the glass, the wafers were slowly heated in air or argon over a period of 3 hours from room temperature to 600°C, 700°C, or 800°C and then held at that temperature for various amounts of time. Opaque glass-ceramics were obtained.

2.1.4 Hydrated metaphosphate: CeP_3O_9 $3H_2O$

The synthesis of the cerium metaphosphate hydrate involved several steps. The procedure followed comes from Bell and Serra (*19, 20*). $NaHPO_4$ (Alfa Aesar) was heated at 530°C for 5 hours to form $Na_3P_3O_9$. This compound was a powder that would not dissolve in water even with refluxing. Bell et al. attribute this to structural issues—the obtained compound has long, disordered, insoluble chains of phosphates. To solve this problem, the NaP_3O_9 was added to a saturated NaCl solution, resulting in the formation of $Na_3P_3O_9$ hydrate (JCPDS 15-0740). This compound was centrifuged, washed, dried, and its structure was confirmed using XRD. Finally, $CeCl_3$ (Strem) was dissolved in water and added in the ratio Ce:Na = 1:3 to the dissolved $Na_3P_3O_9$ hydrate, resulting in the CeP_3O_9 H_2O hydrate (JCPDS 25-0189).

2.1.5 Spark Plasma Sintering

Powder samples of $CePO_4$ and CeP_2O_7 were sent to U. C. Davis for spark plasma sintering. The $CePO_4$ samples were uniaxially pressed into a pellet, and sintered in a graphite die under pressures of 50 and 100 MPa while heating at 1000, 1100, and 1200C, with the aid of a pulsed DC current. The CeP_2O_7 samples were sintered under pressures of 50 and 100 MPA while heating at 600C. A good review of the field-assisted sintering technique is found in (*21*).

2.2 Microstructural Characterization methods

2.2.1 Density measurements

The densities of the pellets were calculated by measuring their dimensions and masses. The measured densities were compared to the theoretical densities calculated from the crystal structures. A estimate of the pellet's porosity to within about 2% accuracy could be made from these measurements, but only imaging the fracture surfaces could confirm if fully dense microstructures were achieved.

2.2.2 XRD

The crystal structures of the various phosphate phases were confirmed using a Philips PW3040 X'Pert Pro Diffractometer using a Cu Kα (α =1.54056Å) source operated with a 45keV X-ray tube voltage. The measured XRD patterns for orthophosphates were matched to the JCPDS cards for rhabdophane $LaPO_4 \cdot nH_2O$ 04-0635, monoclinic $LaPO_4$ 32-0493, and monoclinic $CePO_4$ 32-0199. The pyrophosphate and metaphosphate patterns matched as follows: CeP_2O_7 JCPDS 16-0584, CeP_3O_9 JCPDS 33-0336, and CeP_3O_9 $3H_2O$ JCPDS 25-0159.

2.2.3 SEM

The microstructures of the sintered pellets and glass-ceramics were studied by an analytical scanning electron microscope (SEM, Zeiss Gemini Ultra-55) operated at 5 kV and equipped with an energy dispersive X-ray spectroscope (EDS). In addition, a Hitachi Tabletop SEM TM-1000 was used for quick imaging.

2.2.4 TEM

Electron images were obtained using a transmission electron microscope (TEM, JEOL 2100F) operated at 200 kV, equipped with an energy dispersive X-ray spectroscope (EDS). The elemental distributions, determined by high angle annular dark-field (HAADF-STEM, also called Z-contrast) imaging and EDX composition analysis, were acquired on JEOL 2100F with an annular dark-field detector and Oxford INCA EDX microanalysis system. In the scanning mode (STEM mode) the 1.5 nm focused electron beam was stepped across the specimen for imaging and chemical analysis. HAADF imaging in STEM is a technique based on a theory that higher atomic number (*Z*) elements scatter electrons with higher angle than that of lower *Z* elements. Therefore, the elements with higher atomic number will have brighter contrast compared to the light elements with lower atomic number [7]. The TEM samples were made from the planar sections of the sample, by mechanical pre-thinning (Gatan dimple grinder) and Ar-ion milling (in a Fischione system) with a liquid

nitrogen cooling stage to minimize artifacts. This work was performed with the assistance of Dr. Ruigang Wang in our program group.

2.3 Results and Discussion of microstructural characterizations

For all of the different rare earth phosphate samples synthesized, crystal and microstructural information were gathered using XRD, SEM, TEM, and vibrational spectroscopy data. It was necessary to use this combination of techniques to gain a full understanding of the mixture of crystalline and amorphous phases present in the final sintered samples.

2.3.1 Lanthanum and Cerium Orthophosphates

All of the electrochemical measurements that will be discussed in Chapters 3-5 of this work are conducted upon rare earth orthophosphate samples. Before conductivity measurements could be carried out, the microstructures of the orthophosphate samples had to be reproducible and well understood. The synthesis and processing conditions for the orthophosphates had a strong influence on the morphology and the amounts of excess phosphates present in the samples. First, the lanthanum orthophosphate samples prepared at pH=1, 3, 4, 5 and 6 are compared.

2.3.1.1 XRD and SEM

The aqueous precipitation of the orthophosphates from the lanthanum nitrates and hydrogen phosphates all resulted in fine, white solids. However, the pH of the aqueous solution affected the rate of precipitation and the morphology of the precipitates obtained. At low pHs, the precipitate took several minutes to form, and the precipitates obtained were a flowing powder. As the pH increased, the precipitates formed more quickly, but were finer and tended to agglomerate into a gel. Since finer particles have a larger surface area, it was noted that there may be more excess phosphates adsorbed onto the pH=5 and pH=6 samples.

Figure 2.1 shows the XRD spectra taken of the as-precipitated $LaPO_4$ powders. All of the precipitates show some crystallinity and match JCPDS card 04-0635, which is the hexagonal hydrated rhabdophane structure. However, the precipitates formed at pH 1 have high crystallinity, while those formed at pH 3, 4, 5, and 6 all show very broad peaks. This observed decrease in crystallinity with increasing pH is consistent with the findings of Lucas et al. (*2*) They attribute the changes in the degree of crystallinity to the kinetics of the nucleation and growth of the particles in solution. This group also carried out extensive thermal and elemental analysis of their samples and observed that larger amounts of phosphoric acid and polyphosphates $La(PO_3)_3$ were adsorbed onto the surfaces of the orthophosphate particles as the pH increased. Evidence of such phases was observed in the present work as well when examining the sintered pellets using SEM.

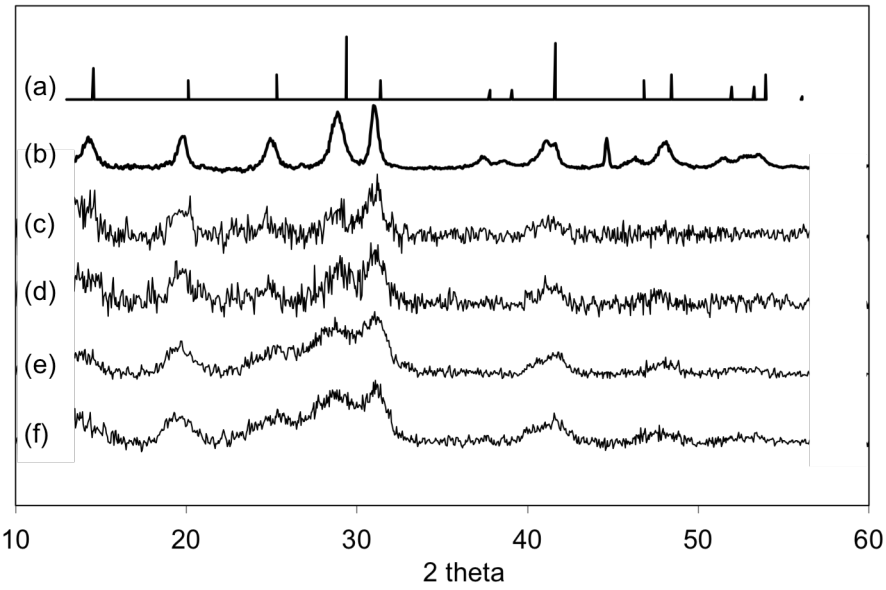

Figure 2.1. XRD spectra of the lanthanum phosphate powders obtained by precipitation at various pHs. (a) Stick pattern for JCPDS card 04-0635 for the hydrated rhabdophane structure. (b) pH=1, (c) pH=3, (d) pH=4, (e) pH=5, (f) pH=6. The extra peak in (b) at 44° is from iron from the sample holder.

All of the precipitated rhabdophane powders were treated in air at 800°C. After this treatment, all of the powders changed phase to monoclinic monazite matching JCPDS card 32-0493. Figure 2.2 shows that there are no detectable differences between the XRD spectra of all 5 powders after this heat treatment. It is important to note, however, that amorphous phases are undetectable using the XRD technique.

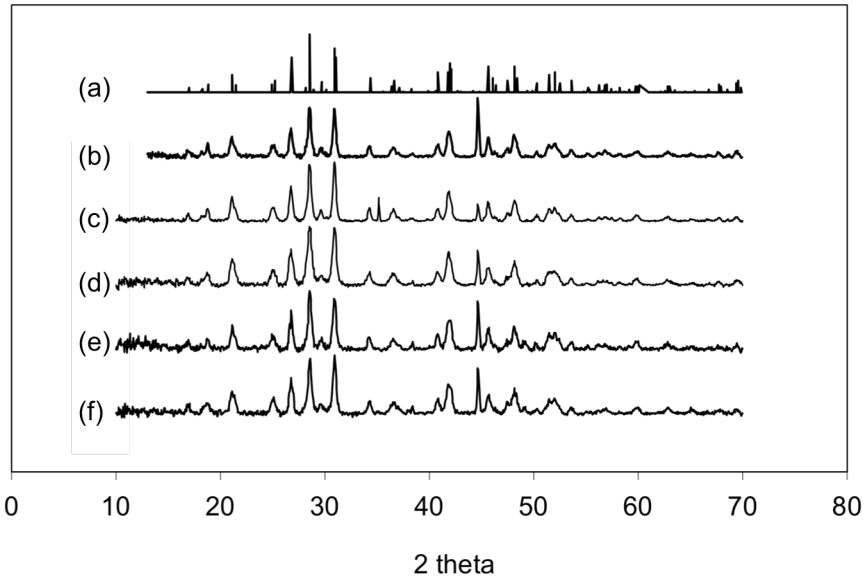

Figure 2.2. XRD spectra of the $LaPO_4$ powders obtained at different pHs after heat treatment at 800°C. All of them match the pattern for the monoclinic monazite phase with no extra peaks. (a) Stick pattern for JCPDS card 32-0493. (b) pH=1, (c) pH=3, (d) pH=4, (e) pH=5, (f) pH=6. The peak at 2 theta = 44° corresponds to Fe from the sample holder.

Figure 2.3 is a series of SEM images of the calcined particles and sintered samples of the materials obtained at pH=3, pH=4, and pH=5. Although they all have the same XRD spectrum, stark differences in morphology can be observed. Particles precipitated at pH=3 are about 500 nm in diameter (though these could be agglomerates of smaller particles; the resolution limits further analysis). The grains in the sintered sample are about 2 um across. The sintered sample shows equiaxed grains with clean grain boundaries. The particles from the pH=4 precipitation are much smaller; TEM images not shown here indicated that they were 10-20 nm in diameter. The sintered compact has grains approximately 3 mm across. The grains are not well packed, and the surface of the sintered samples is partially coated with amorphous phases. Such features typically result if a liquid phase, present during sintering, is squeezed out from connected triple junction phases. The particles from the pH=5 sample were so small that they agglomerated immediately upon precipitation and formed a gel. After calcination, the particles still cannot be distinguished in the SEM image. The sintered pellet is even poorer quality than the other two; the large agglomerates and small particulates do not pack well and the compact could not sinter properly.

These preliminary studies indicate that precipitation at low pH results in particles with the lowest surface area, the highest degree of crystallinity, and the highest quality sintered microstructure. For the rest of the orthophosphate samples synthesized in this work, the precipitation was carried out at pH=1.

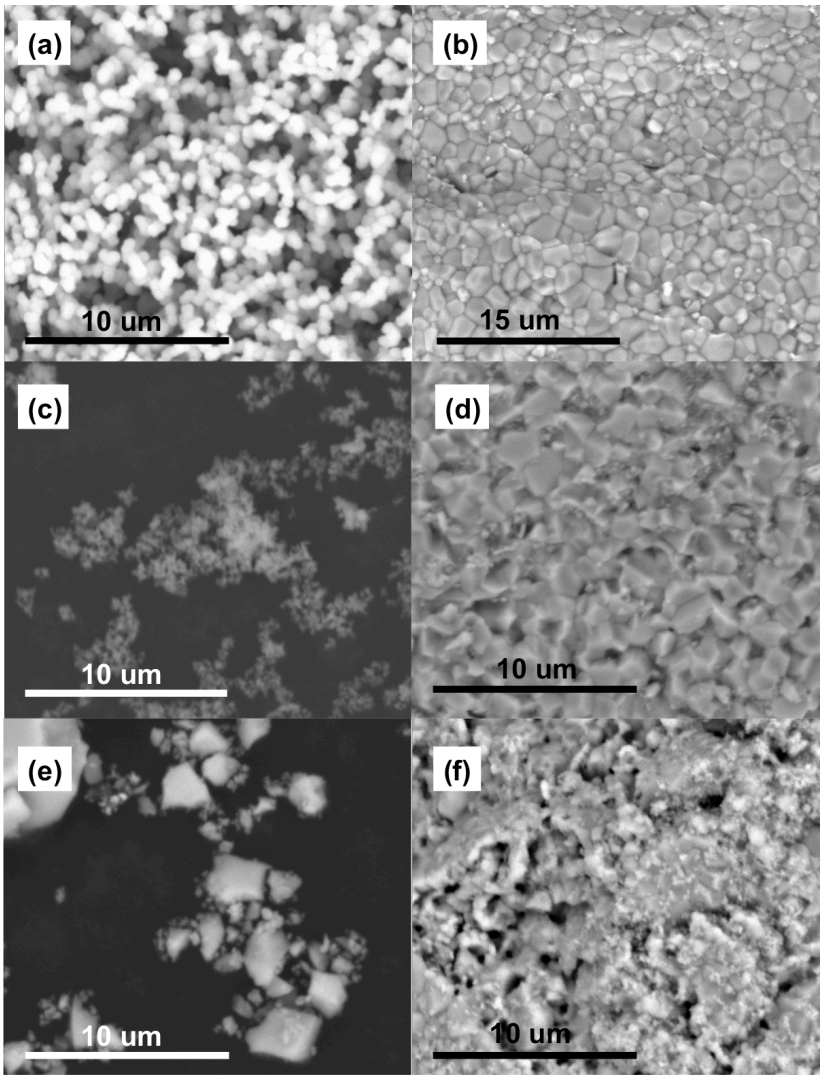

Figure 2.3. SEM images of the calcined $LaPO_4$ particles and the sintered samples obtained from them. (a) Particles precipitated at pH=3, (b) sintered pellet from pH=3, (c) particles precipitated at pH=4, (d) sintered pellet from pH=4, (e) agglomerated particles precipitated at pH=5 and dried (f) sintered pellet from pH=5.

In order to determine the solubility limit of the dopant in the monoclinic orthophosphates, a series of $CePO_4$ samples doped with 2, 5, and 10 mol % of strontium were synthesized. The XRD pattern for the $CePO_4$ powder matched JCPDS card 32-0199. The XRD spectra of the doped and sintered samples are pictured in Figure 2.4. The crystalline second phase $Sr_3Ce(PO_4)_3$ begins to appear for Sr contents above 2 mol %. The low solubility limit for small alkaline earth dopants in monazite is attributed in a review by Clavier et al. (*17*) to the mismatch in ionic radius. However, studies by Amezawa et al. (*5*) on doping with different alkaline earth elements did not give higher solubility limits, suggesting that the charge mismatch is the dominant factor. This doping limit of 2 mol % Sr was kept constant for all orthophosphate samples synthesized for electrochemical testing.

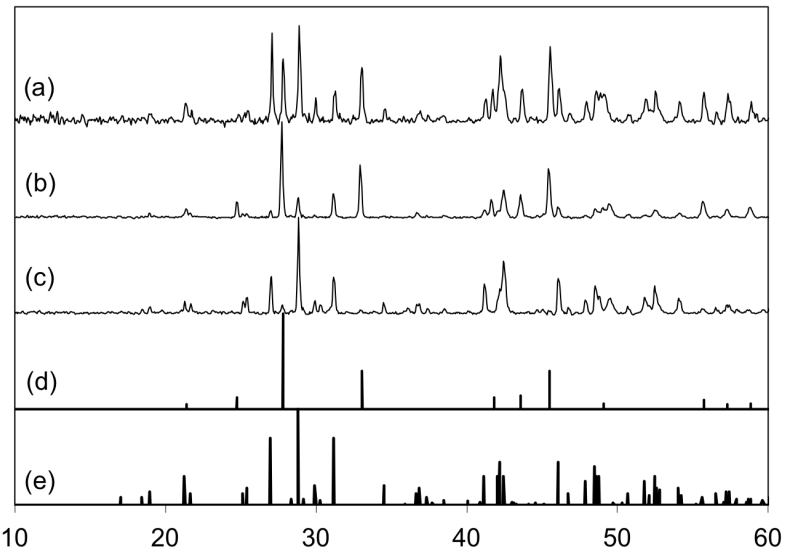

Figure 2.4. XRD spectra of CePO4 doped with (a) 10 mol % Sr, (b) 5% Sr, and (c) 2% Sr. (d) The stick pattern JCPDS 25-0189 for the second phase, $Sr_3Ce(PO_4)_3$ that forms for Sr content 5% and above. This phase is clearly visible in both the 5% and 10% Sr doped samples. (e) The stick pattern JCPDS 32-0199 for monazite $CePO_4$.

The 2% Sr-doped lanthanum and cerium orthophosphates precipitated at pH=1 still showed some variation in microstructure with different calcination and sintering treatments. Figure 2.5 shows SEM images of sintered samples shows four examples of microstructures obtained under various conditions. Figure 2.5 (a) shows a sample for which the precipitated powders were treated at 900°C, pressed, and sintered at 1450°C. The microstructure is ideal—grains are micron-sized and densely packed, and there are no obvious second phases. 2.5(b) shows a sample for which an amorphous liquid-like phase has flowed over the surface of the sample. Figures 2.5(c) and (d) depict fracture cross sections of samples with non-ideal microstructures. 2.5(c) shows large intergranular voids, which form when the sample is not packed and pressed properly. 2.5(d) shows a sample with very large grains, longer than 50 μm, with small intragranular pores evident throughout all the grains. Rapid grain growth and holes created by escaping volatiles are again characteristic of excess phosphates present in the sample. Structural measurements such as XRD, Raman, and FTIR were not capable of detecting the presence of these defects; it was only possible to find them using visual inspection of SEM images. As will be noted in the next section, even samples with the ideal microstructures showed some amorphous grain boundary phases in higher magnification images. The chemical makeup of these phases will be discussed later.

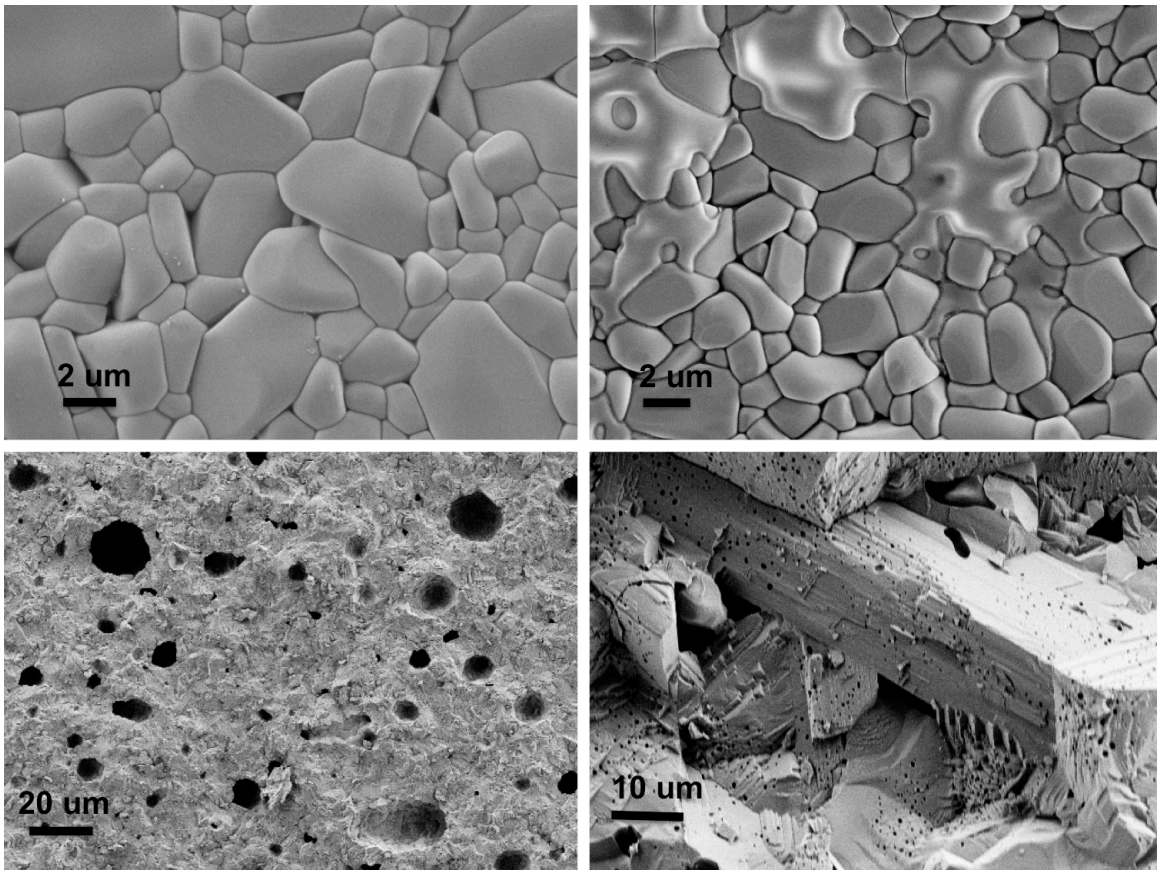

Figure 2.5. Microstructures of monazite sintered in air at various temperatures. (a) A fully dense (>95%) sample of $Ce_{0.98}Sr_{0.02}PO_4$ sintered in air at 1450°C for 5 hrs. This is the ideal microstructure for the samples. (b) A dense sample of $Ce_{0.98}Sr_{0.02}PO_4$ but with a visible liquid-like phase on the surface of the ceramic. EDX analysis shows that this phase is phosphate-rich. (c) The fracture surface of a 75% dense $La_{0.98}Sr_{0.02}PO_4$ sample sintered in air at 1200°C. Large holes are found throughout the sample. This microstructure was obtained when samples were poorly packed and sintered at too low of a temperature. (d) A very large grain on a fracture surface of a $Ce_{0.98}Sr_{0.02}PO_4$ sample that shows a high density of very small pores as may result from rapid grain growth typically associated with the presence of liquid phases.

Figure 2.6 depicts fracture surfaces of samples with dense, small-grained microstructures. These samples were attained using the spark plasma sintering technique. Using this technique, ceramic samples can be densified at low temperatures and with very little grain growth. This shows that this technique works for rare earth orthophosphates, and opens the possibility of using this technique in further experiments.

For example, it would be possible to vary the particle sizes of precipitated orthophosphates by controlling the pH of the precipitation solution. Excess phosphates on the surfaces of the particles could perhaps be removed by controlled heat treatment. Using SPS to sinter them would allow a systematic comparison of a sample's conductivity to grain size and grain boundary volume. This experiment would allow us to test the hypothesis presented by Harley et al. (*9*) that predicts higher proton conduction in amorphous grain boundary phases. Preliminary conductivity measurements carried out on these samples, but not shown here, showed the total conductivity to be about one order of magnitude lower than

the pressureless-sintered samples. Further experiments and analysis of this result will have to be the subject of a future study.

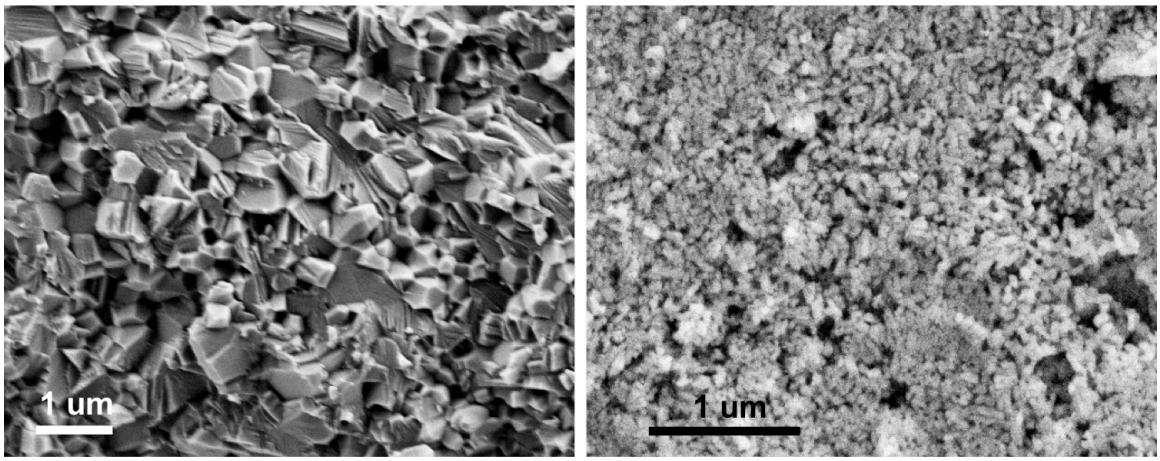

Figure 2.6. Fracture surfaces of ceramics sintered using the spark plasma sintering technique. (a) $CePO_4$ sample with grains about 0.5 um long. (b) Sr-doped $CePO_4$ sample with grains about 100nm long.

2.3.1.2 TEM and EDX

Transmission electron microscopy was used to inspect the unsintered particles and sintered ceramics for second phases and crystallinity. The EDX capability gave elemental analysis of a sample with spatial resolution. This technique is highly informative, but only a few bulk samples were studied due to the difficulty of sample preparation. Electron beam damage occurred for phosphorous-rich compositions, and prevented in-depth crystal analysis.

Figure 2.7 is an HR-TEM image of monoclinic $CePO_4$ grains. Crystal lattice fringes are visible at high resolution, and the particle sizes of 50-100 nm can be observed at lower resolution. If amorphous phosphate phases are present on the surfaces of these grains, they are not clearly identifiable using this technique. However, TEM images of sintered ceramics made using the same process show that second phases do form. Figure 2.8 shows the electron image of a sintered ceramic sample of composition $La_{0.39}Ce_{0.59}Sr_{0.02}PO_{4-\delta}$ (*22*). The image reveals the presence of 3-5 nm thick amorphous phases at grain boundaries and junctions between 3 grains.

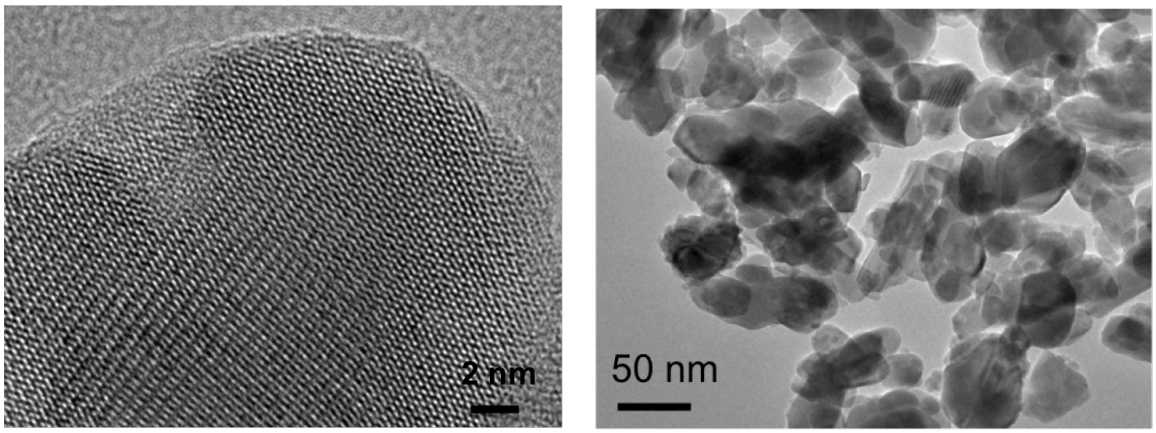

Figure 2.7. TEM images of monoclinic $CePO_4$ grains. Grains are 50-100 nm long and show good crystallinity after the annealing treatment.

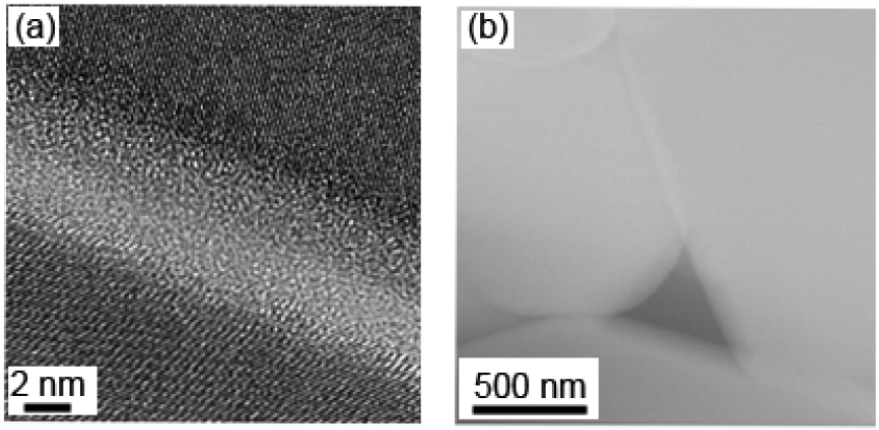

Figure 2.8. (a) HR-TEM image of a sintered pellet with composition $La_{0.39}Ce_{0.59}Sr_{0.02}PO_{4-\delta}$. An amorphous film about 4 nm thick is present at the grain boundary. (b) TEM image of a junction between 3 grains of the same sample. The junction contains a large pocket of amorphous phase. This image is taken from (*22*).

Spatially resolved EDS analysis was carried out for a TEM sample of composition $La_{0.39}Ce_{0.59}Sr_{0.02}PO_{4-\delta}$ (*22*). Figure 2.9 shows the TEM image and three elemental maps of a junction between two grains (light grey) and the amorphous phase (darker grey) between them. The bright red and blue colors of the Ce and La elemental maps show that the rare earth content of the bulk grains is much higher than that of the grain boundary phase. In contrast, in the Sr elemental map, the grain boundary phase is brighter, which indicates that the Sr content of the bulk grains is much lower than that of the grain boundary phase. Measurements of the metal to phosphorous ratio in the grain boundary phase also showed enrichment in phosphorous there compared to the bulk. A more quantitative analysis of these measurements is presented in Chapter 4.

These images show that small amounts of amorphous grain boundary phases persist in the rare earth orthophosphates, even in samples that show no evidence of them at the resolution of SEM. These phases affect the conductivities of the samples, first because the amorphous phases appear to be more resistive than the crystalline phases, and second because they are enriched in dopant—the doping level of the bulk grains is lower than the nominal value.

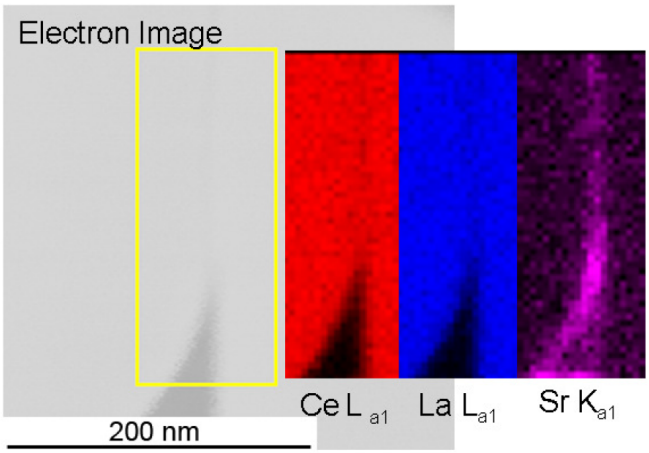

Figure 2.9. Elemental mapping of the La, Ce, and Sr in the bulk and the grain boundary of a $La_{0.39}Ce_{0.59}Sr_{0.02}PO_{4-\delta}$ sample. The electron image shows the intersection of two bulk grains (lighter grey) and a pocket of amorphous grain boundary phase (darker grey). The elemental maps of Ce and La show that those elements are concentrated in the bulk grains, while the grain boundary does not contain detectable amounts of them. In contrast, the elemental map of Sr shows that the grain boundary phase is rich in Sr. This image is taken from (*22*).

2.3.1.3 Summary of Orthophosphate synthesis and characterization

The rare earth orthophosphates were the most stable, simply processed, and reproducible samples synthesized in this study. Therefore, the conductivity measurements in the rest of this work focus on these materials. As discussed above, these samples still show some characteristic defects such as excess amorphous phosphates at the grain boundaries and segregation of the dopant to these phases. The total conductivity of the samples can be affected by these imperfections. However, use of the AC impedance technique allows separation of the bulk and the grain boundary contributions to the conductivity. The sample can be modeled as a composite of bulk and grain boundary phases, and information about both phases can be extracted from the impedance data.

It is instructive to study the cerium pyrophosphates and the cerium metaphosphates because understanding their crystal structures and microstructures can help us to identify structural defects in the orthophosphates.

2.3.2 CeP_2O_7

The cerium pyrophosphates are different from the orthophosphates in that the anion is made up of two linked phosphate tetrahedra $[P_2O_7]^{4-}$, which requires the Ce cation to take the 4+ valence state, rather than the 3+. In addition, the unit cell for this system is pseudo-cubic, similar to ZrP_2O_7, TiP_2O_7 and SnP_2O_7, but with slight distortions that give its actual symmetry as triclinic (*23*).

There was a recent flurry of excitement about pyrophosphate proton conductors with this structure due to measurements showing anomalously high conductivities (10^{-2} S/cm between 50-200°C) (*14, 24-26*). However, the drop-off in conductivity at around 200°C

implied that the conductive species might actually be adsorbed phosphoric acid, which evaporates at about that temperature. Subsequent studies (*27, 28*) showed that indeed, this was the case: conductivity varied systematically with surface area. Since the pyrophosphates tend to decompose to a mixture of the orthophosphate and metaphosphate upon heating above 700°C (well below the sintering temperature), using these materials for gas separation or fuel cells would be difficult. The SPS-sintered compacts synthesized in this study and discussed below conducted very poorly (10^{-6} S/cm at 550°C).

There are several methods in the literature for synthesizing cerium pyrophosphate (*14, 23, 26*). In this work, CeP_2O_7 was obtained by heating CeO_2 and phosphoric acid at 150°C until a paste formed, and then heat-treating the paste until it crystallized into the proper phase.

TEM imaging of the unsintered powders was used to check for the degree of crystallinity of the samples. Figure 2.10 below shows some images of the particles heat treated at 300°C and 600°C. The sample treated at 300°C is amorphous, while the sample treated at 600°C shows crystal lattice fringes. Particles range between 10-100 nm in diameter. As observed in the HR-TEM images of the orthophosphates, if there are amorphous phases present on the surfaces of the crystalline particles, it is not possible to distinguish them using this technique.

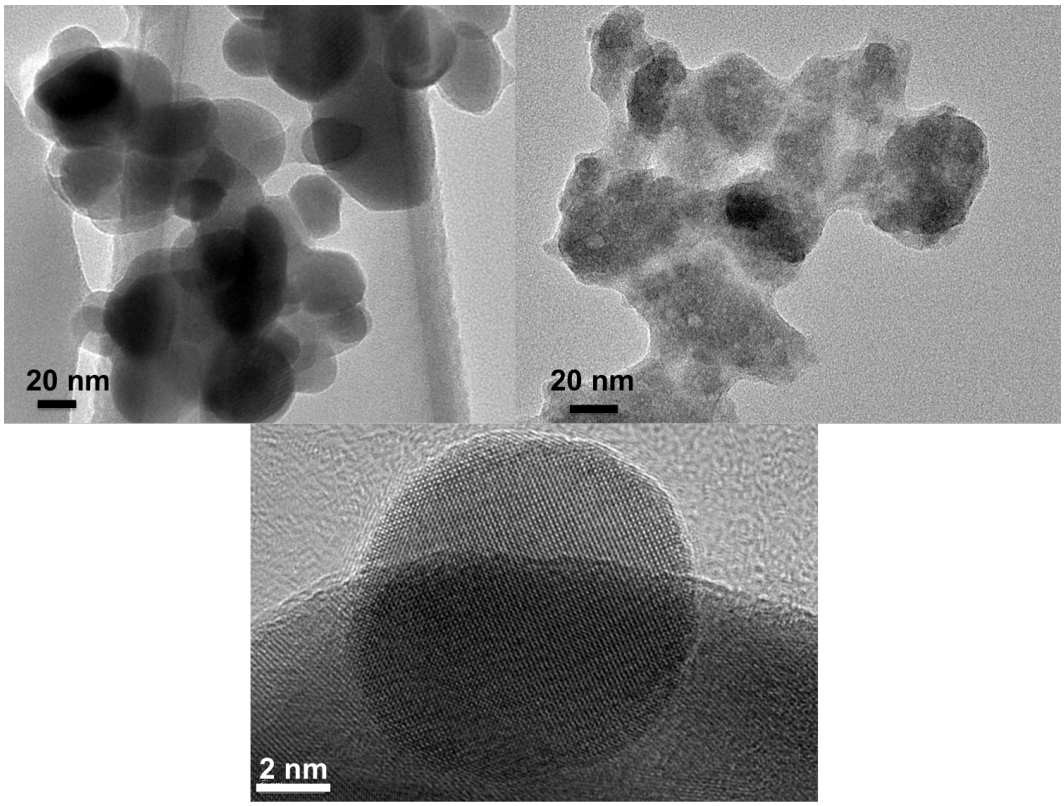

Figure 2.10. TEM images of CeP_2O_7 powders heat treated at 300°C and 600°C. The sample treated at 300°C is still amorphous; the sample treated at 600°C shows good crystallinity.

Figure 2.11 shows the XRD spectra for some CeP_2O_7 ceramic pellets heat-treated at temperatures between 500-800°C. The spectra treated at lower temperatures match JCPDS card 16-0584 for CeP_2O_7 as expected. However, at 600°C some small peaks corresponding to monazite (JCPDS 32-0199) begin to appear, and these grow stronger as the heat treatment temperature increases. The sample treated at 800°C is a mixture of the monazite and metaphosphate phases. This series of measurements proves that it is not possible to attain fully dense CeP_2O_7 using standard sintering methods: the pyrophosphate decomposes far below the temperatures needed for densification and grain growth.

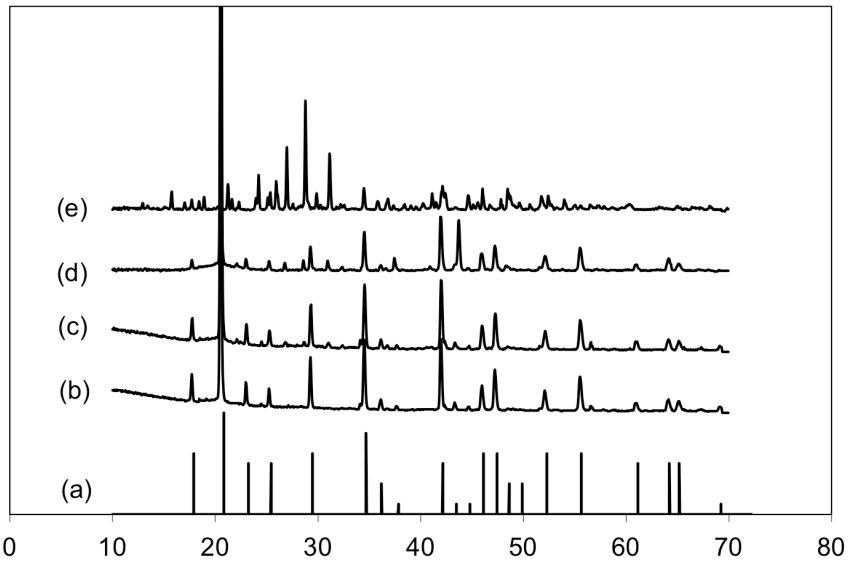

Figure 2.11. (a) The stick pattern JCPDS 16-0584 matches the powder XRD spectrum for CeP_2O_7. XRD patterns for CeP_2O_7 samples heat treated at (b) 500°C, (c) 600°C, (d) 700°C, and (e) 800°C. The samples treated at 600°C and above begin to show extra peaks from the monazite crystal phase, and for the sample treated at 800°C, the monazite phase JCPDS 32-0199 and the metaphosphate phase JCPDS 33-0336 both show strong peaks.

Using the SPS method at at 600°C and 50 MPa allowed us to sinter a CeP_2O_7 sample to 75% density. A fracture cross section of this sample is shown below in Figure 2.12. Grains seem to be a mixture of sizes, 5-20 um. XRD measurements (not shown here) confirmed that this sample still matched JCPDS card 16-0584. AC impedance measurements of this sample showed that its conductivity was quite low: 10^{-6} S/cm at 550°C. (The AC impedance technique will be discussed in Chapters 3 and 4.) This is far lower than conductivity levels of 10^{-2} S/cm between 50-200°C measured by Nagao (*25*) and Einsla (*24*) for SnP_2O_7 and Sun (*14*) for CeP_2O_7. However, as discussed before, the anomalously high conductivities claimed in these works is thought to be due to adsorbed phosphoric acid. This is supported by careful studies by Kreller (*28*). Conductivity measurements by our group on SnP_2O_7-LaP_3O_9 composites (*27*) showed low conductivity, as did those by Kreller.

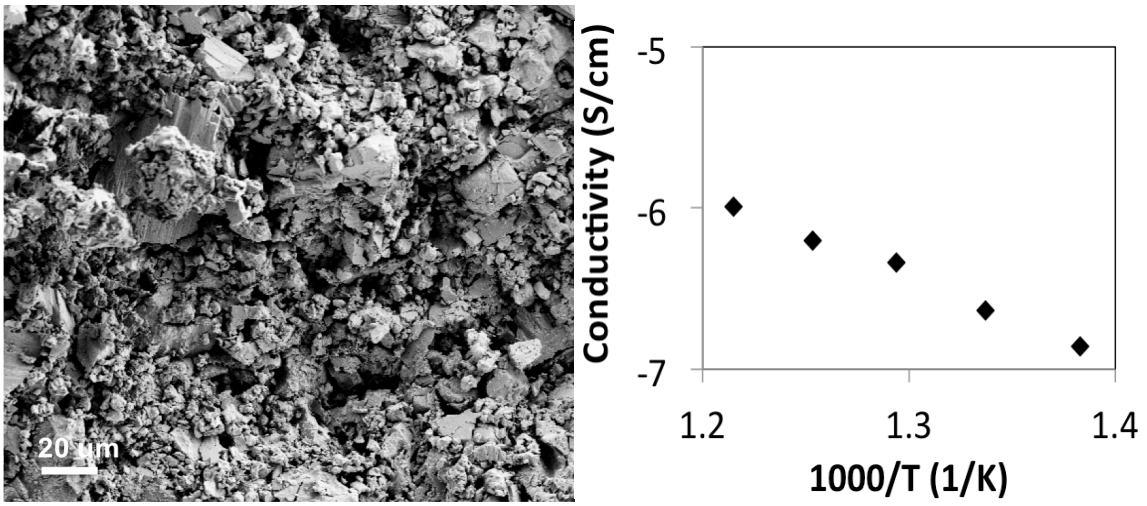

Figure 2.12. (a) Fracture surface of CeP_2O_7 ceramic sintered using the spark plasma sintering technique. The sample obtained was 75% dense. (b) Conductivity vs. temperature for this sample in 3% humidified air.

2.3.2.1 Summary of CeP_2O_7

The CeP_2O_7 structure was successfully synthesized and is stable at low temperatures. Above 600-800°C, the material decomposes to a mixture of monazite and orthorhombic metaphosphate. The SPS technique can be used to densify it to 75% of theoretical. Conductivity measurements of dense CeP_2O_7 samples are quite low, in contrast to the pyrophosphate samples measured by Nagao et al. (*25*) and other groups. This supports recent studies of these materials that attribute the high conductivity to residual surface phases. Comparison of the vibrational spectra of this compound will be compared later in this chapter to the orthophosphate and metaphosphate compounds in order to identify defect species in doped orthophosphate samples.

2.3.4 CeP_3O_9 glasses and glass-ceramics

While the crystal structures, microstructures, and proton conduction properties of lanthanum metaphosphates have been studied by Amezawa et al. (*4, 29, 30*)and by our group (*31-33*) little attention has yet been paid to the proton conductivity of cerium metaphosphates. The rare earth metaphosphates, like cerium pyrophosphate discussed above, are known to decompose to orthophosphates and P_4O_{10} when heated over 800°C. Thus, special processing and sintering techniques must be used to obtain dense samples. As will be discussed later, synthesis of cerium metaphosphate powders is complex: depending on the synthesis technique, multiple crystal structures can be obtained. In this work, we examine the glass-ceramic synthesis pathway, which has been used before in our group to produce dense samples. However, the samples produced have complex microstructures with a mixture of glassy and crystalline phases that are difficult to control and reproduce.

Glass samples were quenched on a hot plate, then annealed. Heat treatments at 700°C were carried out for various amounts of time in order to transform them to glass-ceramics. The samples were first characterized using XRD. The XRD spectra of all glasses (not shown) were noisy with no identifiable peaks, due to their lack of long-range order. The XRD

patterns for samples heat-treated at 700°C for 5 hours are shown in Figure 2.13. Samples are doped with 0, 16, and 32 mol% Sr. XRD spectra were first were taken of the bulk glass-ceramic discs, and then of the same sample after it was ground to a powder. Most of the peak positions of the spectra match JCPDS card 33-0336 for CeP_3O_9. The extra peaks at about 21 and 22 degrees could correspond to second phases SrP_2O_6 or CeP_2O_7, but a definite match could not be made. There is a significant mismatch in peak intensity between the theoretical CeP_3O_9 pattern and the two doped bulk samples. For these spectra, there is an intensified peak at $2\theta=24.25^0$ from the (002) reflection. This phenomenon is interpreted to mean that the growth of the ceramic during the heat treatment occurs in a preferred orientation. However, the increased intensity of this peak disappears when the bulk samples are ground to powder: the peak intensities from powder samples (randomly oriented particles) would show a slightly intensified peak at $2\theta=25.9^0$ corresponding to the (220) peak. The origin of this smaller discrepancy in intensity is unknown.

Figure 2.14 shows XRD spectra for undoped cerium metaphosphate glass-ceramic samples treated for 1 hour, 5 hrs, and 20 hours in air. Samples were ground to powder before measuring the spectra. All samples match the same pattern, 33-0336. There are no differences observable between these spectra. However, SEM images of fracture cross sections of these same samples show very large differences in the microstructures. Thus, it is not possible to distinguish the degree of crystallinity of the samples using XRD.

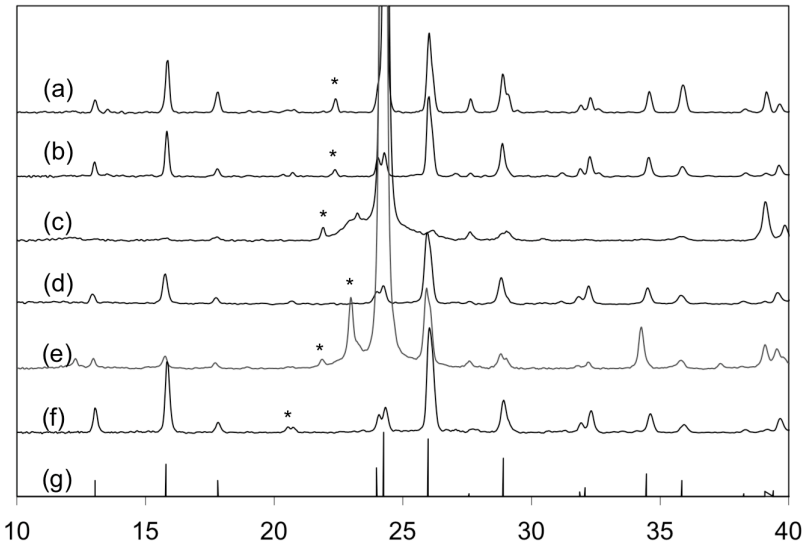

Figure 2.13. XRD spectra of cerium metaphosphate glass-ceramics plotted vs. 2θ. (a) Undoped CeP_3O_9 bulk glass-ceramic sample, (b) the same undoped CeP_3O_9 sample ground to powder, (c) 16% Sr-doped CeP_3O_9 bulk sample, (d) 16% Sr-doped CeP_3O_9 powder sample, (e) 32% Sr-doped CeP_3O_9 bulk sample, (f) 32% Sr-doped CeP_3O_9 powder sample. (g) Most peaks in the spectra match JCPDS card 33-0336. The doped, bulk samples show some very intense peaks at $2\theta=24.25$, indicating preferred orientations for grain growth. After the glass-ceramics are ground to powder, the spectra no longer show such large variations in intensity. Asterisks mark peaks that may correspond to a second crystalline phase (SrP_2O_6 or CeP_2O_7).

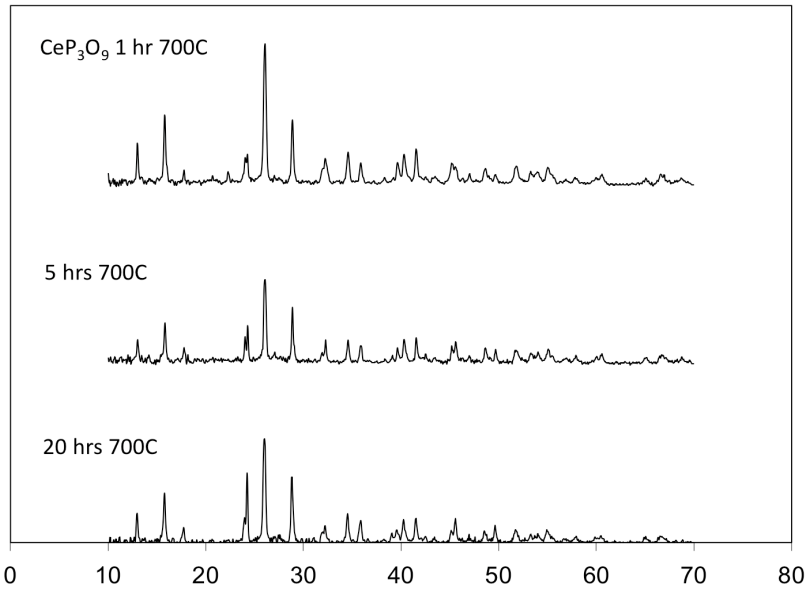

Figure 2.14. XRD spectra of cerium metaphosphate glass-ceramics recrystallized by heat-treating bulk glass discs at 700°C in air for 1 hr, 5 hrs, and 20 hrs. All spectra match JCPDS 33-0336.

The same samples measured in Figure 2.14 were broken in half, and the morphology of the fracture surface was observed using SEM, as shown in Figure 2.15. These images show that crystallization begins at the outside surfaces of the sample and grains grow in toward the center of the sample over time. After just 1 hour of heat treatment, the crystal front has only grown about 50 microns in from the surface. After 2 hours, the crystal growth has progressed, but there is still an amorphous phase visible at the center of the sample. After 5 and 20 hours of heat treatment, the grains seem to have grown all the way in to the center of the sample. It is noted in these images that there seems to be a preferential growth orientation perpendicular to the wafer's surface, which would be consistent with the preferred orientation noted in Figure 2.14.

The microstructures shown in Figure 2.15 would give the impression that this glass-ceramic transformation process is easily controlled and predictable. However, this is not true: the nucleation and growth process of these microstructures varied from sample to sample. Since glass melts were synthesized in small batches, only a few samples could be created from each batch. Homogeneity within a batch could be achieved, but from batch to batch, the recrystallization behavior varied widely. Figure 2.16 shows some microstructures that result from non-ideal crystallization processes. One commonly found defect was the large void observed in 2.16(a). The appearance of this void is not unexpected. Since crystals are more densely packed than glasses, the recrystallized material does not take up as much volume as the glass. Figure 2.16(b) and (c) show grain growth that occurs at different rates: sometimes under the same processing conditions, grains would grow far more quickly or far more slowly than expected. Figure 2.16(b) shows that when grain growth occurs too quickly, the crystals are not orderly – they grow in many different unpredictable orientations and seem to have more voids. Figure 2.16(c) shows a sample that was heat treated for 3 hours—a period of time deemed sufficient to recrystallize the entire sample. However, the interface between the crystallization front

and the glass is still clearly visible. Finally, Figure 2.16(d) shows a junction between three crystallization fronts. There are gaps between the different crystallization fronts; this was common in many samples as well.

These voids and residual glassy phases would have an adverse effect on proton conduction in the samples, since both interrupt the continuity of the sample. These defects in the glass-ceramic were not observable using non-destructive techniques. This shows that the synthesis and processing conditions of the glass-ceramics must be tuned a great deal to improve the reproducibility of these microstructures.

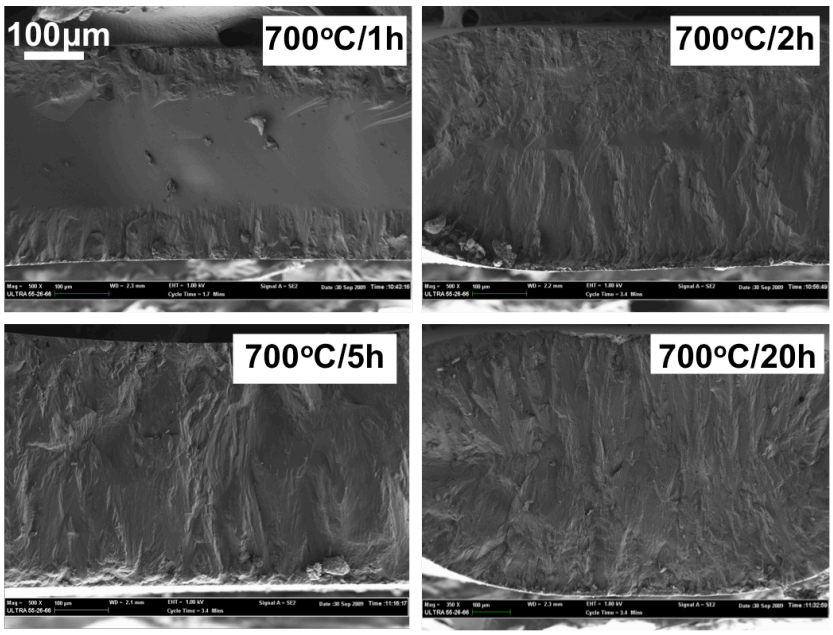

Figure 2.15. Fracture cross sections of CeP_3O_9 glass-ceramic disks annealed for different periods of time at 700°C. The sample starts as an amorphous glass. Metaphosphate crystals nucleate at the outside surfaces of the disks and slowly grow in toward the center. After 1 and 2 hours, there is still glass left in the center of the sample. After 5-20 hours the crystallization appears more complete.

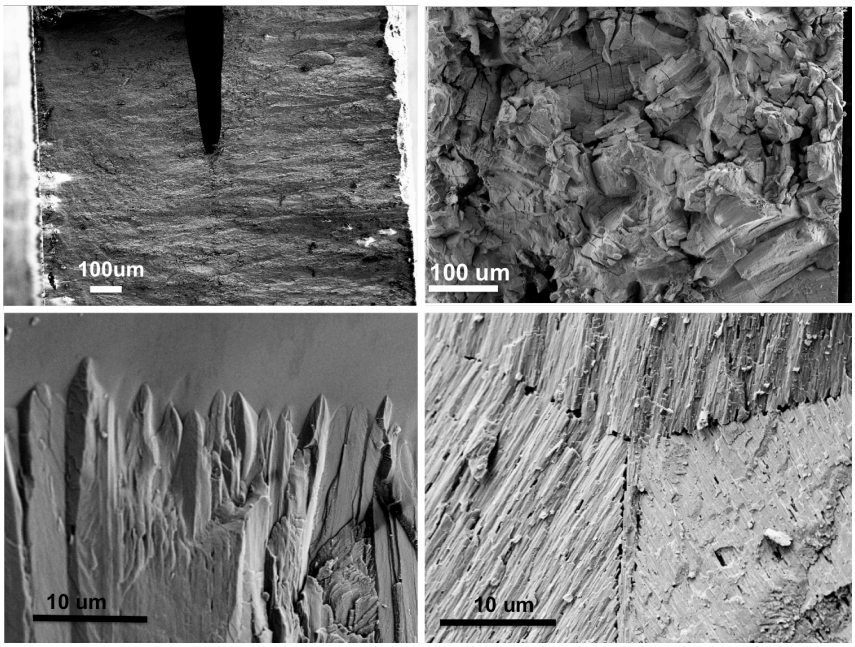

Figure 2.16. Fracture surfaces of CeP_3O_9 glass-ceramics with non-ideal microstructures. (a) Large voids can appear at the center of the disks during the recrystallization process. (b) Large, disordered, cracked grains that do not have good contact with each other can form when the crystallization process occurs too quickly. (c) Image of grains growing into the glass. (d) A triple junction of crystallization fronts meeting in a Y.

Finally, TEM-EDX analysis of the glass-ceramic samples was carried out in order to track the chemical composition of the different phases. Figure 2.17 depicts a grain of 16% Sr-doped CeP_3O_9 glass-ceramic embedded in a glassy matrix. The grain seems to have a twinned structure, as has been observed by others in the orthophosphates (*34*). This could not be confirmed: in-depth structural analysis of this grain was not possible due to the fact that it was quickly damaged by the focused electron beam.

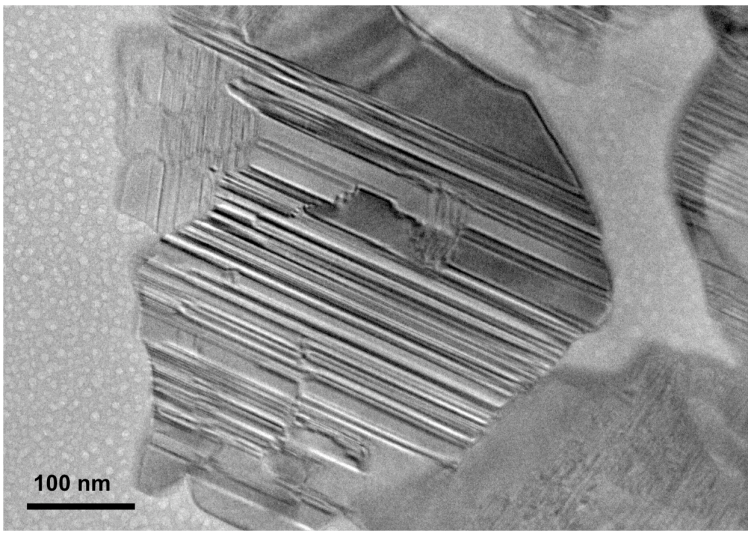

Figure 2.17. TEM image of a bulk CeP_3O_9 glass-ceramic grain.

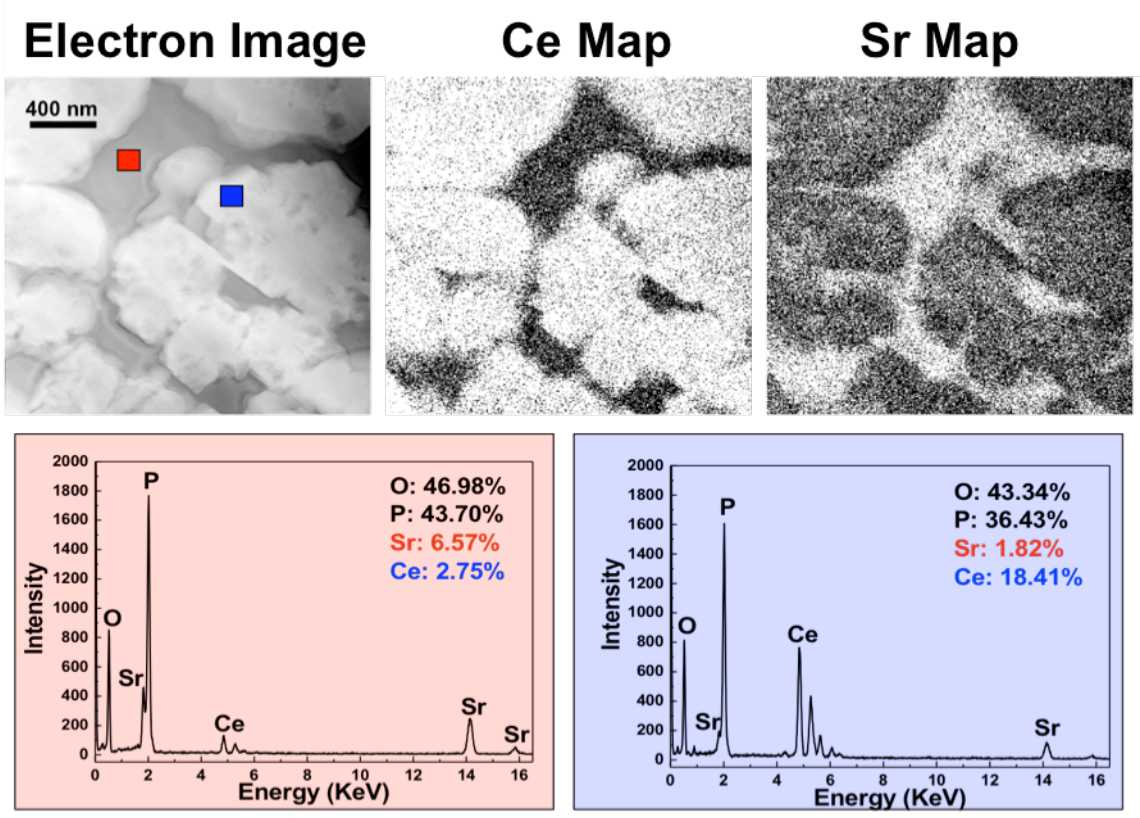

Figure 2.18. (a) Electron image of the 16% Sr-doped glass-ceramic composite. (b) Spatially resolved elemental map of the same image, showing that the crystalline phase has a higher concentration of Ce atoms than the amorphous phase. (c) Spatially resolved elemental map of the same image, showing that the amorphous phase has a higher concentration of Sr atoms than the crystalline phase. (d) EDX map of the amorphous phase, showing its Sr enrichment. (e) EDX map of the crystalline phase, showing the higher Ce content and lower Sr content.

The TEM image in Figure 2.18 reveals that the sample has two different domains: a glassy one and a crystalline one. Based on the principle of Z-contrast imaging (higher atomic number, stronger intensity), it is clearly seen that the crystallized phase is Ce-rich and the glass phase is Sr-rich. The local chemical composition of each phase was obtained using an EDX "point" measurement (blue and red square areas in the electron image) with a focused electron beam (1.2 nm) in STEM mode. The EDX plots for each phase are pictured below the elemental maps, colored red and blue for the glassy and crystalline phase, respectively. The spectrum from the glass matrix shows a high content of Sr, P, and O, and a small amount of Ce is also present. In contrast, the spectrum from the area containing crystallites presents a dominant Ce, P, and O concentration. It is important to emphasize that the Ce-rich crystallite phase and the Sr-rich glass phase still contain small amounts of Sr and Ce, respectively.

Though the cerium metaphosphate glass-ceramic samples demonstrate a new way of attaining high densities without decomposition, the lack of reproducibility and composite nature of the samples are important concerns that limit this technique. Conductivity measurements are not shown or discussed here in depth, but general statements about

them can be made. Conductivity measurements depended very strongly on the microstructures of the samples. Glass-ceramics had orders of magnitude higher conductivity than glasses, but the relationship between conductivity, doping and crystallization was not always clear. If too much residual glass was present in a sample, the conductivity was lower than expected. Sample conductivity increased if a dopant was added, but a trend between the dopant concentration and conductivity was not observed. This could be because the amount of Sr expelled from the crystallites during the heat treatment was uncontrolled.

2.3.5 CeP_3O_9-ceramic hydrate

The final sample synthesized in this study was the cerium metaphosphate hydrate powder. It was obtained using the same method as Nahdi et al. (*16*) and Serra (*20*). The XRD spectrum pictured in Figure 2.19 showed that the crystal structure matches JCPDS card 25-0159, which is distinct from the metaphosphate samples synthesized by Amezawa or by our group using the glass-ceramic process. The literature shows that CeP_3O_9 can exist in many different geometries—the one synthesized here is a ring structure (tricyclophosphate hydrate) rather than the orthorhombic cell with helical chains matching JCPDS 33-0336. Still different structures can be obtained if the metaphosphate is synthesized by dehydration. Nahdi et al. show that under flowing nitrogen, dehydration of this hydrate can yield the orthorhombic metaphosphate, but that setting a higher partial pressure of water over the sample as it is dehydrated can lead to an entirely new phase.

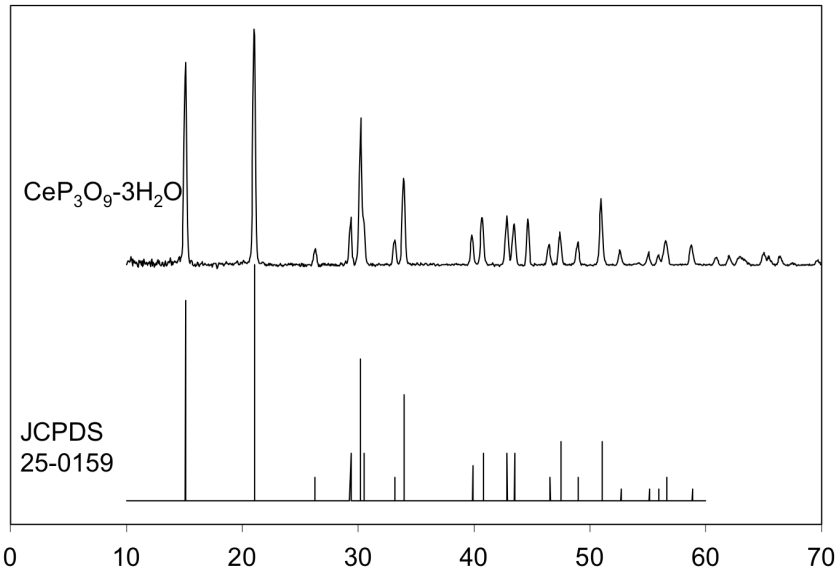

Figure 2.19. XRD pattern for the cerium metaphosphate powder synthesized by precipitation from $CeCl_3$ and sodium metaphosphate hydrate. The CeP_3O_9 $3H_2O$ hydrate is obtained, which matches JCPDS 25-0159.

2.3.5.1 Summary of CeP_3O_9-ceramic hydrate synthesis and characterization

The CeP_3O_9 hydrate is attainable using a different synthesis route than was used by Amezawa et al. (*30*) This route led to a different crystal structure. The preliminary sample

obtained in this work decomposed at very low temperature, 350°C. Further work would need to be done to optimize this composition.

2.4 Spectroscopic studies

The final section of this chapter compares the vibrational structures of the ortho-, pyro-, and metaphosphates synthesized in this study. Vibrational spectroscopy is a useful probe for characterizing the short-range structures in a material. Different molecular structures have different symmetries, and therefore should give distinct normal modes (resonant frequencies) of vibration. In this study, the pyrophosphates (PO_3-O-PO_3) and the metaphosphates (PO_3-O-PO_2-O-PO_3) are compared to the doped orthophosphates (PO_4). The Raman spectra are dominated by these vibrations within the anions: metal-oxygen bonds do not make a large contribution due to their ionic nature. This comparison of the Raman spectra resulted in partial confirmation of the pyrophosphate defect structures predicted by Amezawa et al.

2.4.1 Raman spectroscopy

A Lexel 95 Ar+ ion laser operated at 488 nm and 300 mW was used to excite bulk or powder specimens. The Raman signal was captured with a Spex 1877 0.6m Triple Spectrometer equipped with a Princeton Instruments CCD detector. Data were collected and processed using Winspec software.

2.4.2 FTIR

Infrared spectra of powders were recorded in the range 400 to 1500 cm^{-1} on a Thermo Nicolet 6700 FT-IR spectrometer. Small amounts of powder samples were mixed with KBr, then pressed in a 13mm cylindrical die. Measurements were performed in transmission mode under flowing nitrogen gas.

2.5 Results and discussion of spectroscopic analyses

2.5.1 Raman spectra of phosphates

The Raman spectra of the rare earth orthophosphates have already been extensively characterized. Each peak has been matched to a specific vibrational mode by matching polarization experiments with a factor group analysis of the material's symmetries (*35*). These studies were referenced in order to analyze our spectra. Figure 2.20 (a) shows that the Raman spectra obtained for undoped $CePO_4$ are consistent with the literature. The set of strong peaks in the region 965-1075 cm^{-1} is the signature of orthophosphate compounds, because they correspond to the symmetric and asymmetric stretching of the isolated PO_4^{3-} tetrahedra. Lower energy peaks in the spectrum correspond to O-P-O bending modes.

Figure 2.20 (c) and (d) show the Raman spectra measured for CeP_2O_7 and a glass-ceramic CeP_3O_9 sample. The energies of the cerium pyrophosphate and metaphosphate normal modes were identified by Hirai et al. (*15*) in a dehydration study. These modes differ from

orthophosphates because the dominant phosphate anions in these structures have different symmetries. For the pyrophosphate, a P-O-P linkage exists which is not present in the orthophosphates. A strong peak at 1034 cm^{-1} dominates the spectrum, corresponding to the stretching mode for P-O-P. In reference (*3*), more responses from the bridging P-O-P oxygen in the region 950-850 cm^{-1} and 750-700 cm^{-1} are noted, but in this work, the intensity of the 1034 cm^{-1} peak drowns out the rest of the signal. The peaks at even lower wavenumbers (300-500 cm^{-1}) again should correspond to O-P-O bending modes in the PO_3 terminal groups of the pyrophosphate links.

For the metaphosphates, a series of peaks at 1100-1200 wavenumbers appears, which are assigned to the symmetric and asymmetric stretching of the $–PO_2–$ groups present in phosphate chains. The peak around 680 cm^{-1} corresponds to P-O-P bending harmonics. The peaks at even lower wavenumbers (300-600 cm^{-1}) again should correspond to O-P-O bending modes. Peaks for the cerium ortho-, pyro-, and metaphosphates are reported in Table 2.1.

Table 2.1. Raman peaks for various cerium phosphate species. Extra peaks (due to pyrophosphate defects in the doped orthophosphate crystal) are starred.

Species	**Energies of Peaks (wavenumbers, cm^{-1})**
Undoped $CePO_4$	325, 373, 391, 447, 512, 552, 603, 968, 989, 1025, 1056, 1073
Doped, oxidized $CePO_4$	327, 374, 392, 444, 478*, 513, 553, 571*, 604, 626*, 970, 991, 1016*, 1027, 1057, 1075
CeP_2O_7	324, 497, 514, 576, 625, 1033 (large)
CeP_3O_9 glass-ceramic	351, 462, 500, 530, 559, 685, 971, 1062, 1091, 1128, 1196, 1222, 1264

Finally, Figure 2.20(b) is the Raman spectrum of a 2% Sr-doped $CePO_4$ sample. This spectrum matches the undoped spectrum almost exactly with a few extra peaks. These peaks appear at 1010 cm^{-1}, 620 cm^{-1}, and 480 cm^{-1}. The appearance of these peaks indicates that there may be some different phosphate species present in the sample. The position of the peak at 1010 cm^{-1} is very close to the very strong pyrophosphate P-O-P stretching peak. This indicates that introduction of the dopant results in some condensation of PO_4 groups to form PO_3-O-PO_3 linkages, just as hypothesized by Amezawa et al.

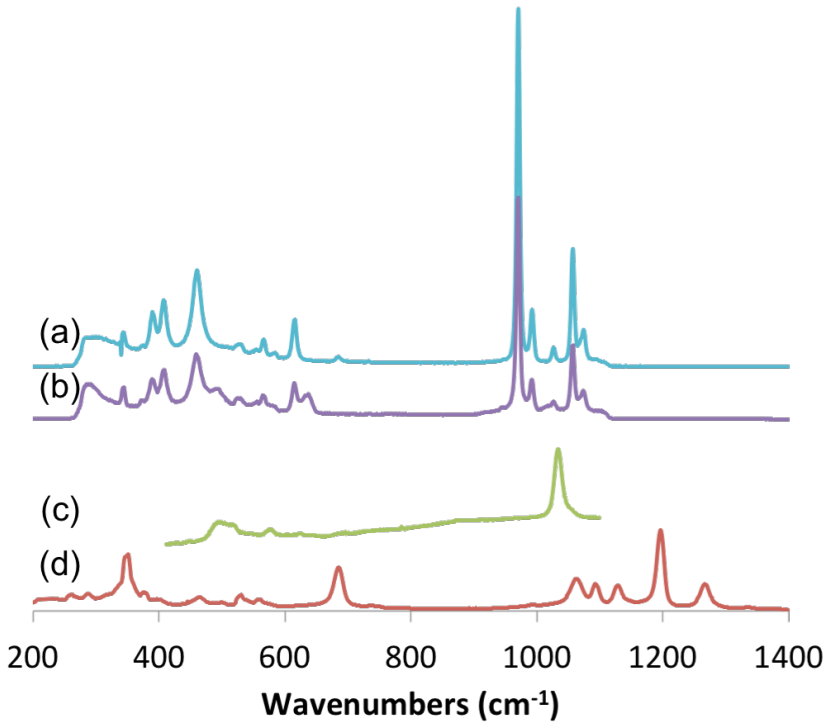

Figure 2.20. Raman spectra of (a) undoped $CePO_4$, (b) 2% Sr-doped $CePO_4$, (c) CeP_2O_7 and (d) CeP_3O_9 glass-ceramic.

To look at this peak more in depth, the Raman spectra of a series of doped and undoped orthophosphate samples treated in various atmospheres were compared at higher resolution in the region 900-1200 cm^{-1}. Figure 2.21 shows that some of the orthophosphates show an extra peak at about 1010 cm^{-1}, and some of them do not. As noted before, this peak is thought to originate from the presence of pyrophosphate linkages; the peak probably corresponds to the same P-O-P stretching mode that gives a very strong peak in this region in the CeP_2O_7 Raman spectrum. No extra peaks were noted at the higher wavenumbers, where peaks characteristic of the metaphosphate $-PO_2-$ linkages would appear.

The extra peak only appeared for samples that (1) were doped and (2) were treated in air. In Figure 2.21, the peak is visible for (a), (c), (d), and (g). This is as expected, because the pyrophosphate defects should only form in order to charge-compensate for aliovalent dopants. Undoped samples may have pyrophosphate defects as a native defect, but the concentration of them should be much lower. In addition, this pyrophosphate defect should only dominate over hydrogen-phosphate groups in samples treated in dry, oxidizing conditions. For samples treated by H_2, the pyrophosphate defect is thought to be "hydrated:" the P-O-P bonds are broken, and replaced by protonated PO_4 groups. Thus, the extra peak only appears in the samples in which it would be expected to appear, following the defect model.

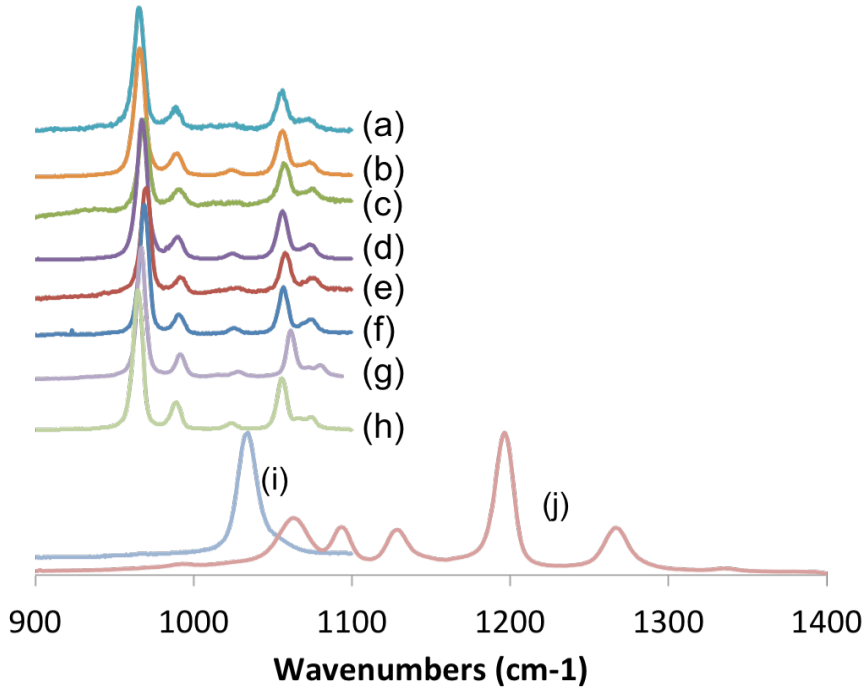

Figure 2.21. Raman spectra of (a) $La_{0.69}Ce_{0.29}Sr_{0.02}PO_4$ treated in air, (b) $La_{0.69}Ce_{0.29}Sr_{0.02}PO_4$ treated in humidified hydrogen, (c) $La_{0.29}Ce_{0.69}Sr_{0.02}PO_4$ treated in air, (d) $La_{0.29}Ce_{0.69}Sr_{0.02}PO_4$ treated in humidified hydrogen, (e) $Ce_{0.98}Sr_{0.02}PO_4$ treated in air, (f) $CePO_4$ treated in air, (g) $La_{0.98}Sr_{0.02}PO_4$ treated in air, (h) $LaPO_4$ treated in air, (i) CeP_2O_7, (j) CeP_3O_9 glass-ceramic.

Amezawa et al. noted a few additional extra peaks at lower wavenumbers in the Raman spectra indicative of other P_2O_7 bending modes; however, these were not seen here. Amezawa et al. also took Raman spectra of reduced samples, and noted peaks that might correspond to HPO_4 moieties, but these also were not observed here. This could just be due to low concentrations of defects in our sample, and low intensities of the defect peaks drowned out by the strong sample signal.

2.5.2 FTIR

Characteristic FT-IR spectra of the cerium metaphosphates, pyrophosphates, and orthophosphates are shown in Figure 2.22. The spectra agree with the literature and the normal modes for the different phosphate anions are consistent with those discussed for the Raman spectra. There is a good deal of overlap between the strongest peaks from the CeP_2O_7 and the $CePO_4$. This means that this method is not good for identifying mixtures of these two phases. Better resolution was attained using the Raman measurement. Peaks are reported in Table 2.2.

Table 2.2 FTIR peaks for various cerium phosphate species.

Species	**Energies of Peaks (wavenumbers, cm^{-1})**
CeP_3O_9	455, 533, 569, 684, 771, 953, 1057, 1154, 1274
CeP_2O_7	531, 739, 944, 1072
$CePO_4$	538, 561, 576, 618, 952, 992, 1032, 1092

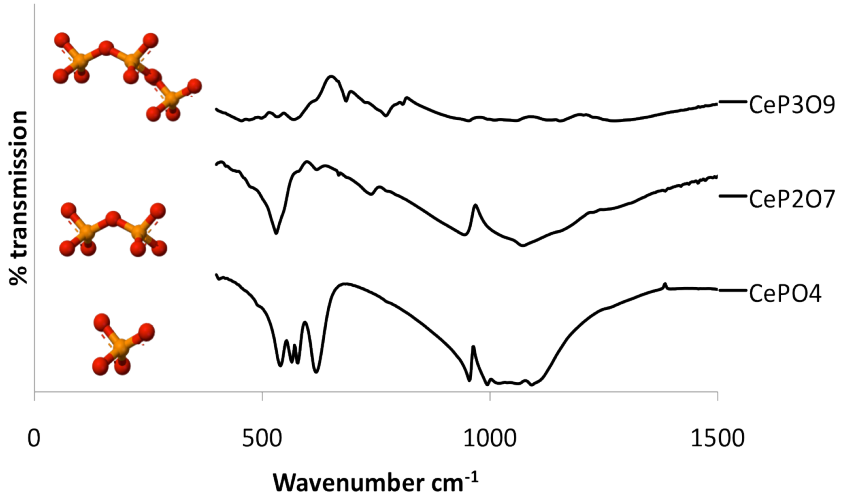

Figure 2.22. FT-IR spectra of cerium metaphosphate glass-ceramics, cerium pyrophosphates, and cerium orthophosphates. For illustration, the various phosphate anions are depicted next to their IR spectra.

As shown in Figure 2.23, FT-IR spectra of the lanthanum orthophosphate series discussed in section 2.3.1.1 showed some broadening of the strong PO_4 stretching peaks around 1000 cm^{-1} for samples precipitated at pH=5 and pH=6. This broadening may be caused by the presence of high concentrations of amorphous phosphates, as was pictured in Figure 2.3. However, the amount and chemical makeup of these phosphates cannot be determined using this technique. Further experiments, pairing this technique with thermogravimetry and differential scanning calorimetry (TGA-DSC) measurements and chemical analysis, could give more insight into the chemistry of orthophosphate synthesis.

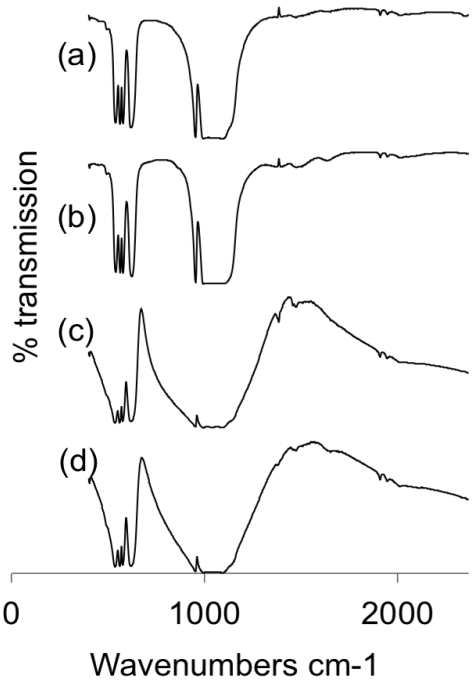

Figure 2.23. FT-IR spectra of $LaPO_4$ precipitated at (a) pH=3, (b) pH=4, (c) pH=5, and (d) pH=6. The peaks appear at the same energies, but there is a good deal of broadening for the samples synthesized at high pH.

2.6 Conclusions

A full understanding of the common microstructures and defect structures in a material system is needed before attempting to interpret transport measurements, because these define its conductivity. In this chapter, the cerium and lanthanum orthophosphates, pyrophosphates, and metaphosphates were synthesized using many different routes, and characterized using x-ray diffraction, electron microscopy, and vibrational spectroscopy.

The rare earth orthophosphates are simple to synthesize and were stable to high temperature processing. Characteristic imperfections in these samples are amorphous phosphate-rich phases, and dopant segregation. These can adversely affect the microstructures by causing runaway grain growth or giving rise to second phases. These microstructural considerations must be controlled or taken into account when interpreting the conductivity data. Doping these samples introduces pyrophosphate defects, which are detectable using Raman measurements. This is consistent with Amezawa's defect model.

CeP_2O_7 was successfully synthesized, but only retains its phase up to 600°C. Above this temperature, the material decomposes, with loss of volatile P_4O_{10}, to a mixture of monazite and orthorhombic metaphosphate phases. Conductivity measurements of a 75% dense CeP_2O_7 sample were quite low. Claims of higher proton conductivity in materials with this crystal structure should be attributed to residual phosphoric acid surface phases. Raman spectroscopy of this material reveals a very intense characteristic peak at $1034cm^{-1}$. The presence of this pyrophosphate moiety can be tracked using this technique.

Cerium metaphosphate glass-ceramic samples are formed by annealing cerium phosphate glasses above 700°C. Crystalline grains grow from the surface of the sample in toward the center of the disk. The final samples are mixtures of glassy and crystalline phases, with the resistive glassy phase enriched in the dopant. The problems with reproducibility and resistive phases make this synthesis route unpromising. Vibrational studies of this sample show characteristic Raman peaks between 1100-1200 cm^{-1}, corresponding to chains of -PO_2- species.

Metaphosphates can take on several different crystal structures. The CeP_3O_9 hydrate is successfully obtained in this work, but it decomposes at 350°C. Different synthesis routes for making these compounds should be pursued and compared.

The main defects in all of these samples are residual amorphous phosphates. These are difficult to identify when they are present in small amounts, but they strongly affect the conductivity of samples. A careful study of these phases should be carried out using the parallel TGA-DSC-MS technique, in which information about the weight loss, phase transition temperatures, and evolved volatile species can be collected. Since phosphate materials are used for other electrochemical applications such as battery cathodes, and catalysts, such a study would be valuable to many materials research fields.

Chapter 3

Identification of the charge carriers in Sr-doped $LaPO_4$ and $CePO_4$

3.1 Introduction

3.1.1 Mixed Conduction

Electrical conduction in ionic solids occurs via the flow of charge carriers such as electrons, electron-holes, or ions in response to a gradient in their electrochemical potential. Under certain gaseous environments it is possible for multiple types of charge carrier to be thermodynamically stable in a material. When both electronic and ionic charge carriers flow in a material at the same time, it is a mixed ionic and electronic conductor (MIEC). When studying mixed conduction, it is of interest to determine the relative contributions of different charge carriers to the total current. To measure the partial current density of a selected charged species, a combination of experimental methods must be used.

The techniques used for determining the ionic contribution to the total current take advantage of the fact that ions have distinct chemical identities and reactivity, occupy specific physical positions in solid materials, and have much larger masses than electrons. Common transport measurements include ac impedance spectroscopy or various dc techniques (*1-3*); electromotive force (emf) measurements (*4*) gas permeation (*5, 6*); thermogravimetric analysis (*7*); and secondary ion mass spectrometry (SIMS) (*8*). Isotopes of charge carriers (deuterium for hydrogen, ^{18}O for ^{16}O) are often used in the above techniques to definitively identify certain ionic carriers. In almost all of the above techniques, samples are equilibrated in atmospheres with various controlled partial pressures of oxygen, hydrogen, and water in order to define the relative carrier concentrations.

3.1.2 Rare Earth Phosphates

Sr-doped $LaPO_4$ and $CePO_4$ are isostructural, but have different conduction properties due to their different dominant charge carriers. This makes them a good model system for studying the fundamentals of mixed protonic and electronic conduction. It is important to understand the transport characteristics of these two materials before moving on to experimenting with the alloys $La_{0.98-x}Ce_xSr_{0.02}PO_4$. However, it is often challenging to measure the transference numbers (the fraction of the charge carried by a particular charge carrier), even for the simplest systems.

Specifically measuring the protonic current in rare earth orthophosphates is difficult because of the generally low carrier concentration. ^1H MAS-NMR measurement confirms this low proton content (*9*). There are several reasons for this. The dopants have extremely

low solubility: adding more than 2 mol % Sr to the system gives rise to the crystalline second phases $SrCe(PO_4)_3$ and $SrLa(PO_4)_3$. Even at doping levels of 2% and less, the dopant tends to segregate to amorphous grain boundary phases (*10-12*). Thus, the bulk doping level of this material system is about 1.5 mol% (*11*); this is very low compared to oxygen ion conductors with the fluorite structure, which can be doped 10-20 mol %. The low doping level sets the number of effective negative charges in the crystal: it defines an upper bound for proton content. Protonic charge carriers compete with oxygen vacancies and electron-hole defects to compensate these effective negative charges. As discussed in Chapter 1, oxygen vacancies in this system are manifested as pyrophosphate moieties, which are not very mobile. The insertion of protons requires transport of the pyrophosphate defects to the sample surface, thus creating a kinetic hindrance for protonic defects to replace oxygen vacancies (*i.e.* the pyrophosphate links), even when it is exposed to conditions in which they should be thermodynamically favored. Finally, even when protons are incorporated, there is a strong electronic attraction between the protons and the effective negative charges surrounding the dopants—this causes some of the protons to be trapped near the dopant sites (*13, 14*).

Due to the above considerations, the precise characterization of the ion transport was difficult. The sensitivities of most of the commonly used measurements were too low. For attempted TGA measurements, there was not enough of a mass change to overcome the noise levels. Preliminary SIMS measurements of water-treated samples proved difficult to interpret due to the complexity of the ionic compounds released. Gas permeation measurements were not attempted due to the low conductivity of the material and difficulty of setting up and calibrating the residual gas analyser. DC measurements with blocking electrodes (Hebb-Wagner polarizations) were also inconclusive since making electrodes that completely block protons is difficult.

The characterization techniques that did work for the Sr-doped $LaPO_4$ and $CePO_4$ samples were AC and DC conductivity measurements, and thermopower measurements. Although it was not possible in this work to determine exact transference numbers for proton, oxygen, or electronic conduction, each of these techniques yielded a good deal of information about the characteristic behavior of the system. AC impedance measurements of the samples in equilibrium with controlled atmospheres allowed us to distinguish between bulk and grain boundary responses. Qualitative observation of the line shapes of the Nyquist plots allowed us to distinguish between dominant protonic vs. electronic charge carriers. Varying the humidity and H/D isotopes confirmed the identity of the dominant charge carriers. DC measurements gave the total conductivity of the sample, with no differentiation between bulk and grain boundary; however, the advantage of DC measurements was that they could be taken as a function of time. Thus, transient changes in current on changes in atmosphere could be tracked. An estimate of the carrier concentration present in the material could be calculated by fitting the transients. Finally, a thermopower experiment was carried out in order to determine the sign of the electronic charge carrier and the mechanism of electronic conduction. The results from each of these experimental techniques will be discussed.

3.2 Experimental

3.2.1 AC impedance Measurements

Platinum mesh electrodes were attached to the sintered pellets using platinum paste (Heraeus). Total conductivity measurements of the $La_{0.98}Sr_{0.02}PO_4$ and $Ce_{0.98}Sr_{0.02}PO_4$ samples were taken in ambient air using the 2-probe ac impedance technique using a Bio-Logic SP-150 / VSP / VMP3 potentiostat. The frequency was varied from 1 MHz to 0.1 Hz, and the alternating voltage amplitude was 25 mV. Impedances were measured for the full series of samples between 350 and 600°C in air with 3% humidity, air with 6% humidity, and in H_2 gas with 3% humidity, and D_2 gas with 3% humidity of D_2O.

All impedance data were fitted to the usual equivalent circuit using the Levenberg-Marquardt algorithm in the software package EC-Lab (BioLogic). For sintered ceramic materials with randomly oriented bulk grains and grain boundaries, the Nyquist plot generally displays responses reflecting this microstructure. The standard equivalent circuit for a mixed ionic and electronic conductor is shown in Figure 3.1a, and the ideal Nyquist plot for this equivalent circuit is shown in Figure 3.1b. For each sample, one pathway (ionic or electronic) is assumed to dominate over the other. The high frequency arc in the impedance plots was assigned to the bulk grains, the lower frequency arc was assigned to the grain boundary, and additional responses at very low frequency were attributed to electrode processes (*15*). Semicircles tended to be slightly depressed, due to inhomogeneities of current distribution. Because of this, the capacitors in the model equivalent circuit were replaced by constant phase elements, Q (*16*).

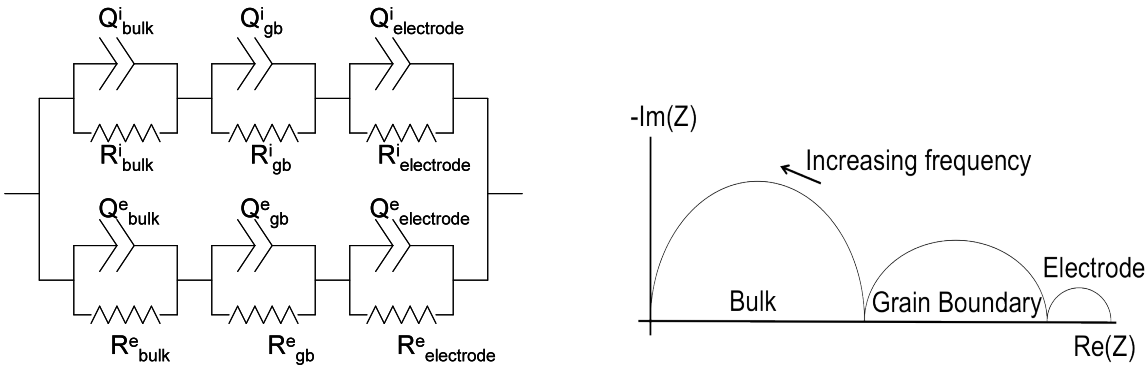

Figure 3.1 (a) Full equivalent circuit for a mixed ionic and electronic conducting ceramic. (b) Ideal Nyquist plot for one branch of the circuit depicted in (a). Each semicircle corresponds to a different RC element of the full equivalent circuit.

The line shapes of the experimentally measured responses in the complex impedance plane were fitted using subsections of this full circuit, since not all bulk, grain boundary, and electrode responses were visible and interpretable under all conditions. For example, the bulk resistance for conduction in $Ce_{0.98}Sr_{0.02}PO_{4-\delta}$ and other Ce-rich compositions in air were apparent in the measured frequency range for temperatures below 350°C, but moved out to much higher frequencies at higher temperatures. In these cases, the bulk response was estimated by measuring the high frequency intercept of the grain boundary response.

For very resistive samples, especially those containing high fractions of La and measured at lower temperatures, the response at low frequencies became too noisy to interpret.

3.2.2 DC conductivity measurements

Sintered $La_{0.98}Sr_{0.02}PO_4$ and $Ce_{0.98}Sr_{0.02}PO_4$ samples 0.5-1mm thick and 12mm in diameter were painted with Pt paste electrodes and Pt contacts. Samples were placed inside of a home-built alumina tube test rig. This test rig had ports for gas in and gas out, Pt wires for electrical contact, and a thermocouple placed close to the sample. It allowed the sample to equilibrate with one gaseous environment supplied by the gas line, and positioned the sample in the center of a tube furnace.

The Bio-Logic potentiostat/galvanostat and EC-Lab software were used for the DC measurements. To track changes in conductivity with changes in atmosphere, chronoamperometric measurements were used, in which a constant potential of 700mV was applied and the current measured as a function of time. The samples were first equilibrated at a selected temperature and controlled atmosphere for at least half a day. The chronoamperometry test routine was loaded, and after 2-5 minutes of measuring the current at this first controlled atmosphere, the gas lines were suddenly switched out: the different possible gas lines were ambient air, argon, and 4% H_2, balance Ar. All gases were bubbled through water at room temperature, which set the humidity to be 3%. Changes in current were monitored as a function of time.

3.2.3 Thermopower measurements

A thermopower measurement was carried out on a 1mm x 5mm x 5mm $Ce_{0.98}Sr_{0.02}PO_4$ sample in a home-built test rig. The sample was measured after sintering in air at 1200°C, with no treatment in humidified air or hydrogen. The test rig consisted of a vacuum chamber with two small controllable heaters inside, and electrical contacts.
Silver paste was painted onto the corners of the sample for thermal contact, and each end of the sample was placed on one of the heaters. Electrical probes were attached to each end of the sample as well. Measurements of the thermal voltage were taken under low vacuum. The temperature difference between the heaters was kept constant at 5°C, but the temperature of measurement was varied between 300-500°C. The measured Seebeck coefficient was +230uV/K for all temperatures. The same measurement was attempted for an undoped $CePO_4$ sample, but the conductivity of this sample was too low, and the thermopower could not be detected by the equipment.

3.3 Results and Discussion

3.3.1 AC Impedance

The frequency-dependent impedance responses for the $La_{0.98}Sr_{0.02}PO_4$ and $Ce_{0.98}Sr_{0.02}PO_4$ samples were plotted on the complex plane (Nyquist plot) in the standard manner, with the

real component plotted on the abscissa and the imaginary component on the ordinate axis. The usual Nyquist plot for these samples consisted of two depressed, overlapping semicircles and a low-frequency electrode response, as noted in the experimental section. The high-frequency bulk response was fitted for analysis and for comparison across samples and across gaseous atmospheres. The bulk conductivity of all samples in all atmospheres displayed Arrhenius behavior with respect to temperature: this shows that the dominant charge carriers under all conditions move via temperature-activated transport mechanisms.

Observation of the Nyquist plots for the $La_{0.98}Sr_{0.02}PO_4$ and $Ce_{0.98}Sr_{0.02}PO_4$ samples showed that the relative magnitudes of the bulk and grain boundary responses, as well as the degree of overlap of the two semicircles, were quite different depending on the sample and the atmosphere. This qualitative difference in line shape, as well as changes in activation energy and total resistance, indicate that there is a change in dominant charge carrier in this system.

3.3.1.1 $La_{0.98}Sr_{0.02}PO_4$ Nyquist Plots

Nyquist plots for the $La_{0.98}Sr_{0.02}PO_4$ composition in 3% humidified air intercept the origin at high frequencies, and show a large, high frequency bulk semicircle overlapped with a smaller, low frequency grain boundary semicircle. The plots shown in Figures 3.2-3.4 come from different samples; hence, the resistances differ between plots. However, within each plot the sample is the same. The increase or decrease in resistance with each change in atmosphere is consistent for each plot. As shown in Figure 3.2, changing from 3% to 6% humidity leaves the qualitative line shape the same, but leads to a small decrease in resistance. In Figure 3.3, we see that changing from 3% humidified air to 3% D_2O in air led to a slight increase in resistance. This is as expected from the literature (*17*) The classical model, which relates the diffusivity of protons to the vibrations given by the reduced mass of the O-H or O-D oscillator, would give the ratio of the sample conductivity to be about 1.4:1. However, this can vary due to non-classical effects such as differing activation energies and some dependence on the O dynamics in the crystal (*17*).

When the atmosphere is changed from air to 3% humidified hydrogen gas, the general line shape of the Nyquist plot shown in Figure 3.4 does not change; however, the measured resistance decreases even further, due to increased carrier concentration. These responses to changes in atmosphere indicate that the dominant charge carrier leading to the impedance response in $La_{0.98}Sr_{0.02}PO_4$ is protonic. This is consistent with the proposed defect model discussed in Chapter 1. The activation energy for proton transport in this sample was around 1 eV.

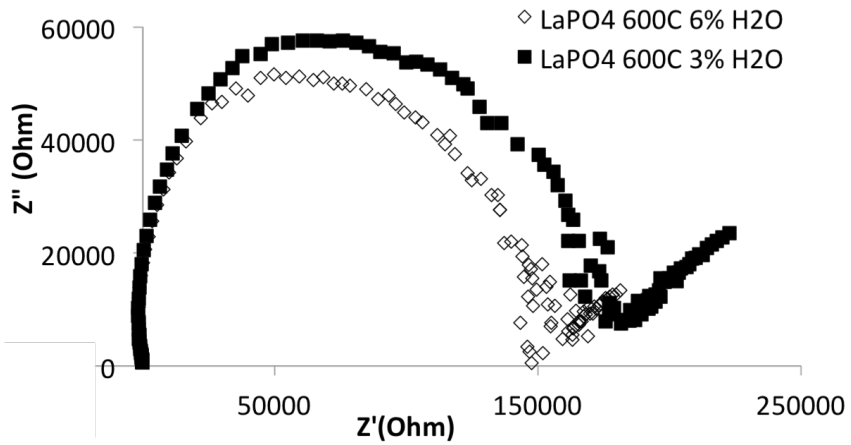

Figure 3.2. Nyquist plot for La0.98Sr0.02PO4 measured at 600°C in 3% vs. 6% humidified air. The total resistance of the sample decreases with increased humidity.

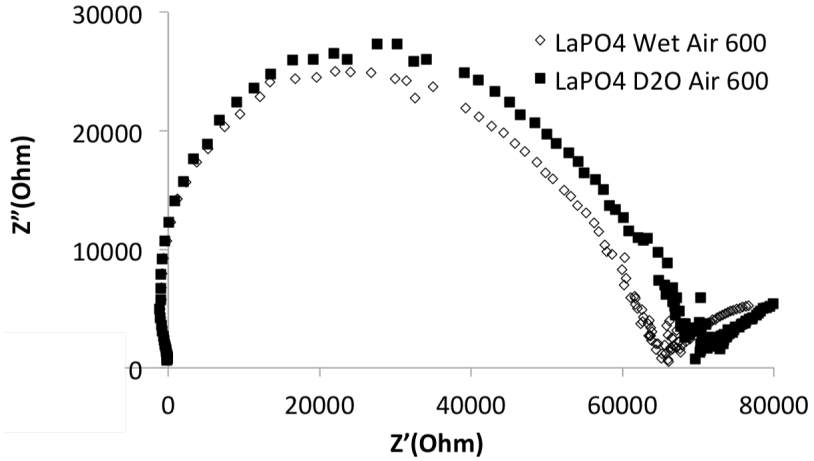

Figure 3.3. Nyquist plot for $La_{0.98}Sr_{0.02}PO_4$ measured at 600°C in air with 3% H_2O vs. 3% D_2O. The total resistance of the sample is higher for the atmosphere containing heavy water.

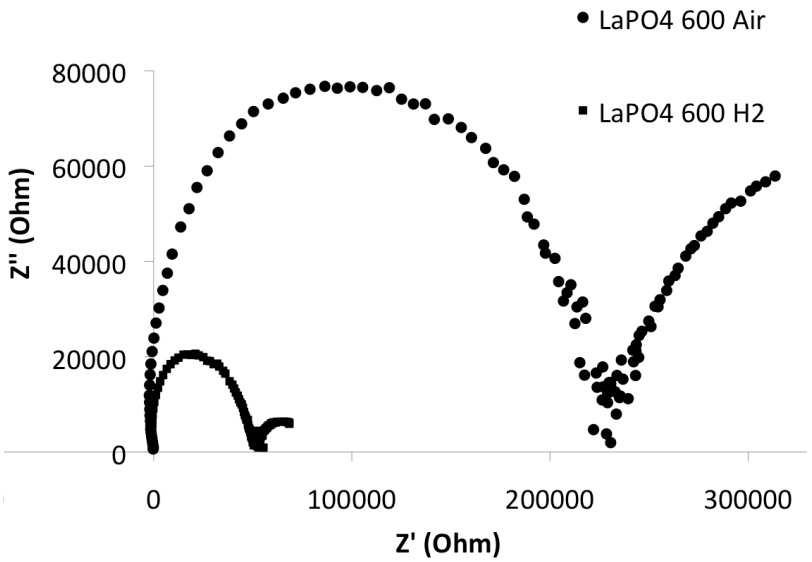

Figure 3.4. Nyquist plot for the $La_{0.98}Sr_{0.02}PO_4$ sample measured at 600°C in 3% humidified air vs. 3% humidified H_2. The resistance decreases dramastically for the measurement taken in reducing conditions.

3.3.1.2 $Ce_{0.98}Sr_{0.02}PO_4$ Nyquist Plots

The characteristic line shapes for the $Ce_{0.98}Sr_{0.02}PO_4$ composition in humidified air are shown in Figure 3.5. They are qualitatively different from the $La_{0.98}Sr_{0.02}PO_4$ samples. The bulk arc is now smaller than the grain boundary arc, and the bulk and grain boundary arcs are more distinct. Both arcs are visible at the lower temperatures measured, but at higher temperatures, the response from the bulk moves to higher frequency and this bulk arc is no longer visible in the frequency ranged measured. However, the grain boundary arc is still visible at higher temperatures, and the high frequency intercept of this arc moves to lower resistances as the temperature increases. The bulk resistance was estimated to be equivalent to the grain boundary arc's high frequency intercept. The fact that the bulk and grain boundary responses are now more separate in frequency indicates that a fundamentally different conduction process is occurring in this sample.

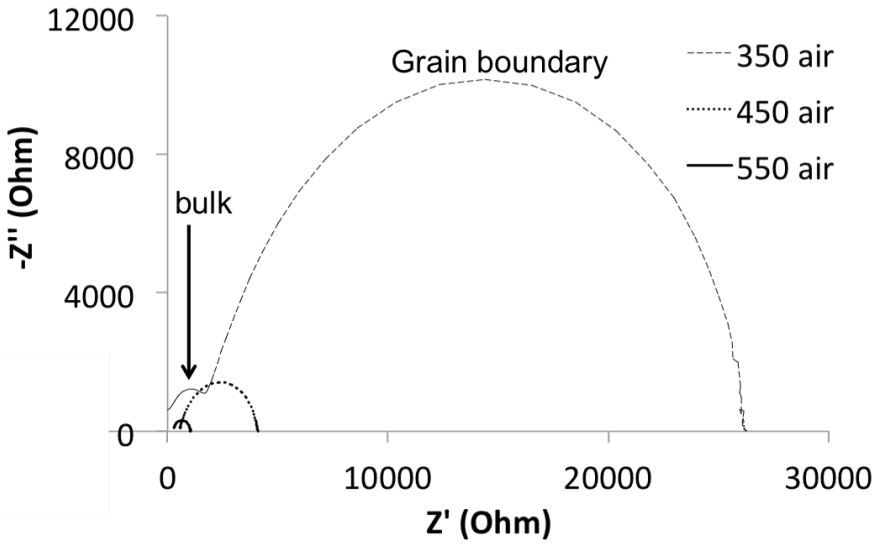

Figure 3.5. Nyquist plot for $Ce_{0.98}Sr_{0.02}PO_4$ in air at various temperatures. At low temperatures (350°C), the small, high frequency bulk response is visible and distinct from the grain boundary response. At higher temperatures, only the grain boundary responses are visible; the bulk response is out of the frequency range measured. The high frequency intercepts of the grain boundary arcs move to the left as temperature increases, giving an estimate of the bulk response.

Figure 3.6 shows that changing from 3% to 6% humidity did not give any changes in bulk resistance. In addition, changing from 3% H_2O to 3% D_2O also did not lead to any changes in bulk resistance: this is shown in Figure 3.7. These two tests show that for $Ce_{0.98}Sr_{0.02}PO_4$ in air, the dominant charge carrier is not protonic. The defect model proposes that the charge carrier is actually electronic—conductivity in this material is due to hopping of an electron-hole between Ce cations, which can be in the 3+ or the 4+ valence state. This is further supported by the measurement of the activation energy at 0.60 eV—lower than that for proton transport in the lanthanum phosphates.

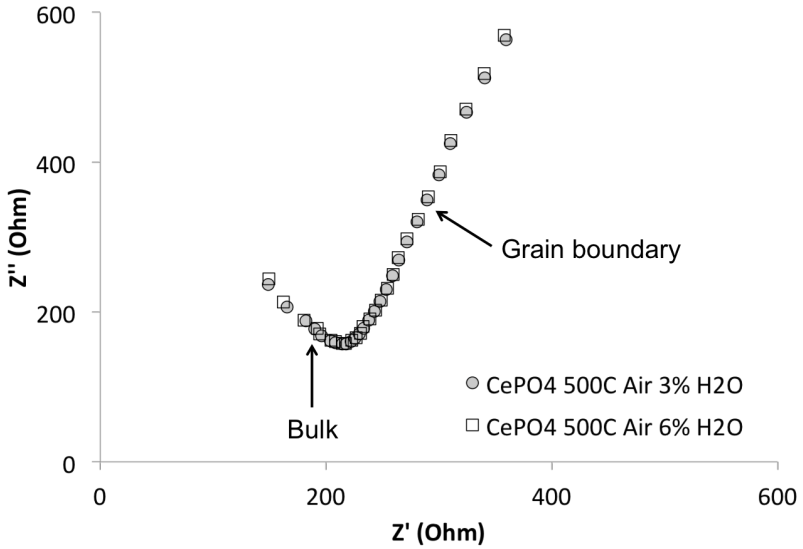

Figure 3.6. The high frequency bulk response for the $Ce_{0.98}Sr_{0.02}PO_4$ material measured in air is unaffected by changes in humidity.

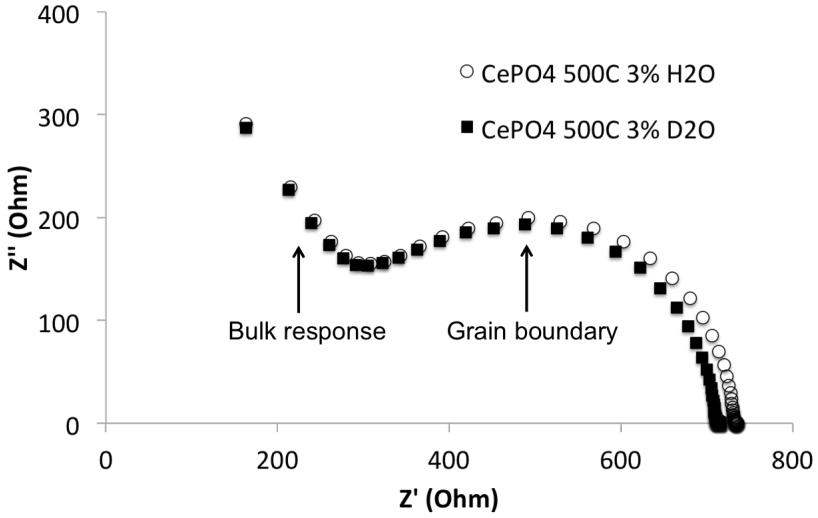

Figure 3.7. The high frequency bulk response for the $Ce_{0.98}Sr_{0.02}PO_4$ material measured in H_2O vs. D_2O is unchanged.

Upon exposure of the $Ce_{0.98}Sr_{0.02}PO_4$ sample to humidified hydrogen, the line shapes of the Nyquist plots for the sample changed dramatically. As shown in Figure 3.8, the total resistance increased by orders of magnitude after this change in atmosphere. The line shape for the $Ce_{0.98}Sr_{0.02}PO_4$ sample when in equilibrium with a reducing atmosphere looked more similar to the $La_{0.98}Sr_{0.02}PO_4$ traces: the trace starts at the origin of the complex plane, and shows a large high frequency bulk semicircle greatly overlapped with a smaller grain boundary arc. Finally, changing from 3% humidified H_2 to 3% D_2O in D_2 led to an increase in resistance. This shows that the dominant charge carrier for $Ce_{0.98}Sr_{0.02}PO_4$ in reducing conditions is protonic—this is consistent with the activation energy measured at 1.1eV.

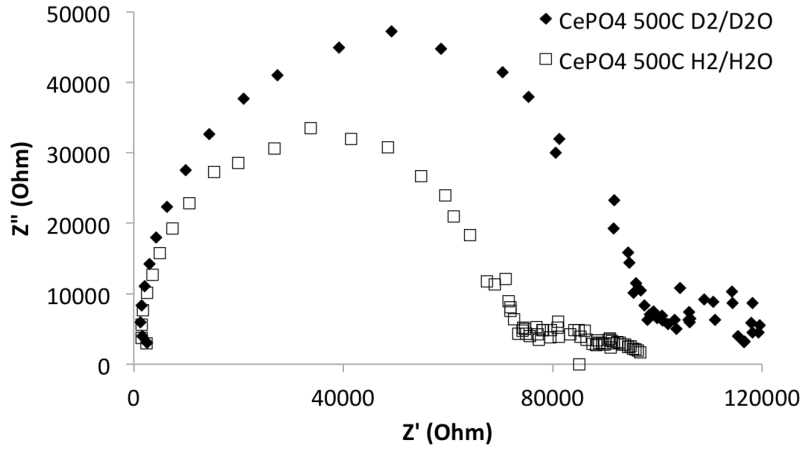

Figure 3.8. The Nyquist plot of $Ce_{0.98}Sr_{0.02}PO_4$ in reducing conditions is shaped like those measured for $La_{0.98}Sr_{0.02}PO_4$. The resistance increases upon changing from H_2 to D_2, indicating that the dominant charge carrier is protonic.

All of this demonstrates that for $Ce_{0.98}Sr_{0.02}PO_4$ in air, the dominant charge carrier is electronic, whereas for $Ce_{0.98}Sr_{0.02}PO_4$ in hydrogen, and for $La_{0.98}Sr_{0.02}PO_4$ in air and in hydrogen, it is protonic. The changes in line shape and total resistance for $Ce_{0.98}Sr_{0.02}PO_4$ on switching from air to hydrogen atmosphere are caused by a change in dominant charge carrier from p-type electronic to protons. This is consistent with the literature (*18*) and is also consistent with the proposed defect model (*19*). Upon exposure to a reducing atmosphere, all Ce^{4+} cations are reduced to Ce^{3+}, and protons are incorporated instead, according to the defect reactions 1.17-1.18 in Chapter 1. The p-type electronic carriers can no longer exist under reducing conditions; therefore the incorporated protonic carriers dominate the total conduction.

3.3.2 DC transients

DC measurements were also used to confirm the defect model for the $La_{0.98}Sr_{0.02}PO_4$ and $Ce_{0.98}Sr_{0.02}PO_4$ samples. Chronoamperometry measurement routines set a potential, and measure the current as a function of time. If the gas environment is suddenly changed during the measurement, then the transient changes in current can be observed as the sample equilibrates with its new environment. These DC measurements not only can support the conclusions drawn from the AC measurements about defect equilibria, but also can give information about the nonequilibrium processes of changing the carrier concentration or carrier type.

The advantage of the DC measurements over the AC is that very small changes in current could be tracked real-time. Such small changes in conductivity would be lost in the noise of an AC impedance measurement. However, it is difficult to extract true quantitative information on kinetics from these DC measurements due to time lags in gas mixing, fluctuations in current during the measurement, and polarization from the measurement routine itself. Therefore, for most of the samples shown here, only qualitative changes are discussed: net increases or decreases in current, and the magnitude of the change.

The transient response for the $Ce_{0.98}Sr_{0.02}PO_4$ sample upon changing the gaseous atmosphere from air to 4% H_2/balance Ar was sizeable and far less noisy than the other measurements. This transient response is modeled quantitatively, and a diffusion coefficient and estimate of the carrier concentration are extracted.

3.3.2.1 DC transients of $La_{0.98}Sr_{0.02}PO_4$

First, the qualitative changes in current with atmosphere will be discussed. Changes in current for $La_{0.98}Sr_{0.02}PO_4$ were measured for switches between dry argon, 3% humidified argon, and 3% humidified 4% H_2 in argon with a 700mV applied potential at 600°C. First, the sample was equilibrated with dry argon and the current was measured. As shown in Figures 3.9 and 3.10, due to the low conductivity of this sample, the application of this very high potential only resulted in a current of 0.001 mA. Upon switching the gas line to humidified argon, the current increased to 0.002mA. The delay of several seconds in the current response was attributed to gas mixing issues—with this experimental setup it took

several seconds for the humid gas to completely displace the dry. After equilibration with the wet gas, the line was switched back to dry argon. As shown in Figure 3.11, the current decreased again, as predicted.

On switching from wet argon to the wet hydrogen/argon mixture, the same increase in current occurred, except this time the magnitude of the current enhancement was larger: the current switched between 0.001 mA and 0.003 mA. This is shown in Figure 3.12. The transient for this atmosphere change is quite sharp; this seems indicative of a critical change in the sample. The nature of this change will be discussed further in the next section. Switching back to argon led to a decrease in the current (Figure 3.13). This behavior proves that the defect reaction for protonation and deprotonation of the $La_{0.98}Sr_{0.02}PO_4$ sample is reversible, and is consistent with the defect model discussed in Chapter 1.

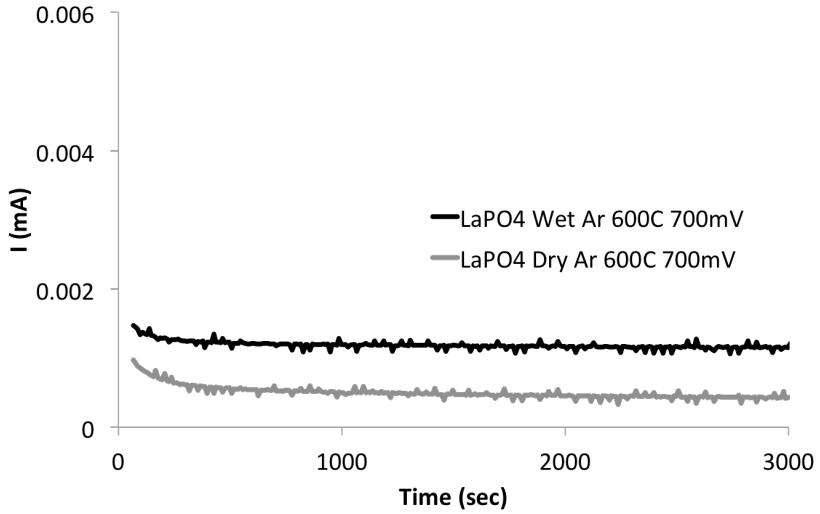

Figure 3.9. Comparison of chronoamperometry measurement of the $La_{0.98}Sr_{0.02}PO_4$ sample in dry vs. wet argon at 600°C and 700mV applied potential. The current in wet Ar is about double the current in dry Ar.

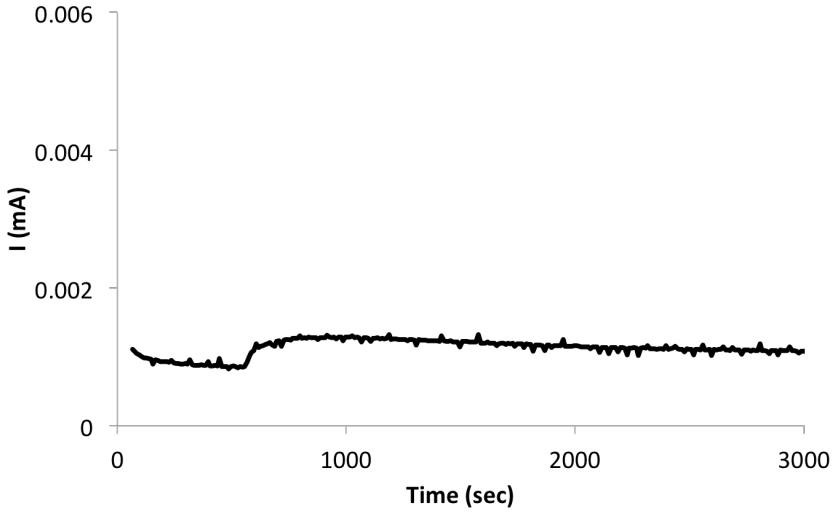

Figure 3.10. DC transient measurement of the $La_{0.98}Sr_{0.02}PO_4$ sample as the atmosphere is switched from dry to wet argon. There is a visible increase in current.

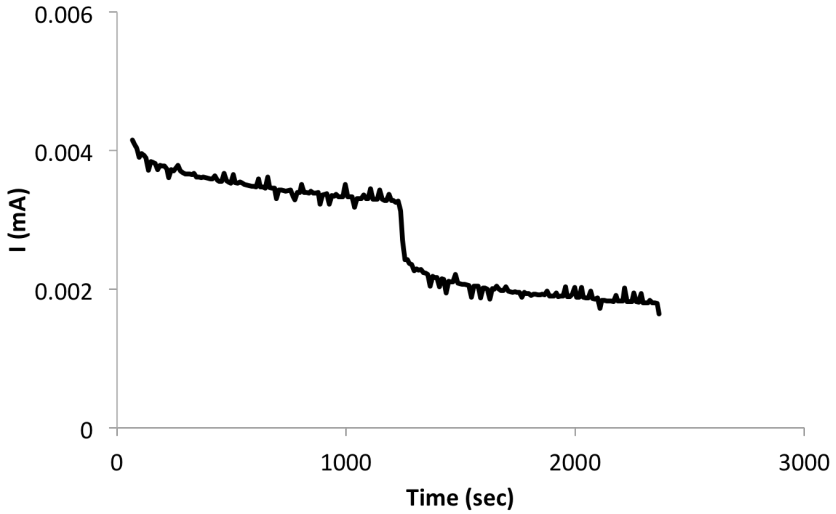

Figure 3.11. DC transient measurement of the $La_{0.98}Sr_{0.02}PO_4$ sample as the atmosphere is switched from wet to dry argon. There is a visible decrease in current.

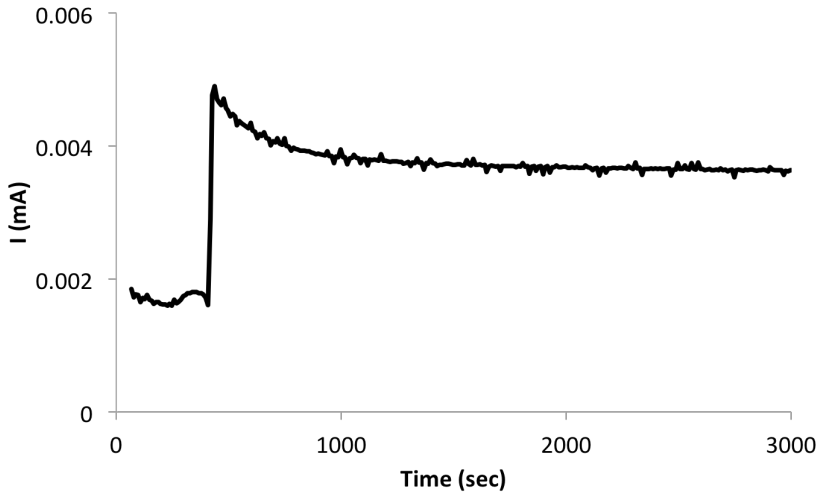

Figure 3.12. DC transient measurement of the $La_{0.98}Sr_{0.02}PO_4$ sample as the atmosphere is switched from ambient air to 3% humidified H_2. There is a short delay after the gas line is switched, followed by a sudden increase in current.

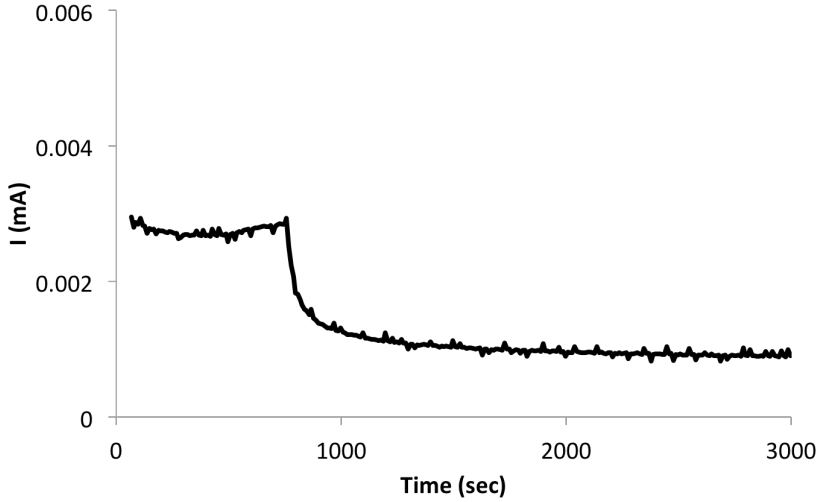

Figure 3.13. DC transient measurement of the $La_{0.98}Sr_{0.02}PO_4$ sample as the atmosphere is switched from 3% humidified H_2 to ambient air. There is a sudden, monotonic decrease in current.

3.3.2.2 DC transients of $Ce_{0.98}Sr_{0.02}PO_4$

Changes in current for the $Ce_{0.98}Sr_{0.02}PO_4$ sample were measured with the same atmosphere changes at several temperatures. In contrast to the $La_{0.98}Sr_{0.02}PO_4$ samples, switching between dry and wet argon did not lead to significant changes in current. The current level for this sample in air for the same applied potential is several orders of magnitude higher than that for the $La_{0.98}Sr_{0.02}PO_4$ sample. This indicates that a different, more mobile charge carrier is dominant in this system. As shown in Figure 3.14, upon changing the atmosphere from dry to wet Ar, there did seem to be a small change in the level of current. The magnitude of the observed current change was on the same order of magnitude as for the $La_{0.98}Sr_{0.02}PO_4$ sample (microamperes). However, it was noted that

there was also some variation between measurements taken in dry atmosphere, and the change in current observed on changing from wet to dry was on the same order as these differences. Thus, protonic charge carriers are not the main contributor to the current in argon, dry or wet. The changes are so small that even if they are caused by proton incorporation, they are insignificant changes compared to the total conductivity or total current.

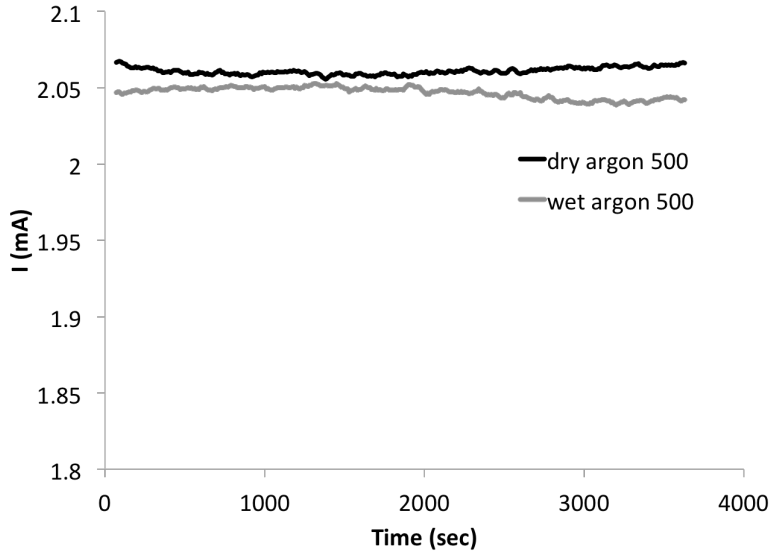

Figure 3.14. Comparison of chronoamperometry measurement of $Ce_{0.98}Sr_{0.02}PO_4$ in dry vs. wet argon at 500°C and 700mV applied potential. The current in wet Ar is measured to be slightly lower than the current in dry Ar; however, it is not a significant difference and is not a large fraction of the total current.

Finally, we consider current transients in the $Ce_{0.98}Sr_{0.02}PO_4$ sample for changes between air and 4% H_2 in Argon. These are depicted in Figure 3.15. The current starts out high as usual for measurements in oxidizing conditions. After the 4% H_2 in Ar gas line is attached, there is a delay of several minutes with a slight increase in the current level, before the current begins to drop off precipitously. The majority of the current drop occurs in just a few minutes, but it takes 12 hours or more for the current to decay completely to equilibrium with the new atmosphere. The rate of the decrease is temperature dependent—the slope of the transient is steeper for higher temperatures. After equilibration with the reducing atmosphere, the current is very low –about the same order of magnitude as the current in the $La_{0.98}Sr_{0.02}PO_4$ sample. This dramatic change in current level indicates that the dominant charge carrier has changed from electronic to protonic. The shape of the transient, and especially the delay before the dramatic drop-off, is interesting and will be discussed in the next section.

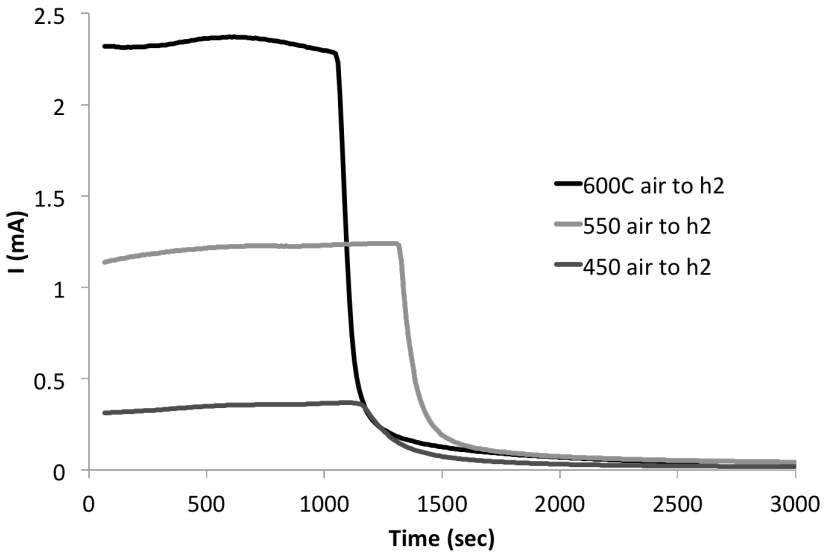

Figure 3.15. DC transient measurement of the $Ce_{0.98}Sr_{0.02}PO_4$ sample on changing the atmosphere from air to 3% humidified 4% H_2 in argon at 600, 550, and 450°C. The gas line is switched at time 0 seconds, and there is a delay of several minutes before the current drops precipitously.

The DC transient measurement for $Ce_{0.98}Sr_{0.02}PO_4$ for the change from 4% H_2 in argon back to air was carried out as well. This is shown in Figure 3.16. Two interesting characteristics of the current response were noted. First, there was no delay in current increase. As soon as the line was removed, the current began slowly increasing. The rate of increase was slow, which may be due to gas mixing processes. The second noted characteristic was that the current never reached its original level, which for this sample was 1.9 mA—instead, it leveled off around 1.3 mA. Thus, the oxidation and reduction process for $Ce_{0.98}Sr_{0.02}PO_4$ was not completely reversible, in contrast to the $La_{0.98}Sr_{0.02}PO_4$ system. One possible cause for this irreversibility in current could be slow exchange of low mobility oxygen defects. Upon prolonged exposure of the sample to H_2 gas, many holes and O vacancies may eventually be ejaculated and replaced by protonic defects. On re-oxidation, the reverse process of replacing those protons with O vacancies or holes may be slow due to frozen-in O defects.

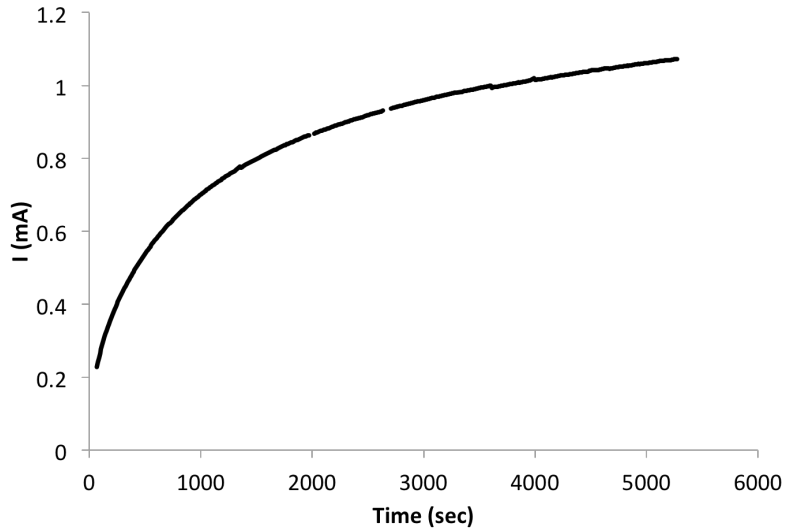

Figure 3.16. DC transient measurement of a different $Ce_{0.98}Sr_{0.02}PO_4$ sample on changing the atmosphere from reducing conditions back to air at 500°C. The original current in air was measured at about 1.9 mA; after cycling between reducing conditions, the current in air leveled off at about 1.3 mA.

There are several conclusions we can reach from these DC transient experiments. First, we confirm again the proton dominance for $La_{0.98}Sr_{0.02}PO_4$ in all conditions, and the switch between protons and electronic charges for $Ce_{0.98}Sr_{0.02}PO_4$. The variation of current with time deserves more discussion. Both materials evidence sharp changes in conduction behavior on changes between oxidizing and reducing conditions. The observed delays before step-changes in current may indicate that complete formation of a reduced electron-blocking layer is necessary before the protons become dominant over the electronic carriers.

3.3.3 Transient Model

A simple quantitative transport model for the transient reduction of $Ce_{0.98}Sr_{0.02}PO_4$ was constructed in order to extract estimates for the diffusion constant and the proton concentration.

To construct the model, some assumptions must be made about the reduction process. Samples start off in dynamic equilibrium with the oxidizing environment. Once the gas line is switched from air to 4% H_2 in argon, there is a slight delay in response due to gas mixing processes, and then the sample begins to contact the H_2 molecules. The presence of this reducing gas causes the electronic carriers at the surface, Ce^{4+}, to reduce to the Ce^{3+} valence state, and to incorporate protons (see Equations 17-18 from Ch.1) The layer of reduced material grows to cover the entire surface of the sample. When the growth of this layer is complete, there is no more contact of the oxidized, electronically conductive material with the atmosphere, and the electrochemical processes at work undergo a sharp change.

This assumption of layer growth is consistent with our previous qualitative observation of the transient behaviors. Oxidation and reduction of both the $Ce_{0.98}Sr_{0.02}PO_4$ and

$La_{0.98}Sr_{0.02}PO_4$ samples seemed to show a nonlinear change in current after a short delay. The delay can be attributed not only to gas mixing but also to the slow growth and completion of a layer of reduced material covering the entire surface of the sample.

The model assumes that the reduction of $Ce_{0.98}Sr_{0.02}PO_4$ proceeds via the growth of a reduced layer that first covers the outside surfaces of the sample and then grows in toward the center. This is depicted in Figure 3.17. The reduced layers with proton concentration (n_1) have different conduction qualities than the oxidized layer (n_2). The reduced layers should dominantly conduct protons rather than electron-holes. Exchange of the carriers in the oxidized material in the center of the sample must occur through this reduced layer. This process is slow because the thermodynamically disfavored electron-holes must travel through the reduced layer. It takes many hours for the current to equilibrate to the low conductivity associated with the pure proton conductor.

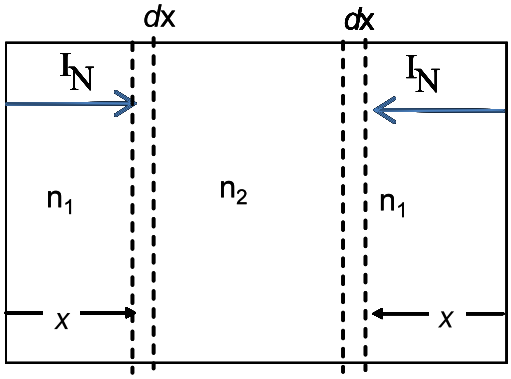

Figure 3.17. One-dimensional transport model of the two reducing layers growing into the sample. I_N is the current resulting in layer growth; n_1 is the concentration of protons in the reducing layers; n_2 is the concentration of protons in the oxidized core of the sample; x is the layer thickness; dx is the amount the layer grows per unit time.

Consider the current, I_N, that gives rise to the reduction of Ce^{4+} to Ce^{3+}, with concomitant strong lowering of the electron hole conductivity.

(3.1) $I_N = F\,(Dn)\,dx/dt = (Dn/n_1)\,V/\,(R_0\,x)$

Where F is the Faraday constant, x is the incremental change in the thickness of the layer as it grows over time, $Dn=n_2-n_1$ is the change in the number of protons, R_0 is the specific resistance of the reduced layer, and V is the open-circuit potential (discussed in Chapter 5 of this work). This definition of the V acting on the layers deserves some clarification, as does the origin of the term (Dn/n_1).

The center zone with n_2 proton content has its oxygen chemical potential established at the start of the experiment, during equilibration with air. The reduced outer layers with n_1 proton content have a low oxygen chemical potential applied at t=0. In essence, the reduced layer combined with the oxidized layer of high electronic conductivity resembles the fuel cell arrangement discussed in Chapter 5. Thus V is taken to correspond to the OCV of the Sr-doped $CePO_4$ mixed conducting membrane. This voltage, V=0.3V thus appears

over the reduced layer, and in the absence of other applied voltage determines the intrinsic rate of growth of the reduce layer, but does not produce an external current.

The voltage, V_a, applied for measuring the current is considered *not* to affect the *combined* reduced layer thickness, because although V_a would advance the one interface, it would equally slow the other, so long as V_a is less than about twice the Nernst voltage. This is a consequence of the resistive current being constant throughout the sample, which has the effect of drifting the combined reduced layers.

The term (Dn/n_1) is inserted into the expression in order to express the incremental growth of the layers into the center of the sample. The expression

(3.2) $i=V/R_0\ x$

would be the instantaneous current density for the layer of thickness x, with a total proton concentration of n_1, and specific resistance R_0, acted on by voltage V. However, only the fraction Dn/n_1 of *i* constitutes the actual Faraday reduction current, I_N. So the layer growth current must be $I_N=(Dn/n_1)i$.

From equation (3.1), we find $I_N = (Dn/n_1)\ V/\ (R_0\ x)= F\ (Dn)\ dx/dt$, or

(3.3) $R_0\ F\ n_1\ x\ dx= V\ dt$

Then, upon integration,

(3.4) $(R_0Fn_1x^2/2) = V\ t$

If we define the conductivity in the reduced layer as

(3.5) $\sigma_0\equiv 1/R_0$

then equation (3.4) can be rearranged to

(3.6) $x^2 = 2\ Vs_0/F.n_1)t$

The Nernst-Einstein relationship with protons as the conducting species is expressed as

(3.7) $\sigma_0= (n_1.D.F^2/RT)$

which is inserted into (3.6) giving

(3.8) $x^2 = 2V\ (n_1.D.F^2/RT)t/F.n_1 = 2V\ (D.F/RT)t$

The current I_R during the resistance measurements is $I_R=V_a/(2R_0x)$, and measures resistance of both layers together. The external current I_R measured as a result of applying

V_a is not affected by the internal voltage, since the internal voltage does not lead to a contribution to the current in the external circuit.

So also

(3.9) $x=V_a/(2R_0I_R)$

combined with the Nernst-Einstein relation (3.7), we obtain

(3.10) $x^2=V_a/(R_0^2 4I_R^2) = 2V\ (D.F^2/RT)t/F$ and

(3.11) $V_a^2/(R_0^2 I_R^2)=8V\ (D.F^2/RT)t/F$

Solving for Dt,

(3.12) $RTV_a^2/(8VFR_0^2\ I_R^2)= D.t$

But the term $RTV_a^2/8VFR_0^2$ is a constant for a selected temperature and constant applied voltage. Thus, I_R^{-2} should be proportional to t. This gives

(3.13) $D=[dI_R^{-2}/dt]s_0^2 RTV_a^2/(8VF)$

Plotting experimental data as $d(I_R^{-2})/dt$ *vs*. the time, we find that this is the case at later times. The long transient may be attributed to the incomplete establishment of the resistive layer. This manipulation of the transient data from Figure 3.15 above is shown in Figure 3.18.

The diffusion coefficient is calculated by inserting the usual values for R and F, the measurement temperatures, the measured conductivities for these samples at these temperatures in reducing conditions, and V = 0.3 V due to the open circuit potential.

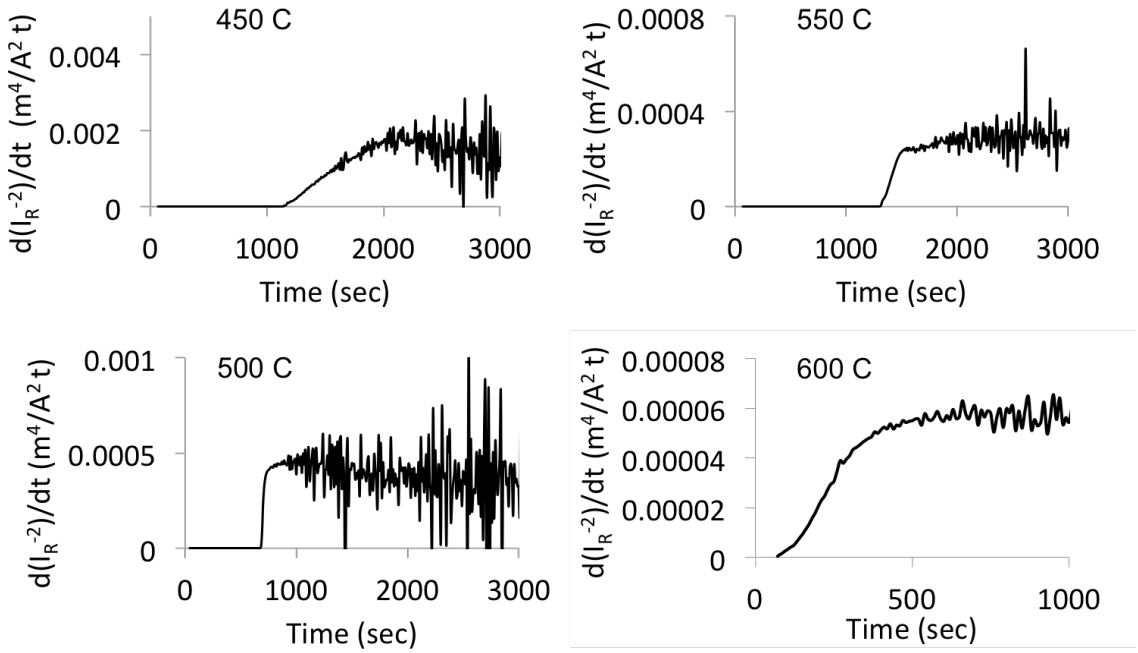

Figure 3.18. Plots of $d(I_R^{-2})/dt$ vs. time at various temperatures reveal that at longer times, this value becomes constant with time. The value for dI_R^{-2}/dt is extracted from these plots and inserted into equation (3.13).

To solve for the proton content, we simply rearrange equation (3.7) and insert the calculated diffusion coefficients.

(3.14) $n_1 = RTs_0/(D.F^2)$

The values obtained for D and n_1 are shown in Table 3.1. The diffusion coefficients are low compared to diffusion constants for other well-known proton conductors CsH_2PO_4 or the perovskites $BaCeO_3$ (10^{-10} – 10^{-8} m^2/sec). However, the conductivity of this system is far lower, so the low diffusion constants calculated here are reasonable for this system. The calculated values of D increase with increasing temperature as expected. As for the calculated proton concentrations, they are very low. The theoretical maximum H^+ concentration at 2% dopant content is 443 mol/m^3, and these calculated values are less than 1/4 of this. These calculated proton concentrations are fairly close to the proton concentration measured using NMR (*9*). The variation of the calculated proton content with temperature, while showing significant scatter, is consistently significantly below the maximum proton concentration that would result from complete dopant compensation by protons (440 mol/m^3). This would indicate that there is a significant concentration of undissociated pyrophosphate links in the Sr doped $CePO_4$ after exposure to H_2/H_2O atmospheres. It could also imply that the dopant concentration in the bulk is significantly lower than expected due to Sr segregation to the grain boundaries, as was discussed in Chapter 2.

Table 3.1.

Temp (C)	$d(I_R^{-2})/dt$ (m^4/A^2 t)	Conductivity (S/m)	D (m^2/sec)	n_1 (mol/m^3)
450	0.0017	0.000351	2.66E-12	85.1
500	0.00048	0.00103	6.87E-12	103.
550	0.00027	0.00379	5.61E-11	49.6
600	0.000056	0.0103	8.60E-11	90.6

3.3.4 Thermopower measurement

In order to gain further understanding of the electronic charge carrier in the $Ce_{0.98}Sr_{0.02}PO_4$ sample, it was important to carry out a measurement that would give us an idea of the band structure and sign of the charge carrier. The usual measurement used for this is the Hall effect; however, since the rare earth phosphate materials only conduct appreciably at high temperatures, carrying out this measurement was not possible. However, thermopower measurements can be carried out at elevated temperatures, and also yield the sign of the dominant charge carrier. Measurement of the Seebeck coefficient involves simply placing the sample in a controlled thermal gradient and measuring the potential that develops as a result. This measurement was successfully carried out on a Sr-doped sample, but attempts to measure an undoped sample were unsuccessful due to low conductivity.

The Seebeck coefficient for the $Ce_{0.98}Sr_{0.02}PO_4$ sample was found to be +230 μV/K in oxidizing conditions at every temperature between 300-500°C. The two important observations from this measurement are (1) that the sign of the coefficient is positive, and (2) that the coefficient is independent of temperature. The positive sign of the Seebeck coefficient indicates a positively charged carrier. This is consistent with the defect model: the mobile charge is proposed to be an electron-hole resulting from the change in valence state of the Ce cations. The treatment of the behavior of the Seebeck coefficient with temperature is complex and deserves a short discussion.

Expressions for the Seebeck coefficient (S = dV/dT) can be derived from the physical principles underlying thermoelectric phenomena. At open circuit, no charge carriers can flow out of the material, so this causes an accumulation of quasi-free carriers at the cold end of the sample. This produces a difference in electrochemical potential to counteract the flow. This potential difference is measured in the experiment. The sign of this potential depends on the sign of the charge building up at the cold end of the sample (*20*). The temperature dependence of the Seebeck coefficient must come from the dependence of the current density of a material on temperature.

For semiconducting materials, the density of carriers is strongly dependent on temperature since the Fermi energy level relative to the transport level and Fermi distribution change with temperature. For a broad-band semiconductor, S is given by

(3.15) $S = \pm (k/e)(E_F/kT + A)$

Where E_F is the Fermi energy measured relative to the transport level and A is a

dimensionless constant ~ 2-4 depending on the scattering mechanism (*21*).
In contrast, for materials in which the number of carriers is fixed, the current density becomes independent of temperature. The expression for S becomes (*20, 22*)

(3.16) $S = -(k/e)[\ln\beta(1-c)/c + ST/k]$

Where c is the concentration of carriers, ST is the vibrational entropy associated with the ions surrounding a polaron and β is a degeneracy factor. This expression is derived using the expression for electrical conductivity of a diffusion model. According to Heikes, equation (3.16) is comparable to equation (3.15) for the broad-band semiconductor in the limit that the effective mass of the carrier is so large that only one carrier is localized on a site. The Heikes formula is often used to determine the Seebeck coefficient in oxide thermoelectrics, which have highly correlated d electrons. (*23, 24*)

In the literature, the observation of a Seebeck coefficient that is temperature independent is often taken as an indicator that the charge carrier in the material behaves like a free particle. This supports the present treatment of the carriers as polarons that conduct via a diffusion mechanism (*21, 22, 25*).

The use of this equation (3.16) would give an estimate of the carrier concentration of the sample if reasonable values for the degeneracy factor β and the vibrational entropy ST could be determined. However, these values are unknown for this system. Further insights can be obtained from first-principles calculations of the electronic structure, and more comprehensive measurements of the Seebeck coefficient, varying the doping level, oxygen partial pressure, and temperature.

3.4 Conclusions

In this section, the identity of the dominant charge carrier has been probed using ac impedance, dc chronoamperometry, and thermopower measurements in various gaseous atmospheres. These experiments show that $La_{0.98}Sr_{0.02}PO_4$ is a dominant proton conductor under both oxidizing and reducing conditions, whereas $Ce_{0.98}Sr_{0.02}PO_4$ is a dominant electron-hole conductor under oxidizing conditions, and switches to proton conduction under reducing conditions. The qualitative shapes of the impedance responses can be used to identify the charge carriers. Thermopower measurements confirm the positive charge of the electronic carrier. The measurement of a constant Seebeck coefficient with temperature indicates a localized charge that likely is transported by a polaron-hopping mechanism. The transient currents of the samples were analyzed qualitatively and semi-quantitatively. Sharp changes in current upon oxidation and reduction indicate critical processes at work. The nature of these processes will be discussed in the next chapter. The transient is modeled using a layer growth model, and diffusion constants and proton concentrations are extracted. Diffusivities are on the order of 10^{-12} to 10^{-11} m^2/sec, which is low compared to other proton conductors. The proton concentrations calculated are on the order of 100 mol/m^3, well below the theoretical maximum value set by the dopant concentration. This calculated low carrier concentration is consistent with the measured

level (*9*), and indicates that an appreciable concentration of pyrophosphate defects remains intact.

Understanding the behavior of the charge carriers in the samples $La_{0.98}Sr_{0.02}PO_4$ and $Ce_{0.98}Sr_{0.02}PO_4$ can next be applied to understanding mixed conduction in the alloyed system, $La_{0.98-x}Ce_xSr_{0.02}PO_4$.

Chapter 4

Tunable Electronic Conduction in $La_{0.98-x}Ce_xSr_{0.02}PO_{4-\delta}$ Solid Solutions[1]

This work was previously published in *Electrochimica Acta* and is repeated here in its entirety with permission of all authors. There is some data and discussion in the experimental and microstructural characterization sections of this chapter that has already been presented in Chapters 2 and 3 of this thesis.

4.1 Abstract

This study examines the conductivity of the rare earth orthophosphate ceramic series $La_{0.98-x}Ce_xSr_{0.02}PO_{4-\delta}$ in oxidizing and reducing atmospheres. The full rare earth orthophosphate series is synthesized and characterized using XRD, SEM, TEM-EDX, and HRTEM to detect the presence of second phases and potential compositional heterogeneities that may affect conductivity. AC impedance measurements under reducing conditions showed that the protonic conductivity is nearly independent of the cerium content. Under oxidizing conditions the conductivity shows percolation-type dependence with increasing Ce content; this is attributed to the appearance of electron- holes, localized on Ce, as the dominant charge carrier. The fit of the experimentally measured conductivity with composition to a percolation model implies a low percolation threshold, which may result from Ce clustering or higher nearest neighbor hopping of the electron holes. The strong Ce concentration dependence of the conductivity suggests an increasing hole concentration with increasing cerium content, which in turn would imply a relatively high stability of the pyrophosphate defects.

4.2 Introduction

The conductivity of the rare earth orthophosphate system $La_{0.98-x}Ce_xSr_{0.02}PO_{4-\delta}$ is examined as a function of the Ce content in oxidizing and in reducing atmospheres. In reducing atmospheres (*i.e.* humidified hydrogen) Sr-doped $CePO_4$ exhibits a protonic conductivity that is similar to that of Sr-doped $LaPO_4$. However, in oxidizing conditions Sr-doped $CePO_4$ is an electron hole conductor with Arrhenius temperature dependence [1, 2]. This suggests that percolation behavior should be expected in this series for electron-hole hopping, since Sr-doped $LaPO_4$ is not an electronic conductor and cerium 3+ ions can host an electron hole. The monazite phosphate crystal structure accommodates the full range of La/Ce ratios, and thus should be a good model system for studying percolation behavior in single-phase solid solutions. The changes in material properties as a function of composition in

[1] This work was previously published in *Electrochimica Acta* as: H. L. Ray, N. Zhao, L. C. De Jonghe, "Hole Percolation and Proton Conduction in Monazite Solid Solutions: $La_{0.98-x}Ce_xSr_{0.02}PO_{4-\delta}$ *E. Acta.* DOI: 10.1016/j.electacta.2012.05.101 (2012).

mixed materials have been studied to a great extent [3-6], and scaling laws have been postulated for many material properties, including conductivity. However, most of the focus has been on conductor-insulator mixtures rather than mixtures of two conducting materials, and most of the studies have been theoretical in nature. In the present work, the conductivity as a function of Ce content of the $La_{0.98-x}Ce_xSr_{0.02}PO_{4-\delta}$ system is compared to the one expected on the basis of available percolation models.

It has been shown that doping $LaPO_4$ and $CePO_4$ with Sr introduces associated effective negative charges that enable the incorporation of positively charged defects such as hydrogen phosphate groups, pyrophosphate groups, and electron-holes. These defects compete with each other for dominance, and the dominant defect changes depending on the atmosphere. The interaction of $La_{0.98}Sr_{0.02}PO_{4-\delta}$ and $Ce_{0.98}Sr_{0.02}PO_{4-\delta}$ with humidified oxidizing and reducing atmospheres has been explored by several groups, especially those of Amezawa and Kitamura [1, 2, 7-15]. The general model describing the defect behavior of the rare earth orthophosphates $LnPO_4$ proposed by Kitamura et al. [1] is summarized below.

When $LaPO_4$ or $CePO_4$ is doped with Sr, a structural defect that has been observed to form is the pyrophosphate ion $P_2O_7^{4-}$ as, for example, in Equation (4.1). In this system, this pyrophosphate group takes the place of two PO_4^{3-} anions, has an effective positive charge, and is equivalent to an oxygen vacancy. In theory, this defect can then be exchanged for proton or electron-hole defects. However, the chemistry of these pyrophosphate defects, and their interactions with oxygen, hydrogen, and water are not fully quantified, so that uncertainty remains as to the actual concentrations of the various species. Equations 4.2-4.4 show the three proposed reactions that allow exchange between the three types of defects.

(4.1) $$2SrHPO_4 \xrightarrow{LaPO_4} (P_2O_7)^{\bullet\bullet}_{2PO_4} + 2Sr'_{La} + H_2O$$

(4.2) $$(P_2O_7)^{\bullet\bullet}_{2PO_4} + H_2O_{(g)} \leftrightarrow 2(HPO_4)^{\bullet}_{PO_4}$$

(4.3) $$\tfrac{1}{2}O_2 + 2(HPO_4)^{\bullet}_{PO_4} \leftrightarrow 2(PO_4)^{X}_{PO_4} + H_2O + 2h^{\bullet}$$

(4.4) $$(P_2O_7)^{\bullet\bullet}_{2PO_4} + \tfrac{1}{2}O_2 \leftrightarrow 2h^{\bullet} + 2(PO_4)^{X}_{PO_4}$$

where Sr'_{Ln} represents Sr^{2+} on the Ln sites (La^{3+} or Ce^{3+}), $(P_2O_7)^{\bullet\bullet}_{2PO_4}$ represents the pyrophosphate bond between two adjacent orthophosphate tetrahedra, $h^{\bullet}$ represents an electron-hole, and $(HPO_4)^{\bullet}_{PO_4}$ represents a protonated orthophosphate ion.

Equation (4.2) shows that when water vapor is present, pyrophosphate groups can be hydrated, with protons incorporating into the lattice as hydrogen phosphate groups, HPO_4^{2-}. These structures were observed by Amezawa [10]. Protons hydrogen-bond to oxygen, and move through the system by hopping from oxygen to oxygen aided by rotation of the

phosphate tetrahedra [16]. Equation (4.3) shows how a proton can be exchanged for an electron hole. Upon exposure to oxygen, water is evolved, and an electron-hole is introduced to preserve charge neutrality.

Equation (4.4) of the proposed defect model introduces oxygen and electron holes as compensation for a pyrophosphate defect. The hole charge carrier behaves very differently in $LaPO_4$ *vs.* $CePO_4$. A low amount of electronic conductivity has been reported in doped $LaPO_4$ at sufficiently high temperatures and low water partial pressures. The carriers were identified as p-type with the positive Seebeck coefficient measured by Amezawa *et al.* [9]. However, equation (4.4) would predict increasing electronic conduction with increasing oxygen partial pressures, while conductivity measurements of $LaPO_4$ in dry conditions show no pO_2 dependence [11]. In contrast, the electronic conductivity of $CePO_4$ in dry conditions is high, and does increase with pO_2. However, the dependence is lower than predicted by the defect model [2]. Conduction is thought to be polaronic in nature, with the hole localized on the Ce cation. It should be stated here that the formation or removal of pyrophosphate defects requires transport of oxygen ions, which in these materials can be a slow process. This could perhaps account for some of the discrepancies.

In the present work, the rare earth orthophosphates $La_{0.98-x}Ce_xSr_{0.02}PO_{4-\delta}$ are synthesized by a wet precipitation method. The microstructures of the samples are examined using XRD, SEM, TEM-EDX, and HRTEM. Next, the conductivity of the rare earth orthophosphate system $La_{0.98-x}Ce_xSr_{0.02}PO_{4-\delta}$ is determined by AC impedance measurements. Finally, the changes in conductivity with composition are discussed.

4.3. Experimental

4.3.1 Synthesis

To synthesize the $LaPO_4$ and $CePO_4$ powders, 2 molar aqueous solutions of $Ce(NO_3)_3{\cdot}6H_2O$ (Alfa Aesar) or $La(NO_3)_3{\cdot}6H_2O$ (Alfa Aesar) were added dropwise to a 2 molar aqueous solution of $NH_4H_2PO_4$ (Acros Organics) in a 1:1 metal to phosphorus ratio. The resulting precipitates (fine white solids) were collected using centrifugation, washed with water, filtered, and dried. The collected precipitates were the hydrated rhabdophane phase of the rare earth orthophosphate. The powders were heat treated at 800°C for 2 hours in order to transform them to the monoclinic monazite phase. The powders were ground with an agate mortar and pestle, and passed through a 325 mesh sieve. Next, the $La_{0.98-x}Ce_xSr_{0.02}PO_{4-\delta}$ compositions were prepared by attritor milling appropriate amounts of the $LaPO_4$, $CePO_4$, and $SrHPO_4$ (99.99% purity, Aldrich) powders in isopropyl alcohol. The molar Ce content, x, was varied from 0 to 0.98, increasing in steps of 0.1. The Sr-doping level was kept constant at 2 mol %. This level of doping was chosen because it is high enough to incorporate enough charge carriers to outweigh carriers introduced by intrinsic impurities, but low enough to avoid the appearance of second phases such as $Sr_3Ce(PO_4)_3$ [2]. The resulting powder mixtures were dried, pressed at 145 MPa into 13 mm diameter pellets, and sintered for 5 hours at 1450°C. Sintered pellets had densities ranging from 80-95%.

4.3.2 Microstructural Characterization

The densities of the pellets were calculated by measuring their dimensions and masses. The crystal structures of the rhabdophane and monoclinic phases were confirmed using a Philips PW3040 X'Pert Pro Diffractometer using a Cu Kα (α =1.54056Å) source operated with a 45keV X-ray tube voltage. The measured XRD patterns were matched to the JCPDS cards for rhabdophane $LaPO_4 \cdot nH_2O$ 04-0635, monoclinic $LaPO_4$ 32-0493, and monoclinic $CePO_4$ 32-0199. Peak widths were calculated by using X'Pert Highscore software. Lattice parameters of the series were calculated using Rietveld refinement using the PowderCell 2.3 software. The reference cell parameters used in the refinement for the $LaPO_4$ and $CePO_4$ compositions were taken from the study by Pepin [17]. The microstructures of the sintered pellets were studied by an analytical scanning electron microscope (SEM, Zeiss Gemini Ultra-55) operated at 5 kV, and a transmission electron microscope (TEM, JEOL 2100F) operated at 200 kV, both equipped with an energy dispersive X-ray spectroscope (EDS). The elemental distributions, determined by high angle annular dark-field (HAADF-STEM, also called Z-contrast) imaging and EDX composition analysis, were acquired on JEOL 2100F with an annular dark-field detector and Oxford INCA EDX microanalysis system. In the scanning mode (STEM mode) the 1.5 nm focused electron beam was stepped across the specimen for chemical analysis. The TEM samples were made from the planar sections of the sample, by mechanical pre-thinning (Gatan dimple grinder) and Ar-ion milling (in a Fischione system) with a liquid nitrogen cooling stage to minimize artifacts. HRTEM images were obtained using a 300-kV Philips CM300 transmission electron microscope.

4.3.3 Conductivity measurements

Platinum mesh electrodes were attached to the sintered pellets using platinum paste (Heraeus). Total conductivity measurements of the $La_{0.98-x}Ce_xSr_{0.02}PO_{4-\delta}$ series were taken in air bubbled through water at 25 or 35°C using the 2-probe AC impedance technique with a Bio-Logic SP-150/VSP/ VMP3 potentiostat. The frequency was varied from 0.1 Hz to 1 MHz, and the alternating applied potential amplitude was 25 mV. Impedances were measured between 350 and 600°C in ambient air for every member of the series. The impedances of selected samples were also measured in 3% humidified H_2 gas. All impedance data were fitted to the usual equivalent circuits [18], including constant phase elements [19], for conducting ceramics using the Levenberg-Marquardt algorithm in the software package EC-Lab (BioLogic). This equivalent circuit consists of separate responses from bulk, grain boundary, and electrode processes. The high frequency arc in the impedance plots was assigned to the bulk grains, the lower frequency arc was assigned to the grain boundary, and additional responses at very low frequency were attributed to electrode processes [18]. Not all arcs were evident in the measured frequency range under all conditions. For example, the bulk resistance for conduction in $Ce_{0.98}Sr_{0.02}PO_{4-\delta}$ and other Ce-rich compositions in air were apparent in the measured frequency range for temperatures below 350°C, but moved out to much higher frequencies at higher temperatures. In these cases, the bulk response was estimated by measuring the high frequency intercept of the grain boundary response. For very resistive samples, especially

those containing high fractions of La and measured at lower temperatures, the response at low frequencies became too noisy to interpret.

4.4. Results and Discussion

4.4.1 Microstructural Characterization

4.4.1.1 X-ray Diffraction

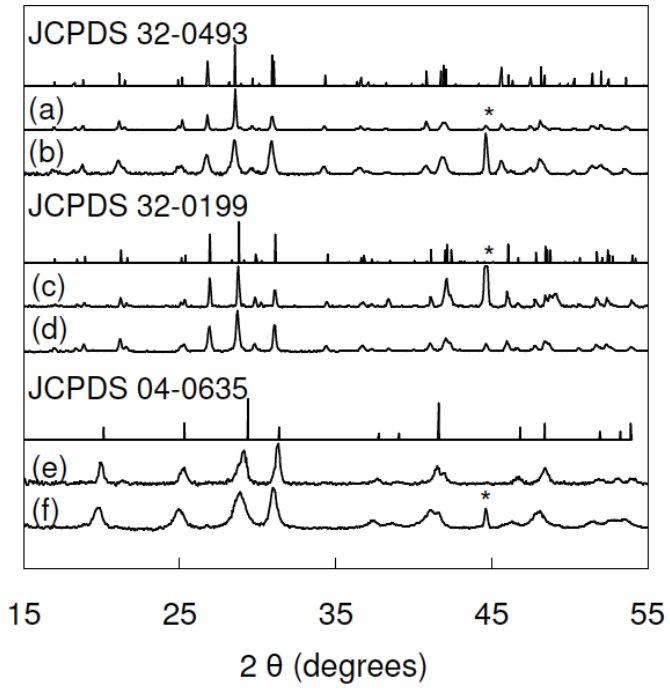

Figure 4.1. Measured XRD spectra of (a) the monazite $La_{0.98}Sr_{0.02}PO_{4-\delta}$ pellet and (b) the $LaPO_4$ powder, (c) the monazite $Ce_{0.98}Sr_{0.02}PO_{4-\delta}$ pellet and (d) the $CePO_4$ powder, and the as-precipitated rhabdophane powders of (e) $CePO_4$ and (f) $LaPO_4$. The powders are single-phase, and peak widths decrease after heat treatments, indicating grain growth. The JCPDS patterns are shown for comparison. The asterisks at 2θ = 44° indicate the reflection from the iron in the sample holder.

X-ray diffraction was used to confirm the crystal structure and phase purity of the series. As shown in Figure 4.1, the as-precipitated $LaPO_4$ and $CePO_4$ powders matched JCPDS card 04-0635, which is the hexagonal hydrated rhabdophane structure. After heat treatment at 800°C, the powders changed phase to monoclinic monazite. The $LaPO_4$ powder matched JCPDS card 32-0493, and the $CePO_4$ powder matched JCPDS card 32-0199. After mixing with $SrHPO_4$ and sintering at 1450°C, the x-ray spectra showed no extra crystalline phases. The extra peaks at 2θ=44° are marked with an asterisk, and they correspond to iron from the XRD sample holder. Peak widths decreased after sintering the powders, indicating an increase in grain size. As depicted in Figure 4.2, when the $LaPO_4$ and $CePO_4$ powders were mixed together and sintered, the XRD peaks shifted as a function of composition. The difference between the two materials is slight; the cell volume for $LaPO_4$ is 2% smaller than

that for $CePO_4$, which translates to about a 0.3 degree difference in peak shifts. The lattice parameters for each composition were calculated with Rietveld refinement using the PowderCell 2.3 software, with reference cell parameters for $LaPO_4$ and $CePO_4$ taken from Pepin [17]. The lattice parameters were found to vary with Ce content according to Vegard's law, deviating from the predicted value by less than 1%. This is also consistent with XRD studies on the (La,Ce)PO_4 system carried out by DeBiasi [20].

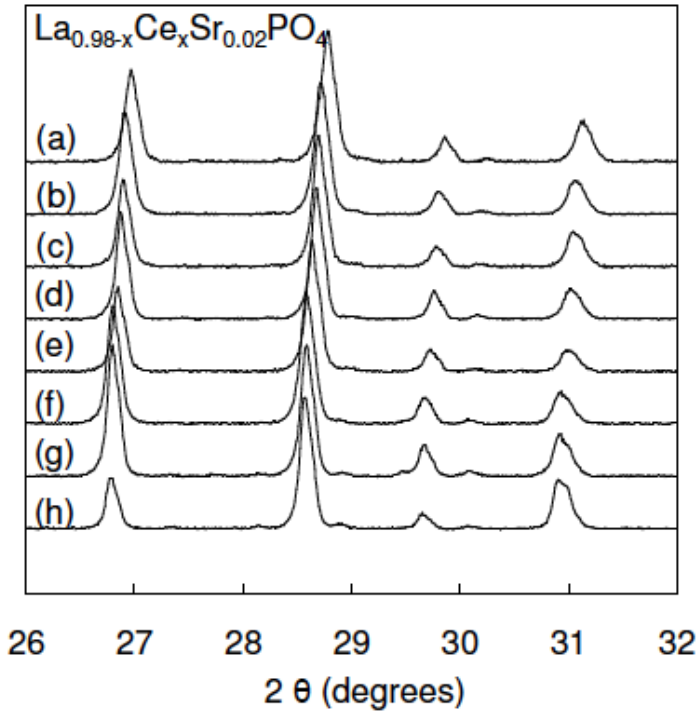

Figure 4.2. XRD spectra of selected samples from the $La_{0.98-x}Ce_xSr_{0.02}PO_{4-\delta}$ series. (a) x=0.98 (b) x=0.94 (c) x=0.69 (d) x=0.49 (e) x=0.29 (f) x=0.14 (g) x=0.04 (h) x=0. Peaks shift according to Vegard's law as a function of composition.

4.4.1.2 Scanning Electron Microscopy (SEM)

Figure 4.3 shows SEM images of the microstructures of a 93% dense $Ce_{0.98}Sr_{0.02}PO_{4-\delta}$ pellet and an 81% dense $La_{0.98}Sr_{0.02}PO_{4-\delta}$ pellet. Figure 4.3 (a) and (c) are images of the surfaces of the pellets. They show that the grains are equiaxed and between 0.5-4 μm in size. Figure 4.3 (b), an image of a fracture surface of $Ce_{0.98}Sr_{0.02}PO_{4-\delta}$, shows that the sample is nearly fully dense. Figure 4.3 (d) shows a fracture surface of the $La_{0.98}Sr_{0.02}PO_{4-\delta}$ sample with some evident porosity. The lower density is consistent with the literature [11] on the monazite composition: $LaPO_4$ is known to require a higher sintering temperature than $CePO_4$ [21]. In this work, all reported conductivities are corrected for density by dividing the measured conductivity by the measured density of the respective pellet.

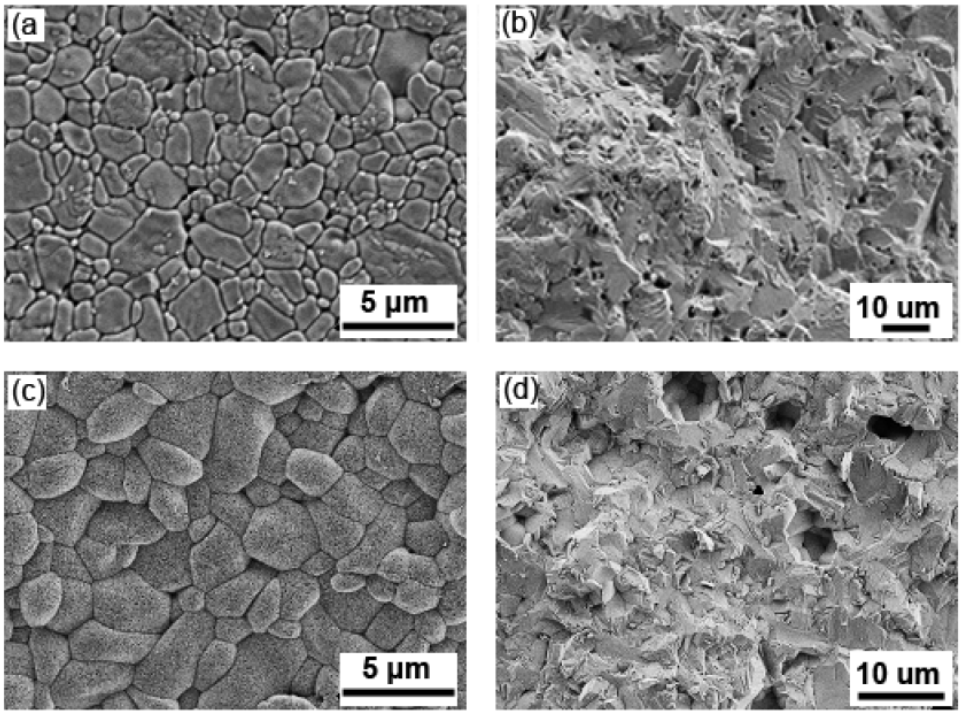

Figure 4.3. SEM images of the microstructures of pressed and sintered ceramic pellets. (a) Surface of the $Ce_{0.98}Sr_{0.02}PO_{4-\delta}$ pellet. (b) Fracture surface of the $Ce_{0.98}Sr_{0.02}PO_{4-\delta}$ pellet. (c) Surface of the $La_{0.98}Sr_{0.02}PO_{4-\delta}$ pellet (d) Fracture surface of the $La_{0.98}Sr_{0.02}PO_{4-\delta}$ pellet.

4.4.1.3 High Resolution Transmission Electron Microscopy (HR-TEM)

A sintered ceramic sample of composition $La_{0.39}Ce_{0.59}Sr_{0.02}PO_{4-\delta}$ was examined using TEM, revealing the presence of 3-5 nm thick amorphous grain boundary phases, Figure 4.4 (a). Some triple junctions also contain amorphous material, as shown in Figure 4.4 (b). Amorphous grain boundary phases in sintered $LaPO_4$ have been observed before [15]. The appearance of these phases has been attributed to residual hydrogen–phosphate-type compounds remaining from the aqueous precipitation synthesis technique [21, 22]. The total conductivity of the samples can be affected by the presence of the grain boundary phases; however, the AC impedance technique allows separation of the grain bulk and the grain boundary contributions to the conductivity.

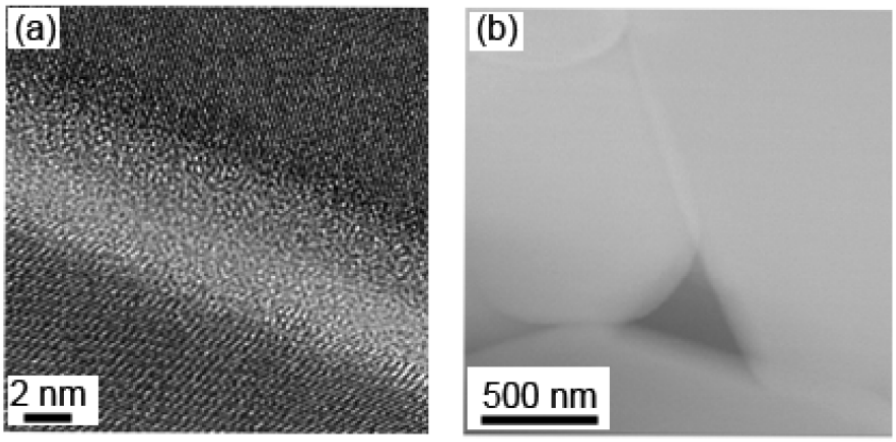

Figure 4.4. (a) HR-TEM image of a sintered pellet with composition $La_{0.39}Ce_{0.59}Sr_{0.02}PO_{4-\delta}$. An amorphous film about 4 nm thick is present at the grain boundary. (b) TEM image of a junction between 3 grains of the same sample. The junction contains a large pocket of amorphous phase.

4.4.1.4 Energy Dispersive Spectroscopy (TEM-EDX) and elemental mapping

TEM-EDX measurements and elemental mapping were used to examine the chemical composition of the $La_{0.39}Ce_{0.59}Sr_{0.02}PO_{4-\delta}$ sample with spatial resolution. The compositions of the bulk grains were measured at 54 random, 1.5 nm diameter spots. The concentration of each element was measured at the various spots. The standard deviations of the local concentration measurements of La, Ce, and P for this sample were compared. The deviations for Ce and La content were 13% and 10% of the mean local concentration. This was comparable to the value of 11% for P, for which local variations should be absent. These results indicate that the scatter in the measured local concentrations originate in the EDX system, masking more subtle sample heterogeneity. The amount of material probed by the 1.5 nm diameter probe in the approximately 100 nm thick sample is about 175 nm^3, while the unit cell volume is about 0.3 nm^3. With 2 rare earth (RE) atoms per unit cell, the analytical beam captures about 1200 RE atoms. On the basis of these results, meaningful variations in the local Ce/La ratios on a scale larger that the probed volumes may be excluded; however, Ce clustering on a smaller scale cannot be eliminated.

Variations in the local Sr content were found to be more readily detected, as seen in the frequency distribution in Figure 4.5. Significant accumulation of Sr in grain boundaries and grain junctions is evident in Figure 4.5, and also shown in the elemental map, Figure 4.6. This Sr-enrichment of the grain boundary phase lowers the average Sr doping level of the bulk grains from the nominal 2 mol % to about 1.5%. However, it is postulated that these variations do not play a large role in the hole conductivity. The identity of the dominant charge carrier and the mechanism of transport in the bulk material are not expected to change due to the Sr distribution. This assertion is in part supported by recent results of DFT computations that show the electron hole to be highly localized on the cerium ion (i.e. Ce^{4+}) with some evidence of slight hybridization of the Ce 4f-O2p orbitals, as was proposed by Takahashi et al. [23] for hole conduction in La-Ce borate solid solutions.

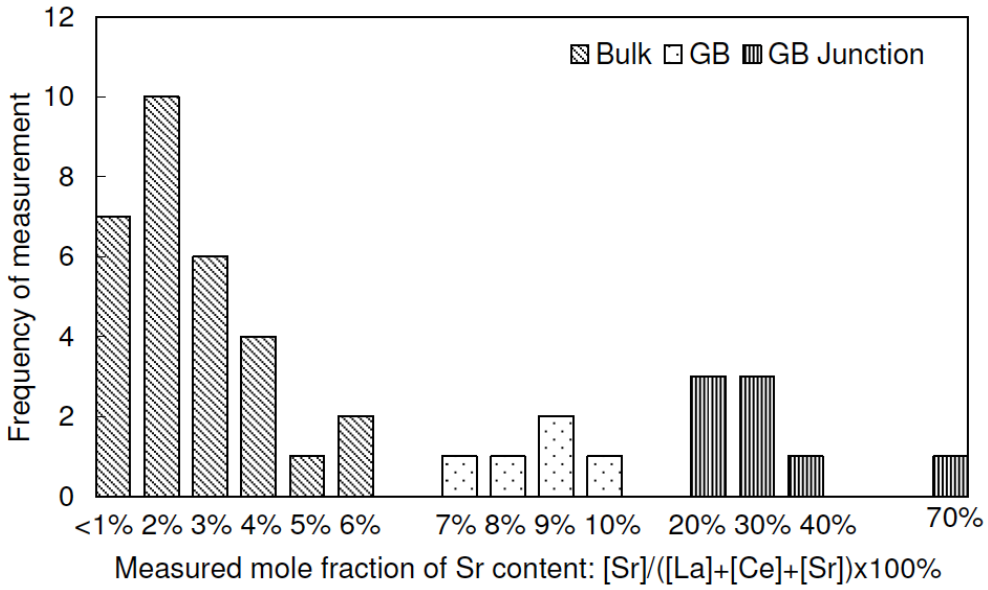

Figure 4.5. Frequency distribution plot of the measured composition of $La_{0.39}Ce_{0.59}Sr_{0.02}PO_{4-\delta}$. The amount of Sr, La, and Ce measured using TEM-EDX in 43 different 1.5 nm spots were tabulated and the fraction of element concentrations [Sr]/([La]+[Ce]+[Sr]) was calculated for each spot. The compositions of spots located in bulk, grain boundary (GB), and GB junction areas are compared: Sr seems to segregate to the grain boundaries and junctions.

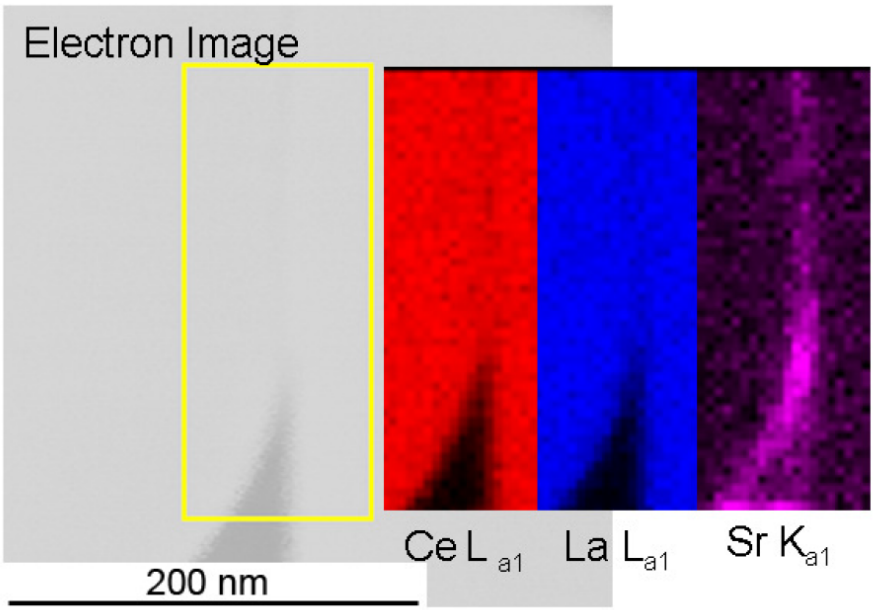

Figure 4.6. Elemental mapping of the La, Ce, and Sr in the bulk and the grain boundary of a $La_{0.39}Ce_{0.59}Sr_{0.02}PO_{4-\delta}$ sample. The electron image shows the intersection of two bulk grains (lighter grey) and a pocket of amorphous grain boundary phase (darker grey). The elemental maps of Ce and La show that those elements are concentrated in the bulk grains, while the grain boundary does not contain detectable amounts of them. In contrast, the elemental map of Sr shows that the grain boundary phase is rich in Sr.

4.4.2 Conductivity Measurements

4.4.2.1 Interpretation of the AC impedance spectra for the series $La_{0.98-x}Ce_xSr_{0.02}PO_{4-\delta}$

To extract the bulk conductivities from the ac impedance spectra of the $La_{0.98-x}Ce_xSr_{0.02}PO_{4-\delta}$ materials, careful interpretation considering mixed ionic and electronic conduction was required. In mixed ionic and electronic conductors (MIECs), both resistive and capacitive elements of the impedance from both types of charge carrier can contribute to each of the bulk, grain boundary, and electrode responses. Figure 4.7(a) shows the equivalent circuit for a mixed electronic and ionic conductor [18]. Since the impedance of a capacitive element scales with the reciprocal of frequency, at high frequencies, highly capacitive elements can be bypassed, and only the resistive component observed. At very low frequencies, large capacitances can dominate over resistive elements. Ionic carriers tend to give rise to higher capacitances and resistances than electronic carriers. Since ionic and electronic circuit elements occur in parallel for each phase, combinations of ionic capacitances and electronic resistances may be observed in certain phases. These effects are shown in the shapes of the Nyquist plots.

In the $La_{0.98-x}Ce_xSr_{0.02}PO_{4-\delta}$ materials, the shape of the Nyquist plot changed upon exposure to different gases, as well as with changes in temperature and composition. Representative Nyquist plots are shown in Figures 4.7(b-d).
Figure 4.7(b) shows the Nyquist plot for $Ce_{0.98}Sr_{0.02}PO_{4-\delta}$ at 350ºC in 3% humidified hydrogen, in which protonic conductivity is known to dominate. This type of Nyquist plot is representative of the plots observed for the entire $La_{0.98-x}Ce_xSr_{0.02}PO_{4-\delta}$ series in reducing conditions, as well as for compositions with $x<0.05$ in air. The single, broad arc shown in this plot can be fitted using the standard equivalent circuit for an ion conductor with the parameters shown in Table 4.1. It should be noted that the bulk response occurs at high frequency and has a capacitance on the order of 10^{-10} F, whereas the grain boundary response occurs at lower frequency and has capacitance of 10^{-9} F.

Figure 4.7(c) shows the Nyquist plot for $Ce_{0.98}Sr_{0.02}PO_{4-\delta}$ at 350ºC in air. For this material in air, the dominant charge carrier should be electronic. Two separate dispersions are visible here: a small arc at high frequency with capacitance $3x10^{-10}$ F, and a larger one at lower frequency with capacitance $6x10^{-9}$ F. These measured capacitances are the same as those measured for proton conduction, thus the small arc is assigned to bulk impedance, and the larger one to grain boundary impedance. The small bulk response is shown in the inset; this arc was fitted using the EC-lab software to obtain bulk conductivity values. The electrode response (usually a capacitive Warburg element) is not visible in this plot. One way to explain this is that it may have been bypassed by low resistance impedance.

Figure 4.7(d) shows the Nyquist plot for $La_{0.69}Ce_{0.29}Sr_{0.02}PO_{4-\delta}$ in air. It is representative of the line shapes seen in air for intermediate composition samples. There are three dispersions visible: a small one at high frequency, a large one at lower frequency, and at very low frequency a response attributed to electrode processes. Again, the measured capacitances fall in the 10^{-10}, 10^{-9}, and 10^{-6} F ranges, consistent with responses from the

bulk, grain boundary, and electrodes. Shown in the inset is the response from the bulk that was fitted in order to obtain bulk conductivity values.

For the responses shown in Fig. 4.7(c) and (d), it must be noted that as the temperature increased above 400ºC, the capacitive element of the high frequency response was shorted so that an arc was no longer visible. The bulk electronic impedance was then approximated as a resistor, and was estimated by taking the high frequency intercept of the grain boundary arcs (the offset of the low frequency arc away from the 0 point of the complex impedance plot).

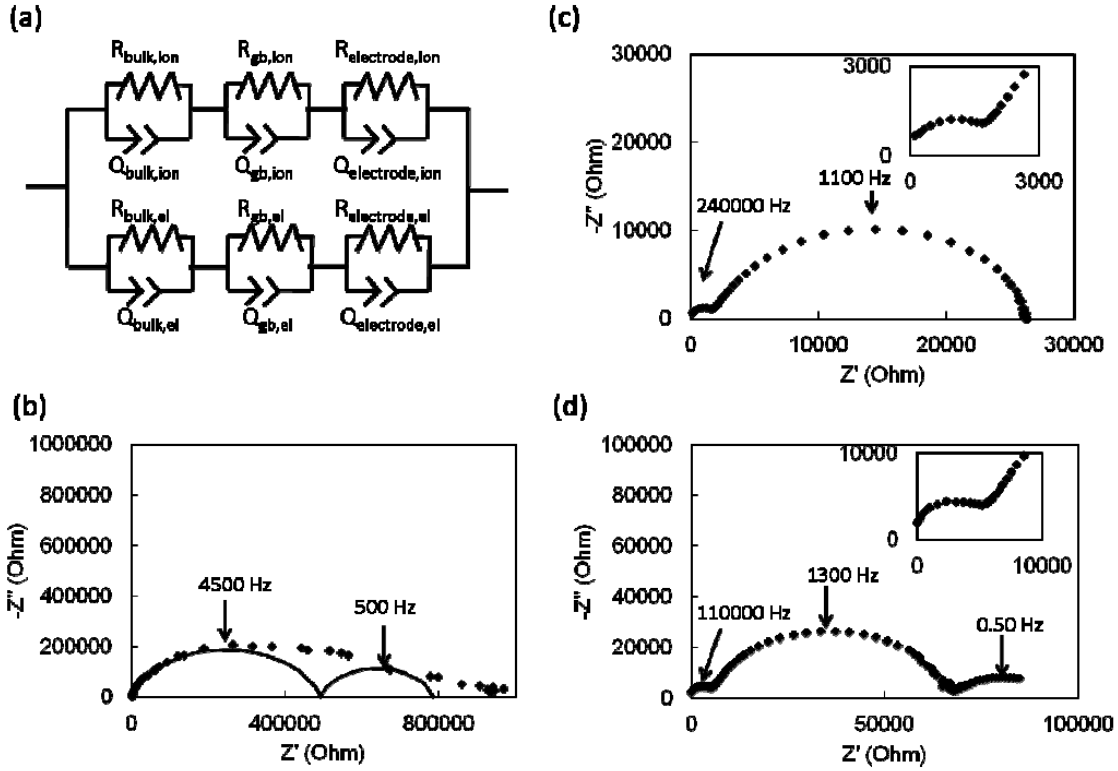

Figure 4.7 (a) Standard equivalent circuit for a mixed ionic and electronic conductor, showing parallel resistors (R) and pseudocapacitors (Q) for the bulk, grain boundary (gb), and electrode responses for both ionic (ion) and electronic (el) charge carriers. (b) Representative Nyquist plot for AC impedance measurements taken at 350°C in 3% humidified hydrogen gas for the full series $La_{0.98-x}Ce_xSr_{0.02}PO_{4-\delta}$. This line shape was similar for compositions measured in air with x <0.050. The shape of the plot is standard for a pure ionic conductor. The bulk and grain boundary responses fitted using the ionic equivalent circuit are also shown. (c) Nyquist plot for $Ce_{0.98}Sr_{0.02}PO_{4-\delta}$ measured in 3% humidified air at 350°C. Inset is shown the high frequency response from the bulk. (d) Nyquist plot for the composition $La_{0.69}Ce_{0.29}Sr_{0.02}PO_{4-\delta}$ measured in 3% humidified air at 350°C. Three separate responses from bulk, grain boundary, and electrode are visible. The inset shows the high frequency response from the bulk.

Table 4.1
The equivalent circuit for an ion conductor can be fitted to the Nyquist plot given in Fig. 4.7(b) using the parameters listed here. Q refers to the pseudocapacitance; a is the constant phase element; and R is the resistance. 1 refers to the bulk response, and 2 refers to the grain boundary response.

Circuit element	Value
Q1	4.8×10^{-10} F
a1	0.83
R1	490,000 ohm
Q2	4.6×10^{-9} F
a2	0.83
R2	290,000 ohm

4.4.2.2 Bulk Conductivities of $La_{0.98}Sr_{0.02}PO_{4-\delta}$ and $Ce_{0.98}Sr_{0.02}PO_{4-\delta}$

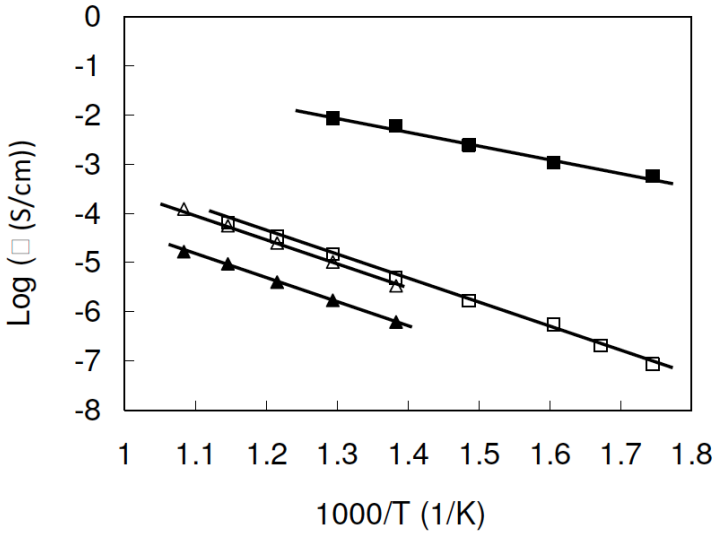

Figure 4.8. Bulk conductivity of the two end members of the series, $Ce_{0.98}Sr_{0.02}PO_{4-\delta}$ (squares) and $La_{0.98}Sr_{0.02}PO_{4-\delta}$ (triangles) measured in both ambient air (filled symbols) and 3% humidified hydrogen gas (empty symbols). Partial pressures of oxygen and water in air are pO_2 = 21 kPa, pH_2O = 4.2 kPa. Partial pressures of hydrogen and water in the reducing conditions are pH_2 = 101 kPa, pH_2O = 4.2 kPa.

The bulk conductivities of the $La_{0.98}Sr_{0.02}PO_{4-\delta}$ and $Ce_{0.98}Sr_{0.02}PO_{4-\delta}$ samples in oxidizing and reducing conditions are shown in Figure 4.8. Both samples display Arrhenius behavior under all atmosphere conditions. The bulk conductivity of $Ce_{0.98}Sr_{0.02}PO_{4-\delta}$ under oxidizing conditions shows an activation energy of 0.60 eV. In comparison, the conductivities of $Ce_{0.98}Sr_{0.02}PO_{4-\delta}$ and $La_{0.98}Sr_{0.02}PO_{4-\delta}$ in humidified H_2 are both about two orders of magnitude lower than this, with an activation energy of about 1.01 eV. The conductivity of $La_{0.98}Sr_{0.02}PO_{4-\delta}$ in air is about one order of magnitude lower, 1.02 eV. The latter would indicate that the majority of protons are removed in oxidizing atmosphere for the doped lanthanum phosphates. These measured values for the conductivities and activation energies are consistent with the values reported in the literature, taking into account the oxygen, hydrogen, and water partial pressures used. The activation energy for proton conduction in these materials has been reported in the literature to be 0.88-1.0 eV [1, 15, 16]. Conduction processes with lower activation energies (0.45-0.70) have been attributed to electronic conduction [1, 2], although activation energies alone are not carrier-specific.

4.4.2.3 Bulk Conductivity of the series $La_{0.98-x}Ce_xSr_{0.02}PO_{4-\delta}$

The qualitative shapes of the Nyquist plots of the series $La_{0.98-x}Ce_xSr_{0.02}PO_{4-\delta}$ were fitted using the appropriate equivalent circuits. In reducing conditions, and in air for x<0.05, all plots were fitted using only the ionic branch of equivalent circuit in Figure 4.7(a). However, for compositions measured in air with x>0.05, the bulk, grain boundary, and electrode arcs were all visible, and the plots were fitted with consideration of the full equivalent circuit for a mixed conductor.

The bulk conductivity of the series $La_{0.98-x}Ce_xSr_{0.02}PO_{4-\delta}$ in various atmospheres is plotted as a function of x, the Ce content, in Figure 4.9. In reducing conditions, the bulk conductivities for the La-Ce phosphate series are similar over the entire range, as is evident from Figure 4.9, and therefore it is reasonable to assume that the proton conductivity dominates, with similar transport mechanisms in reducing atmospheres for the entire series. Dominant proton conductivity in reducing atmospheres has been well established for $La_{0.98}Sr_{0.02}PO_{4-\delta}$ [1]. In oxidizing conditions, the conductivity of $La_{0.98-x}Ce_xSr_{0.02}PO_{4-\delta}$ varies strongly and non-linearly with x, as seen in Figure 4.9. Also pictured in the figure are the results of the conductivity measurements for selected compositions as a function of humidity in air. For these measurements, the relative humidity of the air was increased from 3% to 6% when measuring a sample. It was observed that the bulk conductivity of compositions for which $x \leq 0.05$ increased by about a factor of 2 with this change in humidity, whereas compositions with $x > 0.05$ showed no bulk conductivity change with increased p_{H2O}. This indicates that proton conduction is dominant below x<0.1, but that a different type of charge carrier is dominant above this level. Finally, the initial drop in conductivity for x<0.05 is expected, since $Ce^{(4+)\bullet}$ competes with $H^{\bullet}$ for charge compensation of the Sr'_{La}, resulting in a proton concentration decrease. At the same time, for x<0.05 the hole conductivity remains very low since the Ce concentration is near or below the percolation threshold discussed below.

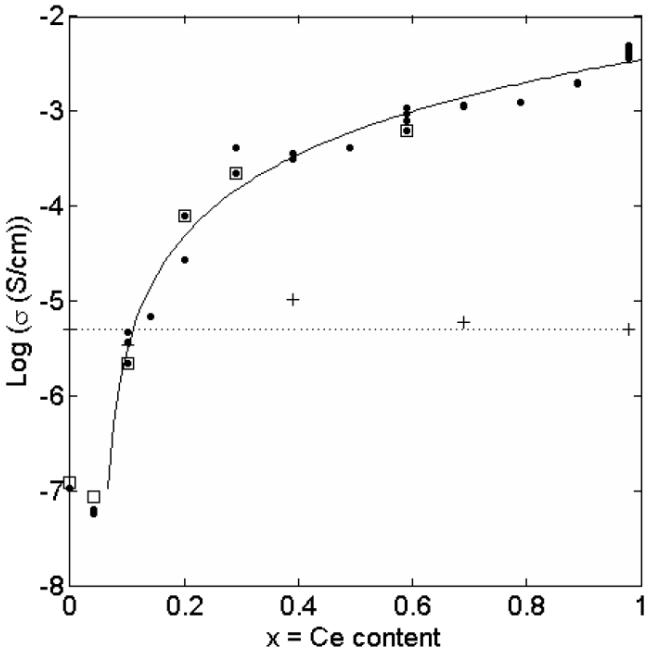

Figure 4.9. Log conductivity *vs.* x = Ce content for the $La_{0.98-x}Ce_xSr_{0.02}PO_{4-\delta}$ series in 3% humidified air (filled circles), 6% humidified air (empty squares), and in 3% humidified hydrogen (crosses). The percolation fit line for the conductivity in 3% humidified air is calculated using the equation in the text. The fit line for the conductivity in humidified hydrogen guides the eye.

4.4.3 Percolation Model

The nonlinear trend for the conductivity of the $La_{0.98-x}Ce_xSr_{0.02}PO_{4-\delta}$ series in air vs. x can be interpreted using a percolation model with p-type conduction occurring via a simple small-polaron hopping mechanism over the Ce^{3+} sites. The equations to describe this type of behavior have been derived by Efros and Shklovskii [5]. The model is constructed according to the following assumptions. The monazite series is described as a perfect solid solution: the crystal is viewed as a mixture of La^{3+}, Ce^{3+}, Ce^{4+}, and Sr^{2+} ions distributed perfectly randomly over the cation lattice sites of the monazite crystal. The La^{3+} and Sr^{2+} cations are treated as equivalent, null sites, and the charge carriers (Ce^{4+} sites) are considered dilute and noninteracting. The active Ce^{3+} cations are considered to be randomly distributed across the lattice. If a group of Ce^{3+} cations occupy nearest-neighbor sites, then they form a cluster. Polarons can hop among Ce^{3+} sites within a cluster, but they cannot hop between clusters that are not nearest neighbors. At low mole fractions of Ce, there are many small clusters, but no clusters that can span the width of the pellet between the two electrodes. The measured conductivity is low, since there is no continuous path for the polarons to travel. Under these conditions, the protonic carriers are more mobile, and they dominate the impedance response rather than the polarons. As the mole fraction of Ce in the lattice increases, the size and distribution of these clusters changes, and statistically the formation of larger and larger clusters becomes more probable. At a critical concentration, or the percolation threshold where $x = p_c$, a cluster large enough to reach all the way across the sample forms in the lattice. Polarons can hop through the spanning

cluster. Above this threshold, increasing the amount of Ce in the composite increases the density of the spanning cluster, thus increasing the conductivity.

We estimate in this work that the percolation threshold p_c falls in the range 0.050<x<0.10. This estimate for p_c is supported both by noting the composition at which the effects of water partial pressure cease to affect the bulk conductivity, and by the appearance of a high frequency dispersive arc in the Nyquist plots as in Fig 4.7(c). If the percolation model of the monazite lattice is applicable, then the conductivity of the composites should change according to the power scaling laws given by percolation theory. Using equations given by Efros and Shklovskii for the conductivity of a mixture of materials with finite conductivities [5], the conductivity *σ(x)* should obey the following trends.

(4.5) $\sigma(x) = \sigma_l (p_c - x)^s$ for $x<p_c$

(4.6) $\sigma(x) = \sigma_h (\sigma_l / \sigma_h)^u$ for $x=p_c$

(4.7) $\sigma(x) = \sigma_h (x - p_c)^t$ for $x>p_c$

where x is the mole fraction of Ce, p_c is the percolation threshold, σ_h is the conductivity of the composition $Ce_{0.98}Sr_{0.02}PO_{4-\delta}$, σ_l is the conductivity of the composition $La_{0.98}Sr_{0.02}PO_{4-\delta}$, and *s*, *t*, and *u* are the scaling exponents for conductivity. Conductivity scatter and limited data did not allow a reliable fit for $x<p_c$ using Eqn (4.5). Eqn (4.6) for fitting the conductivity at $x=p_c$ was not useful for determining p_c since its magnitude can be fit to any threshold by varying the exponent *u*. However, Eqn (4.7) could be used to fit the data for $x>p_c$. Three parameters could be varied: the percolation threshold p_c, the scaling exponent *t*, and the pre-exponential term σ_h. For simple 3D lattices with nearest neighbor jumps only, theoretical percolation models give site fraction thresholds ranging from 0.2 to 0.3, with values of the exponent t in Eqn (4.7) between 1.7 and 2.0.

The best fit of Eqn (4.7) to the measured data gives σ_h=0.00464, p_c=0.0572, and *t*=2.266, with the R^2, the coefficient of determination equal to 0.971. The pre-exponential term σ_h obtained from the fit is consistent with the measured conductivity of the composition with *x*=0.98. The scaling exponent is higher, and the percolation threshold lower than expected from theoretical models [3-5].

The scaling exponent *t*=2.266 found by the fit falls outside the range of values (1.7-2) given by percolation models. Several sources for the departure from the expected percolation exponents may be invoked. One possibility is that the special heterogeneities significantly affect the concentration dependence of the total conductivity. It is difficult, however, to propose systematic variations of conductivities based on heterogeneities. One more likely possibility is that the increased exponent is related to a defect chemistry that yields an increasing hole concentration with increasing cerium phosphate content. The fact that the pO_2 dependencies of the conductivities of $LaPO_4$ *vs.* $CePO_4$ measured by Amezawa [11] and Moral [2] are different implies that the values of the defect equilibrium constants for Eqns (4.3) and (4.4) controlling the hole content of the two materials are different. Though these

equilibrium constants are not known quantitatively, the fact that there is a difference indicates that in this $La_{0.98-x}Ce_xSr_{0.02}PO_{4-\delta}$ series, the hole concentration could increase with Ce content. This model would require a reconsideration of the defect chemistry in which the pyrophosphate defects more stable than presumed so far, and thus are progressively compensated by electron holes with increasing cerium content, rather than saturating at cerium concentrations equal to the Sr doping level. The persistence of pyrophosphate at high cerium concentration, as found, *e.g.*, by Raman spectroscopy by Amezawa [10] would suggest that such may be the case.

A striking result from fitting the percolation model to the data is that p_c, the experimental threshold for onset of percolation events, falls well below that for nearest neighbor percolation. Such a low threshold as seen here could have one of two causes: clustering of Ce, or non-nearest neighbor electron–hole jumps. Although measurements of the spatial Ce distribution did not detect meaningful local compositional variations at a scale larger than about 1000 Ce atoms, smaller clusters cannot be excluded and these can significantly depress p_c. Harter *et al.* calculated a percolation threshold of 0.126 for simple cubic systems with short-length correlation [24]. Duckers calculated that for a simple cubic system, the percolation threshold depended on a parameter that controlled the randomness of site occupation. He found that for "moderate attractive interparticle potentials, the percolation threshold decreased" [25] At the same time, higher nearest neighbor (nn or nnn) jumps can also strongly lower p_c, as was reported recently by Kurzawski *et al.* [26]. The present experiments cannot distinguish between these two possibilities, although we consider the clustering argument more likely in view of the rather large Ce-Ce distances involved in next nearest neighbor jumps.

4.5 Conclusions

The conductivity of the rare earth orthophosphate ceramic series $La_{0.98-x}Ce_xSr_{0.02}PO_{4-\delta}$ in oxidizing and reducing atmospheres were examined. The full rare earth orthophosphate series was characterized using XRD, SEM, TEM-EDX, and HRTEM, to detect the presence of second phases and potential compositional heterogeneities that may affect conductivity. AC impedance measurements under reducing conditions showed that the protonic conductivity is nearly independent of the Ce content. Under oxidizing conditions the conductivity showed a percolation-type dependence with increasing Ce content; this is attributed to the appearance of electron-holes, localized on Ce ions, as the dominant charge carrier. The fit of the experimentally measured conductivities to a percolation model implies a low percolation threshold and a persistent Ce concentration dependence. The low threshold most likely resulted from Ce clustering; however, higher nearest neighbor hopping of the electron holes could not be excluded. The strong Ce concentration dependence of the conductivity suggests an increasing hole concentration with increasing cerium content, which in turn would imply a relatively high stability of the pyrophosphate defects.

4.6 Acknowledgements

This work was supported by the Director, Office of Science, Office of Basic Energy Sciences, Materials Science and Engineering Division, of the U.S. Department of Energy under Contract No. DE-AC02-05CH11231. H. L. Ray would like to acknowledge the National Defense Science and Engineering Graduate Fellowship provided by the American Society for Engineering Education. The authors acknowledge support and use of the Ultra-55 SEM facility and Analytical FETEM JEOL 2100F at the Molecular Foundry at Lawrence Berkeley National Laboratory. The TEM samples were prepared using the facilities at the National Center for Electron Microscopy at LBNL. Phil N. Ross and Nicole Adelstein are thanked for useful conversations.

Chapter 5

Mixed Electronic and Protonic Conduction: DC current-voltage measurements of the $La_{0.98-x}Ce_xSr_{0.02}PO_4$ series in the fuel cell configuration

5.1 Introduction

The final question to be addressed in this work is: How do the charge carriers interact in a mixed ionic and electronic conductor? Do they move independently of each other, or can they modify each other's behavior?

The (La,Ce) orthophosphates are an ideal model system to investigate this because, as established in Chapter 4, we can tune the electronic contribution to the conduction by changing the composition. This is possible because all of the isostructural (La,Ce)PO_4 materials incorporate ionic defects in the same way, but the varied Ce content controls the electronic conductivity. Increasing the Ce content increases the number of sites the electronic carriers can occupy. Above the percolation threshold of about 5 mol % Ce, there is a connected network of Ce hosting sites throughout the sample, which becomes more densely populated as the Ce content increases, thus increasing the conductivity (*1*).

This is distinctive to the (La,Ce)PO_4 materials. In most oxide mixed conductors, the electronic current is changed either through aliovalent doping, which changes the total charge carrier concentration, or through manipulation of the gaseous atmosphere. That is, the oxygen partial pressure must be manipulated so that the material enters the mixed conducting regime, as is often mapped in a Brouwer diagram in which the defect concentrations are typically plotted as a function of oxygen partial pressure (*2*). Changing the Ce content of the (La,Ce)PO_4 materials allows us to increase electronic conductivity without changing the gaseous atmospheres or the aliovalent doping level.

As discussed in Chapter 3, the standard techniques (thermogravimetry, Hebb-Wagner polarization, small-gradient transference numbers) used to determine relative conductivities of ions and electrons are not appropriate for the (La,Ce)PO_4 materials due to low carrier concentrations and the large mismatch in protonic vs. electronic conductivities. However, measurements of the current-voltage (I-V) relation of the materials in the fuel cell configuration can yield some insight.

Putting these mixed conducting materials in the fuel cell configuration forces the simultaneous presence of both protonic and electronic charge carriers. We know from measurements in single atmospheres (discussed in Chapter 3) that different charge carriers should dominate on either side of the sample. On the reducing side, the protonic charge carriers are favored, whereas on the oxidizing side, the electronic carriers are favored. At open circuit, steady-state currents of the protons and electron-holes flow in

opposite directions and cancel each other. The fuel cell configuration imposes a large chemical potential gradient on the sample, which makes interpretation of the measured I-V curve difficult. However, choosing certain points on the I-V curve, namely the open-circuit voltage (V_{OC}) and the short circuit current (I_{SC}), allows us to estimate the relative contributions of the different charge carriers.

Herein are reported the I-V curve measurements of various $La_{0.98-x}Ce_xSr_{0.02}PO_4$ samples in the fuel cell configuration. The V_{OC} and I_{SC} are tracked as a function of Ce content, and the results of these measurements are discussed in the context of the standard electrochemical models for mixed conductors.

5.2 Experimental

Several rare earth orthophosphate samples of composition $La_{0.98-x}Ce_xSr_{0.02}PO_4$ were synthesized, with x = 0, 0.14, 0.29, 0.49, 0.79 and 0.98. The same procedure described in Section 4.3.1 was used for powder synthesis. 2 grams of powder for each sample were pressed at 100 MPa in a 380 mm die, yielding discs about 1 mm thick. The discs were sintered at 1450°C in air for 5 hours, yielding samples that were >95% dense. Platinum paste electrodes were applied to the samples, and platinum mesh current collectors were attached using ceramic bond.

The large discs were attached to an open-end alumina tube using ceramic bond. 3% humidified hydrogen gas was flowed through the alumina tube through gas ports. The other side of each disc contacted ambient air. Platinum leads were attached to the current collectors on either side of each disc in order to take dc measurements. The samples were placed in the center of a tube furnace, and a thermocouple was placed about 5 mm from the sample. The furnace was heated at 1°C per minute to 600°C and held at temperature for at least 1 hour in order to fire the ceramic bond.

Open-circuit voltage measurements and dc chronoamperometry measurements were carried out with the sample at 600°C using a Bio-Logic SP-150/VSP/ VMP3 potentiostat. The software used to control measurements and analyze the data was EC-Lab (Bio-Logic). V_{OC}s were determined first. For the I-V curve measurements, various potentials were applied for 3 hours, and the current response was measured as a function of time. When a potential was first applied, the current would jump to a large initial value, then slowly decay and asymptotically approach a steady-state current. 3 hours was an appropriate amount of time to wait to reach steady state for most samples. In between chronoamperometry measurements, the sample was rested at open circuit until the original open circuit potential was obtained again. This could take up to an hour for some of the samples, depending on composition. The potentials applied ranged from below the short circuit current to above the V_{OC}. The measured currents for each sample were normalized for electrode area and sample thickness before being compared to each other. In this work, the standard notation will be that a negative current is extracted from the cell when the cell is doing work, and that a positive current occurs when the cell is driven by the applied potential. Short circuit currents will be negative in sign.

To estimate the short circuit current activation energy for each sample, the temperature was varied between 600-650°C in 10-degree increments, and the same chrono-amperometry measurements described above were carried out. The measured short circuit currents were plotted as a function of temperature in order to obtain the activation energy. The activation energy obtained is only an estimate, because it was only possible to measure in a small temperature range. Larger changes in temperature led to gas leakage due to the difference in the coefficient of thermal expansion between the sample, the alumina tube, and the ceramic bond holding them together.

5.3 Results and Discussion

5.3.1 Multi-component transport model

The fundamental theories for treating mixed conduction in solid-state samples have been well-established by Wagner (*3, 4*). General models for the analysis of I-V curves in a chemical potential gradient are provided by Riess and Liu (*5-7*). The standard electrochemical equations presented here provide a framework for interpretation of the dc current-voltage measurements taken in this work.

The first quantity measured is the open-circuit potential, V_{OC}. It is the potential that exists across a membrane when no external potential is applied, and no current is drawn. For a membrane that is a pure ionic conductor, the open-circuit potential is equal to the theoretical Nernst potential E_N as given in Chapter 1, Equation 1.6. However, if the membrane is a mixed conductor, the picture becomes more complicated. Partial fluxes of multiple charge carriers must be considered. At open circuit, each of the partial currents may be nonzero, but they must sum to zero. That is, no net current flows in an external load, but partial currents of protons and electron-holes can flow in opposite directions in the membrane as long as their charges cancel.

This concept can be expressed as follows. We assume a one-dimensional system with only two charge carriers: electron-holes (e) and protons (i). If each current flow is driven by the gradient in electrochemical potential of its own species, then the currents are given by:

(5.1) $i_i = -(\sigma_i/z_i e)\, d(\eta_i)/dx$

(5.2) $i_e = -(\sigma_e/z_e e)\, d(\eta_e)/dx$

where i_k is the current density of charged species k, σ_k is the conductivity defined by $\sigma_k = e v_k N$ where e is the electronic charge, v_k is the mobility of species k, and N is the particle concentration per unit volume of the species k. z is the charge of the conductive species (+1 for protons, +1 for electron-holes). η_k is the electrochemical potential of species k defined by

(5.3) $d\eta_k = d\mu_k + zF\, d\phi$,

Where μ_k is the chemical potential of species k, and ϕ is the electrical potential.
The total current in the cell is defined as the sum of the partial currents,

(5.4) $i_{tot} = -\Sigma_k(i_k) = i_i + i_e$

This general picture can be simplified when the device is under open circuit. Under this condition, the total current sums to zero: $i_{tot} = 0$.

(5.5) $$i_{tot} = -\sum_k \frac{\sigma_k}{z_k e}\left[\frac{d\mu_k}{dx} + z_k e\frac{d\phi}{dx}\right] = 0$$

Using the definition of the transference number for species k,

(5.6) $t_k = \sigma_k/\sigma_{tot}$

This can be rearranged to give the electrical potential gradient at position x in the sample.

(5.7) $$\frac{d\phi}{dx} = -\sum_k \frac{t_k}{z_k e}\frac{d\mu_k}{dx}$$

To obtain the potential over the sample, it is necessary to integrate Equation (5.7) over the thickness of the sample, from side (I) to side (II). Consider the possible results for the potential obtained from this. The trivial case would be for a pure ionic conductor, in which only one charged species exists. This would give t_k=1 and V, the measured cell potential difference, would come out to equal the Nernst voltage, E_N. Next, consider a membrane with one type of ion and an electronic charge carrier. For this mixed conductor, $t_k < 1$ for each species. Thus, it is necessary to integrate over the chemical potential for both species as in Eq. (5.8).

(5.8) $$V = \int_I^{II} d\phi = -\int_I^{II} \frac{t_i}{z_i e} du_i + \int_I^{II} \frac{t_e}{e} d\mu_e$$

The electronic species is usually dropped from the equation if the contacts on either side of the membrane are the same metal. There should be no difference in chemical potential of electrons and this term goes to zero. This leaves only the fraction of the current carried by the ionic species, the integral over ($t_i/z_i e\ du_i$). In a cell for which there is not a large gradient in chemical potential, the measured V_{OC} can be approximated as equal to the transference number multiplied by the Nernst potential, $V_{OC}=t_i*E_N$. This is the technique usually used to measure transference numbers in a mixed conductor. However, if there is a large gradient in chemical potential, t_i may vary as a function of position. In this case, it is important to remember that the V_{OC} only gives the average contribution of the ionic current to the total. That is, at different physical points in the thickness of the membrane, the

transference number for ions may vary a great deal. As we will see later, this is the case in the orthophosphate system.

The above set of equations can be applied to the rest of the I-V curve as well. To calculate the potential for nonzero total currents, Eq. (5.5) is solved for $d\phi/dx$ without requiring that $i_{tot} = 0$.

(5.9) $$\frac{d\phi}{dx} = \frac{-i_{tot}}{\sigma_{tot}} - \sum_k \frac{t_k}{z_k e}\frac{d\mu_k}{dx}$$

When solving for the potential difference V, the term i_{tot}/σ_{tot} is integrated over the thickness of the sample from side (I) to side (II) as well. This leaves an IR term in the expression for the potential, (where I is current and R is resistance) which corresponds to the Ohmic losses discussed in Chapter 1 as a source of parasitic voltage drop. This IR term will become important for the measurements discussed in the next section.

(5.10) $$V = \int_I^{II} d\phi = -\int_I^{II} \frac{i_{tot}}{\sigma_{tot}} - \sum_n \int_I^{II} \frac{t_n}{z_n e} d\mu_n = -IR - \sum_n \int_I^{II} \frac{t_n}{z_n e} d\mu_n$$

An easy way to visualize the current-voltage relations is to plot the partial current of each species vs. potential separately. Then the total current, which is the experimentally measured quantity, is simply the sum of these two functions. The ultimate simplification of the framework proposed above disregards any variation in chemical potential and assumes that both of the partial currents are linear with respect to the applied potential. The partial current-voltage relations are then expressed as:

(5.11) $i_e = V s_e$

(5.12) $i_i = (E_N - V) s_i$

Where the current's dependence on chemical potentials is simplified such that i_e intercepts the origin, and i_i intercepts E_N at zero current. To calculate the V_{OC}, the partial currents are set as $i_e = - i_i$, and this equation is solved for V.

(5.13) $V_{OC} = E_N/(1+s_e/s_i)$

Equations 5.11 and 5.12 are depicted in Figure (5.1). This analysis will be discussed further when comparing the V_{OC}s measured for this system.

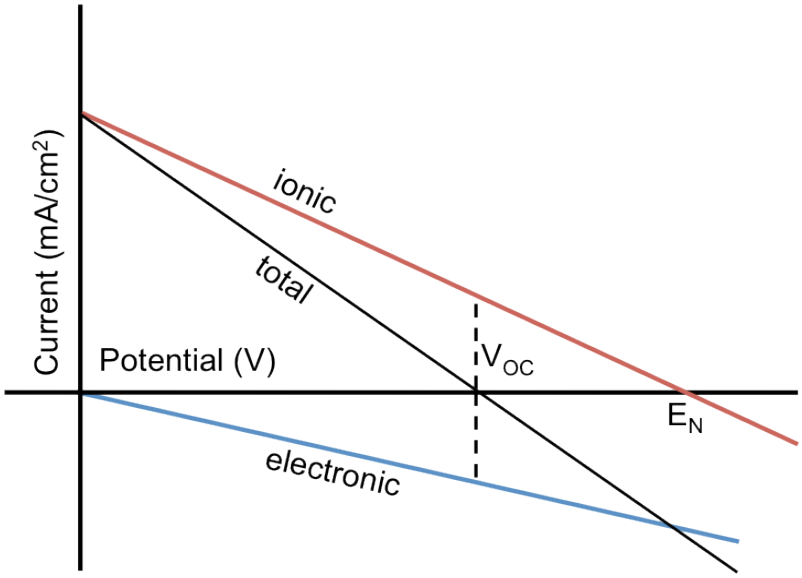

Figure 5.1. One method for estimating the open-circuit potential and the current-potential relations. The partial ionic and electronic currents are plotted separately, and the sum of the two partial currents is equal to the total current. For simplicity, the partial currents are assumed to be linear functions of the applied potential. The open-circuit potential occurs when the ionic and electronic currents cancel each other.

The set of equations (5.11) and (5.12) is the simplest way to depict the partial electronic and ionic currents. Complexity, and increased accuracy, can be added by re-inserting the dependences of the curves on applied voltage, chemical potentials and gradients in carrier concentration. The model by Riess (*6*) assumes that the ionic conductivity remains linear, but introduces nonlinearity into the electronic conductivity. Models by Li (*8*), Duncan (*9*), and Liu (*7*) model the ionic currents to be nonlinear as well. Schematics of I-V plots from the Riess and Liu models are pictured in Figure (5.2). A quantitatively accurate model of a material requires knowledge of carrier concentration dependences on chemical potentials, applied potentials, etc. which are not known for this system. However, some final qualitative insights into the I-V curves can be gleaned from the basic, linear models. Riess takes Equations (5.11) and (5.12) and adds them to get the total current,

(5.14) $i_{tot} = i_i + i_e = (E_N\text{-}V)s_i - Vs_e$

Picking values of V for this curve shows where the different charge carriers dominate. For the value $V = E_N$, the ionic current i_i disappears, and the total current is purely electronic. For $V = 0$, which defines the short circuit current, the electronic current i_e vanishes and the total current should be purely ionic. Between these two extremes, the relative contributions of the electronic and ionic currents will vary. As discussed above, at the V_{OC} the partial currents balance each other. In the next section, the measured I-V curves are quantitatively compared by recording the currents at these particular V values.

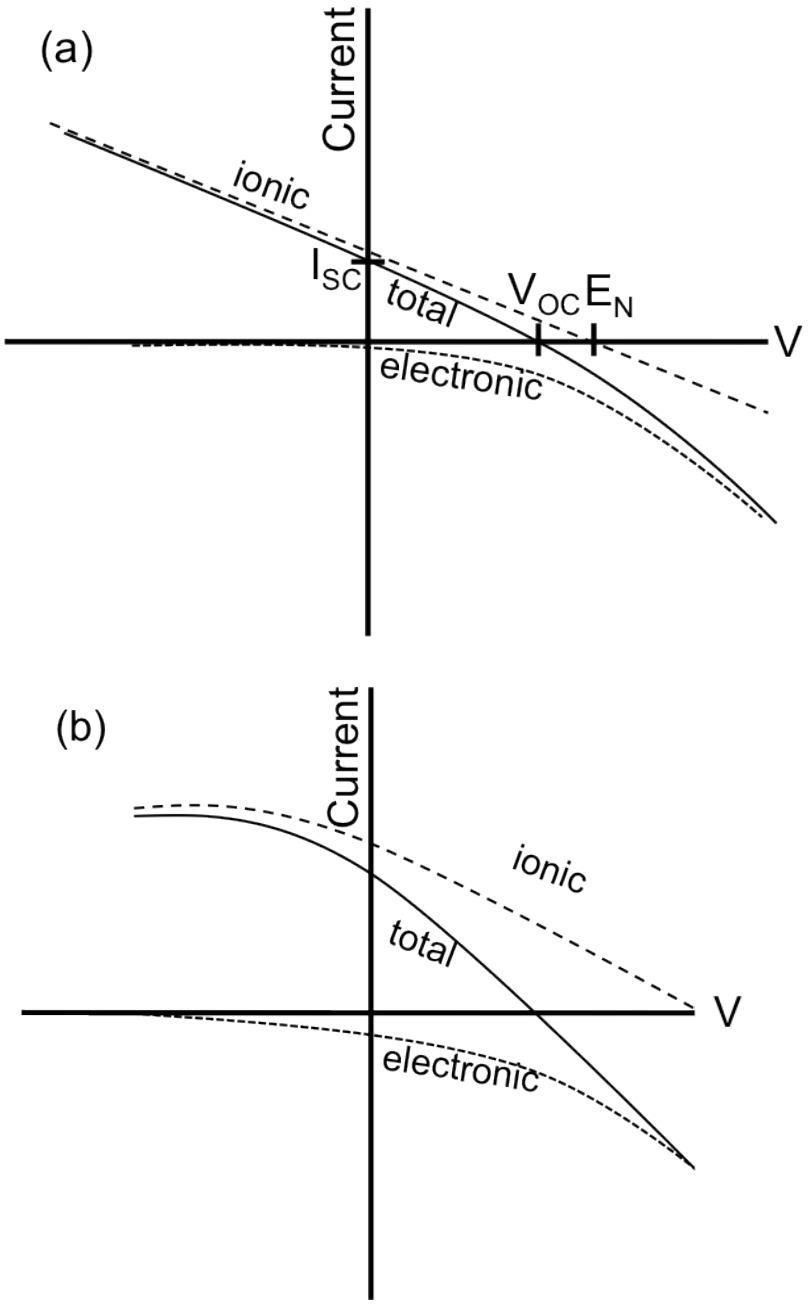

Figure 5.2. Schematics of mixed conduction models. (a) A sample mixed conduction model from Riess. The ionic current does not vary with chemical potential, but the electronic current does. (b) A sample mixed conduction model from Liu. The fluxes of ions and electrons both vary as a function of chemical potential and material parameters such as doping.

The set of equations discussed above should give some insight into the shapes of the measured I-V curves. Modification of this simple model may be necessary to fully understand the effects at work. It is important to remember that this model assumes that the flux of a given species is driven only by the gradient in its own electrochemical potential: no explicit Onsager cross-terms are included here.

5.3.2 Results

Figure 5.3 shows the chronoamperometry measurements taken for the sample $Ce_{0.98}Sr_{0.02}PO_4$. These measurements are a representative example of all of the raw data that were translated into the I-V curves. For each measurement, the V_{OC} is measured first. For the sample presented below, the V_{OC} occurred at 0.32V. Next, various potentials are applied, and the currents are measured as a function of time. The total potential values (OCV-applied potential) are listed in the legend. Measurements were taken for several potentials ranging from V=0 to $V=E_N$, the theoretical Nernst potential, but only a subset of these are presented here.

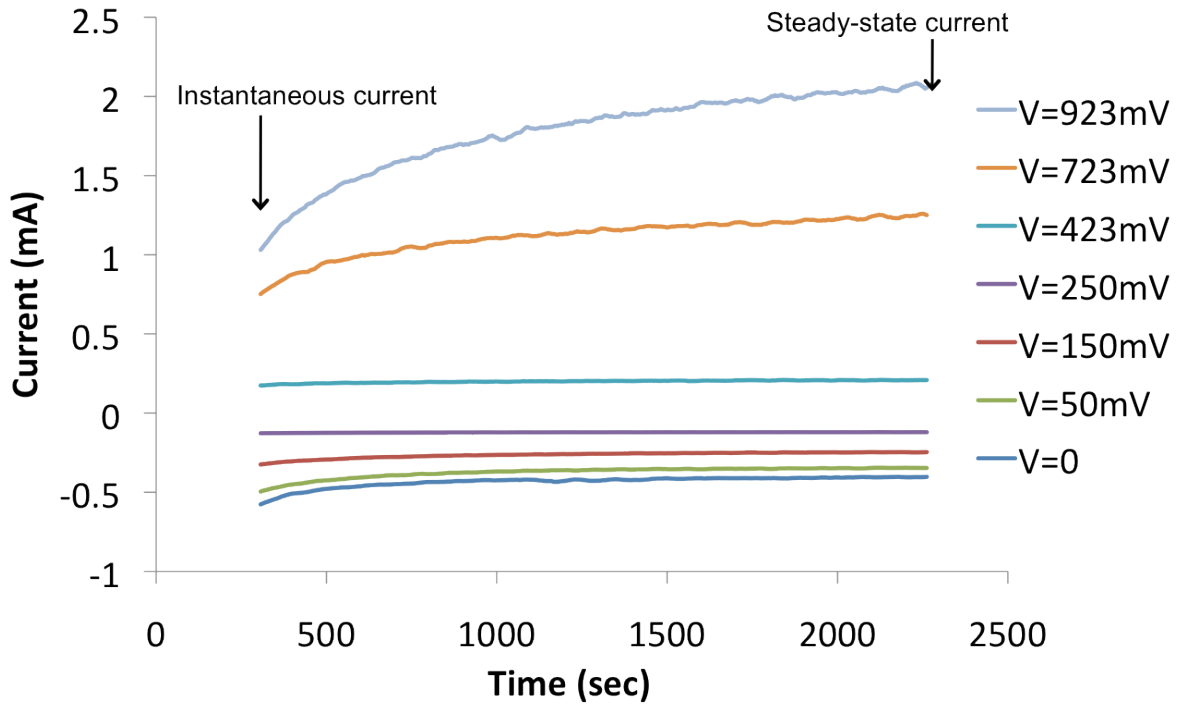

Figure 5.3. Sample chronoamperometry experiment, carried out at 600°C on a $Ce_{0.98}Sr_{0.02}PO_4$ sample exposed to 3% humidified hydrogen and ambient air. Potentials range from V = 0 to V = 0.923 V. The V_{OC} was measured to be 0.32V. Instantaneous current measurements are taken at the point in time indicated. Steady-state currents were obtained after a period of time, 1-3 hours. The two upper curves have not yet reached steady-state, and the value of the current was recorded at a later time than pictured.

From the data pictured above, both the instantaneous and the steady-state currents could be recorded and compared, as in Figure 5.4. The value for the instantaneous current is taken from the peak of the chronoamperometry curve, while the steady-state value is taken from the end of the measurement. The I-V curve for the instantaneous current vs. potential is linear. It shows a resistance on the order of the value obtained using ac impedance measured for the same sample in oxidizing conditions. This is expected—since electron-holes are more mobile than protons, it makes sense that they would respond more quickly to an applied potential. The current decays over time to a lower, steady-state value. The

decay reflects the redistribution of the charge carrier profile inside the sample. Over time, a gradient in charge carriers builds up in order to counteract the applied potential. This causes the decrease in current. That is, microscopically, the protons and holes are redistributing through the sample. The dopants in this case should not be moving. As noted in the experimental section, some of the samples required rest time in between measurements in order to return to the original V_{OC}. This is because the charge carrier buildup needed time to relax back to its equilibrium state.

The steady-state I-V curve is nonlinear. The shape of the curve is similar to the model by Riess that has dominant electronic conductivity on one side of the physical sample, and dominant ionic conductivity on the other (*6*), as pictured in Figure 5.2 (a). This is a good description of the present sample as well. In Figure 5.4, the values for V=0, V=V_{OC}, and V=E_N are indicated. For different potential ranges, the slope of this curve takes different values. The slope of the curve for potentials in the range $0<V<V_{OC}$ is steeper than the slope of the curve in the potential range $V_{OC}<V<E_N$. By comparison to the Riess model, this would indicate that the former region has a higher proportion of ionic current and the latter has dominant electronic current. This makes sense for this sample because applying $V>V_{OC}$ drives the cell backward, injecting holes, while $V<V_{OC}$ draws protonic current through the cell.

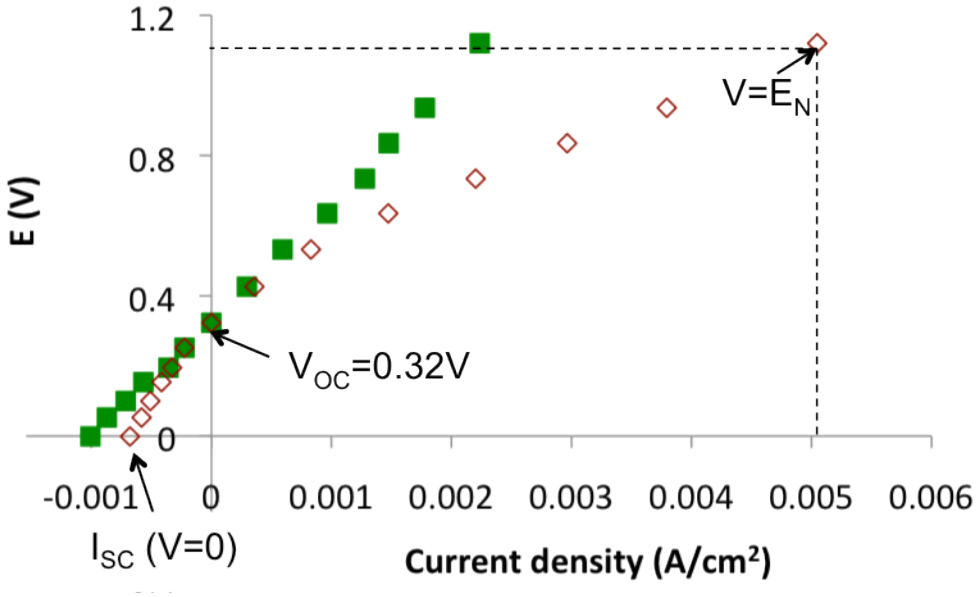

Figure 5.4. Instantaneous (filled squares) and steady-state (diamonds) currents measured at various applied potentials for the $Ce_{0.98}Sr_{0.02}PO_4$ sample at 600°C in the fuel cell configuration.

Steady-state I-V curves were obtained for the $La_{0.98-x}Ce_xSr_{0.02}PO_4$ samples with compositions x = 0, 0.14, 0.29, 0.49, 0.79, and these were compared to the $Ce_{0.98}Sr_{0.02}PO_4$ sample discussed above. All of these measured I-V curves are pictured in Figure (5.5). The intercept of the curves with the y-axis give the V_{OC}, and the intercept of the curves with the x-axis give the I_{SC}. A few trends can be noted from this image. As the Ce content increases,

the slopes of the curves decrease, the V_{OC} decreases, and the I_{SC} grows more negative—that is, its absolute value increases. The $La_{0.98}Sr_{0.02}PO_4$ (x=0) composition has an extremely high slope, and the V_{OC} = 1.1 = E_N. It also has an extremely low I_{SC} = $3x10^{-5}$ A. All of the other samples have lower V_{OC} and larger I_{SC}. The significance of these effects will be discussed individually when the V_{OC} and I_{SC} are plotted vs. Ce content. One final observation of the full I-V curves is that the compositions with higher Ce content (x = 0.79, 0.98) gave curves with two distinct slopes above and below V_{OC}. The I-V curves with lower Ce contents (x = 0, 0.14, 0.29) were more linear. This illustrates that there is a continuum of mixed conduction levels represented by all of these samples. The transition between purely ion-conducting to mixed conducting with various levels of electron conductivity can be qualitatively observed.

Next, the I_{SC} and V_{OC} are plotted separately as a function of Ce content.

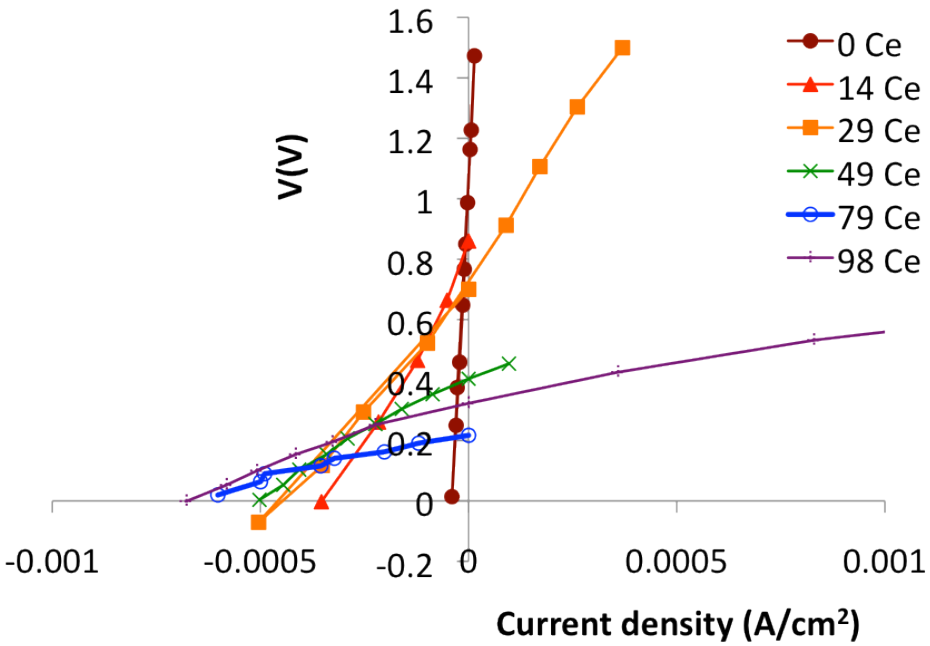

Figure 5.5. Steady-state I-V curves for $La_{0.98-x}Ce_xSr_{0.02}PO_4$ samples taken in the fuel cell configuration at 600°C. The samples tested are compositions for which x = 0, 0.14, 0.29, 0.49, 0.79, and 0.98.

Figure (5.6) shows the measured V_{OC} plotted as a function of Ce content. At x = 0, the V_{OC} = E_N = 1.1 V. As the Ce content increases, the V_{OC} decreases monotonically. The relationship is almost linear, and there is some scatter in the measurements for the higher Ce content samples. This could be due to gas leakage through the ceramic bond seals. Since increasing the Ce content increases the electronic conductivity in the sample, decreasing V_{OC} is expected. However, the relatively low magnitude of its decrease is surprising. This deserves some discussion.

The open-circuit potential is often used as a figure of merit to evaluate fuel cell voltage efficiency. An electrolyte with a V_{OC} = 0.32 V when E_N = 1.1V would be evaluated as being 0.32/1.1=29% efficient. Such a material would never be used as an electrolyte due to low

efficiency: a materials design parameter for fuel cell electrolytes is to maximize the V_{OC}! However, more information can be gleaned from this measurement than just the fact that it is low efficiency.

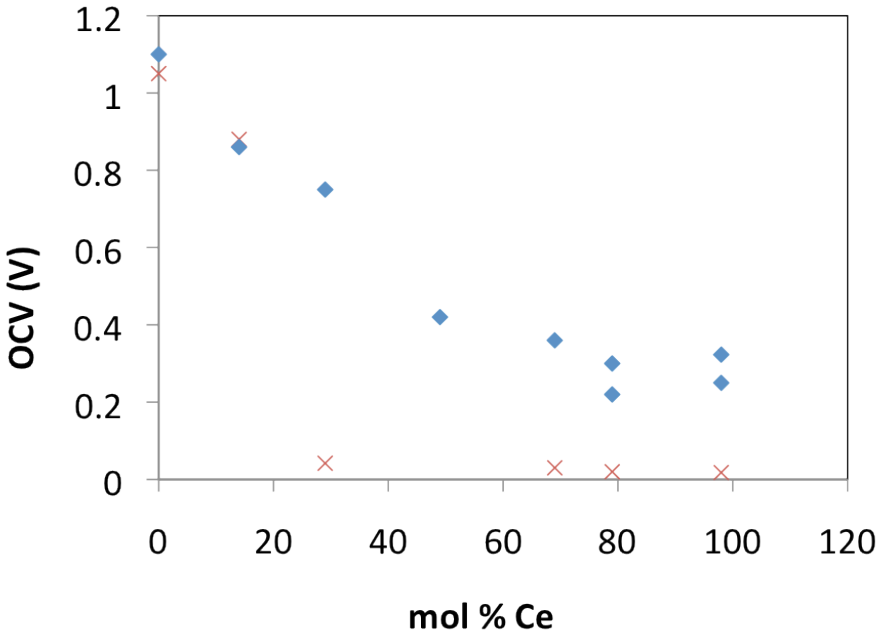

Figure 5.6. The open circuit potentials decrease as a function of the Ce content in $La_{0.98-x}Ce_xSr_{0.02}PO_4$. The measured values are tracked with blue diamonds. The expected values from the simplistic model are tracked with red x's.

As pictured in Figure 5.1, one way to predict the open-circuit voltage of a sample would be to estimate its partial electronic and ionic conductivity, then plot them linearly according to Equations (5.11) and (5.12). This exercise assumes that the V_{OC}/E_N is a perfect estimate of the ionic transference number: there is no variation in the currents with the chemical potential. All values of the V_{OC} predicted using this method are plotted in Figure 5.6. The plots used to obtain the values of V_{OC} are shown in Figure 5.7.

In Figure 5.7, the ionic conductivity is estimated to be constant at $1.2x10^{-4}$ S/cm, the value measured for all samples in reducing conditions at 600°C. The electronic conductivity for each sample is taken from the measurement in oxidizing conditions at 600°C. This conductivity varies by orders of magnitude as the Ce content changes. The absolute values of the partial currents are plotted so that the curves will intersect at the V_{OC}. Figure 5.7 (a) plots the full curves. Figure 5.7 (b) plots the curves at different y-axis scale so that the intersections—the V_{OC}—can be observed. The ionic partial current, H, intercepts the x=0 and x=0.14 partial electronic currents at high potentials. This gives estimates for the V_{OC} of about 1.05 and 0.88V, respectively. However, the rest of the samples have very high measured electronic conductivity, and this results in very low estimates for the V_{OC}. The $Ce_{0.98}Sr_{0.02}PO_4$ sample would from this method of estimation have a V_{OC} of 0.018V, about 15 times lower than 0.32, the actual measured value. The expected contribution of ions to the

average transference number from this estimation would be 1.6%. Thus, the measured V_{OC} is surprisingly high!

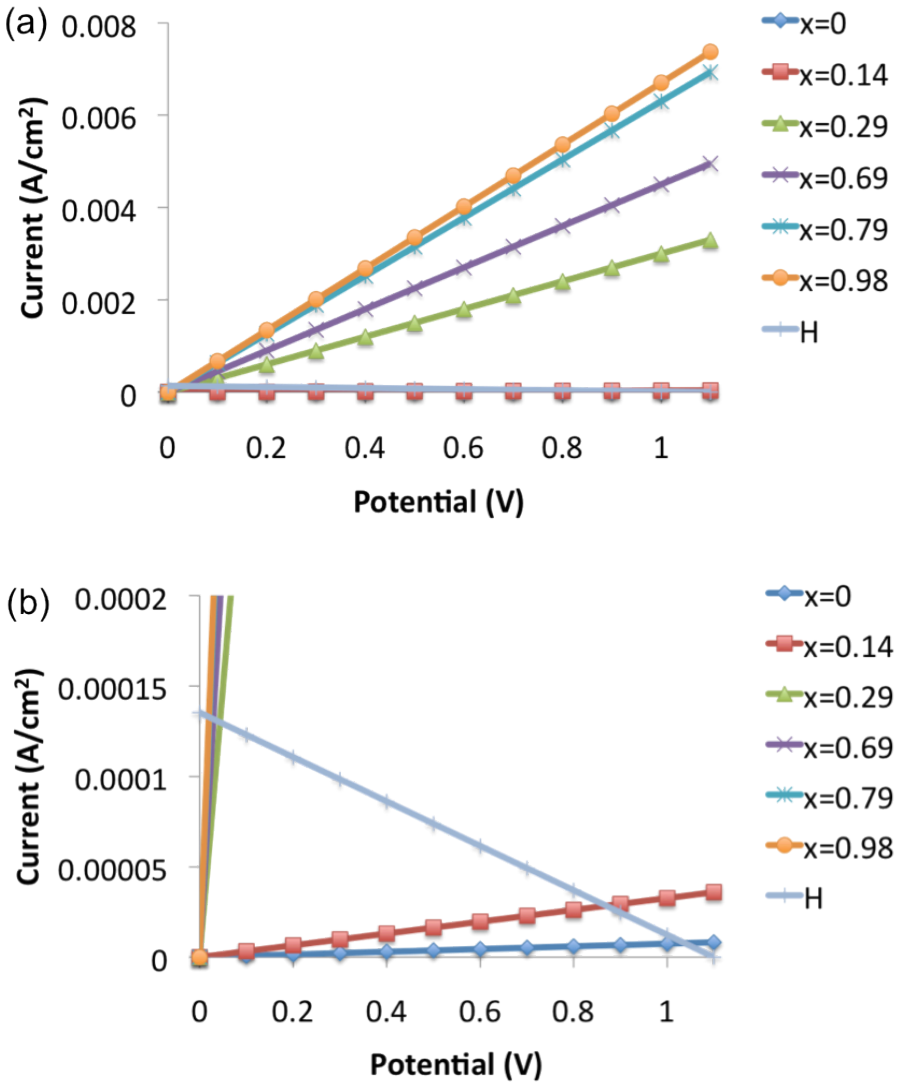

Figure 5.7. I-V plots of the estimated electronic and ionic partial currents in the series $La_{0.98-x}Ce_xSr_{0.02}PO_4$. at 600°C. The partial ionic current is labeled H in the legend and has a negative slope, intercepting E_N=1.1V. The slope of this curve is taken from the total conductivity measurements of $La_{0.98}Sr_{0.02}PO_4$ in humidified hydrogen. The partial electronic currents intercept the origin. Their slopes are estimated from total conductivity measurements for each composition in oxidizing conditions. The intersection of the ionic with the electronic currents estimates the V_{OC}. (a) All curves are plotted on the same axes. (b) The same curves are plotted with a different y axis scale in order to track their intersections.

Evidently, the fuel cell condition imposes a large chemical gradient that affects the protonic and/or the electronic I-V curves very strongly. To attain such a high V_{OC} for the $Ce_{0.98}Sr_{0.02}PO_4$ sample, either the protonic current must increase or the electronic current must decrease, or both. These changes would occur as a function of position in the

membrane. We hypothesize a thin, reduced layer that dominantly conducts protons on the reducing side, and dominant hole conduction through the rest of the thickness.

Next we discuss the trends in the measured I_{SC} with Ce content.

Figure (5.8) plots the absolute value of the measured short circuit currents vs. the Ce content of the sample. These are the x-intercepts of the curves shown in Figure (5.5). This plot shows that the I_{SC} for the $La_{0.98}Sr_{0.02}PO_4$ sample is extremely low: 0.04 mA/cm^2. On increasing the Ce content to 14%, the I_{SC} increases by about an order of magnitude. On increasing the Ce content further, the I_{SC} continues to increase but on a smaller scale: the I_{SC} for the $Ce_{0.98}Sr_{0.02}PO_4$ sample is only about 1.5 times that of the x = 0.14 sample. This type of extreme increase in a property on changing composition is not unique. In Chapter 4, the total conductivity in oxidizing conditions of this same sample series increased dramatically at about 5% Ce content, and this was attributed to a percolation phenomenon. Further measurements would be necessary to identify the precise threshold location for the I_{SC}.

As discussed in Section 5.3.1, for the simple Riess model of the IV curve, the I_{SC} is taken to be purely ionic current. This follows from the assumption that electronic conduction is driven only by a difference in electron chemical potential, and that when V=0, the electronic carriers have no driving force to move. This implies that the increase in I_{SC} indicates an order of magnitude increase in the purely ionic current upon increasing the Ce content. This is quite unexpected; it is an obserevation that to the best of our knowledge has not been reported before. Increasing the Ce content increases the electronic contribution to the total current. A concurrent increase in I_{SC} indicates an enhancement effect: coupling of some kind between the charge carriers.

If the two currents were not coupled, the ionic current would be expected to stay the same, or if anything, decrease with increasing Ce content. The ionic current would decrease because of lowered carrier concentration. As described in Chapter 1, the holes and protons are extrinsic defects and compete with each other to charge-compensate the dopant, whose level for this series of samples is fixed at 2 mol %. Thus, since there is a large increase in I_{SC} rather than a decrease, there must be another phenomenon at work

One well-known type of charge carrier coupling that occurs in ionic mixed conductors is known as ambipolar diffusion. This coupling arises because of the requirement of local charge neutrality in all solids: the energetic penalty for charge separation is extremely high. In an ionic solid, all diffusing species are charged. The diffusion of any one species thus requires the concurrent diffusion of another species in order to charge compensate its movement. This gives a transport coefficient known as the ambipolar conductivity, which for a system with one type of ionic and one type of electronic carrier would be

$$\sigma_{amb} = \sigma_{tot} t_i t_e = \sigma_i t_e = \frac{\sigma_i \sigma_e}{\sigma_i + \sigma_e} \quad (5.14)$$

However, such enhancements of the slow carrier in the case of ambipolar diffusion are well-known to be limited to a factor of 2. The factor of 10 increase in I_{SC} measured here is significantly higher than this, which indicates that the nature of the carrier coupling is different from simple ambipolar diffusion. More factors must be taken into account than just charge compensation.

In an attempt to gain more insight into this novel coupled conduction mechanism, the activation energies of the short circuit currents were measured.

Activation energies of the short circuit currents were estimated by taking measurements with V=0 in a small range of temperatures above 600°C. The x=0 sample had the activation energy = 1.1 eV, similar to the activation energy measured for samples measured in single-atmosphere conditions with pure proton conduction. For samples with x>0, a quantitative trend in activation energy could not be established other than it was generally lower. The measured activation energies ranged between 0.40-0.80 eV, and are given in Table 5.1. The large scatter in values likely results from the narrow temperature domain of the measurement. While the data do indicate a trend towards lower activation energies when Ce is present, a more quantitative relationship could not be established.

Table 5.1

Ce content (mol %)	Activation energy (eV)
0	1.12
29	0.53
69	0.79
98	0.40

The lowered activation energy indicates that the mechanism for proton conduction may be modified. This could occur in several ways. One way that this could occur is that electron-holes present in the material could help protons escape from dopant traps. As discussed in (*10*), first-principles calculations performed by Nicole Adelstein of our group show that the protons are electronically attracted to Ba dopants in $LaPO_4$ with a binding energy of 0.2 eV. Studies by Jonathan Solomon in our group (*11*) and other groups (*12*) show that the binding energy of the proton to Sr dopants in $LaPO_4$ is 0.31 eV. This attraction forms traps for protons moving through a material, which slows their total conductivity. First-principles calculations performed by Nicole Adelstein of our group show that the electron-holes can form associates with dopants with a binding energy of about 0.1eV (*13*). More calculations would be needed to determine to what extent the proximity of electron holes could reduce the proton-dopant binding energy of 0.31eV (*10*). It would be reasonable to expect that since both the protons and electron-holes are positively charged, that they should repel each other, and indeed lower the magnitude of the binding energy. This binding energy is quite significant compared to the overall activation energy for motion. If it could be reduced, then proton movement could be enhanced greatly.

Next, we will discuss the interaction of the trends in V_{OC} and I_{SC} and how they affect the power density of the samples.

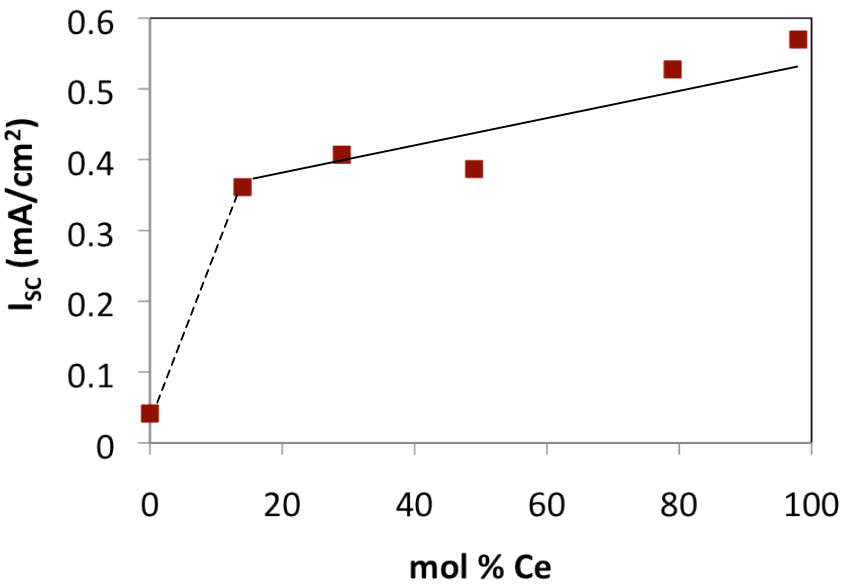

Figure 5.8. The measured short circuit currents increase nonlinearly with the Ce content of the $La_{0.98-x}Ce_xSr_{0.02}PO_4$ sample. Lines are included to guide the eye.

Power densities for each sample were calculated by multiplying the measured current densities by the applied voltage according to P=IV. These power densities are plotted vs. the current density in Figure 5.9. Parabolic fits are used to guide the eye. The plot shows that the power density for the $La_{0.98}Sr_{0.02}PO_4$ sample is very low, with a peak power density of about 0.01 mW/cm^2. Adding 14% Ce to the composition increases the peak power density by a factor of 5. Increasing the Ce content from here does not give a single trend. Measured peak power densities range from 0.03 to 0.07 mW/cm^2.

The trends in I_{SC} and V_{OC} would predict that some maximum in power density would be attained at an optiumum Ce content. Since V_{OC} decreases approximately linearly with Ce content, and I_{SC} increases a great deal between 0 and 15% Ce, this maximum would be predicted to be at 14% Ce. The actual maximum power is measured for the 29% Ce sample, but the maximum power for the 14% sample is not far below this. As the Ce content increases above 29%, the added electronic conductivity decreases the V_{OC} which should decrease the power output. This is true for the 49% and 79% Ce samples. The $Ce_{0.98}Sr_{0.02}PO_4$ sample breaks this downward trend. The particular sample measured here had a higher V_{OC} than the 79%Ce sample and a higher I_{SC}; this would explain its better power performance.

The power densities and current densities reported in Figure (5.9) are very low—several orders of magnitude lower than the performance required for an optimized, commercial fuel cell. However, this experiment proves the concept that small amounts of electronic conductivity can enhance ion conduction and power density. For the 14% Ce sample, the V_{OC} is lowered by 20% from theoretical, but the power density increased by a factor of 5 compared to the pure ionic conductor. This enhancement is thought to stem from coupling effects between protons and electron-holes. This concept might posssibly be exploited for use in real applications using other, more conductive materials.

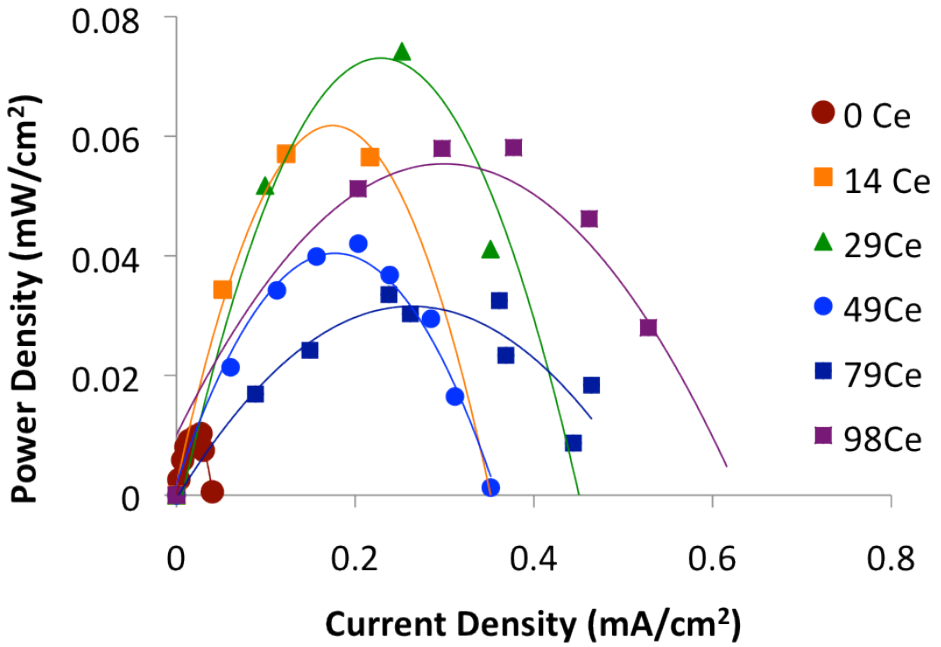

Figure 5.9. Power densities of the $La_{0.98-x}Ce_xSr_{0.02}PO_4$ samples. The composition with 0 Ce content has an order of magnitude lower maximum power density than the other samples. Parabolic fitting curves are used as guides to the eye.

5.4 Conclusion

Measurement of the I-V curves for the mixed conductors $La_{0.98-x}Ce_xSr_{0.02}PO_4$ in the fuel cell configuration shows an order of magnitude enhancement of the short-circuit current as the Ce content is increased from 0 to 98%. This is interpreted as enhanced proton conduction, and translates to a factor of 7 power enhancement for the fuel cell devices. This is unexpected, since added Ce content results in higher electronic conductivity. The enhancement in proton conductivity with higher electronic conductivity is attributed to an unusual coupling effect between the charge carriers.

Evidence that increasing the Ce content in the samples $La_{0.98-x}Ce_xSr_{0.02}PO_4$ increases the electronic conductivity is noted from several different measurements. First, the measured I-V curve for the $La_{0.98}Sr_{0.02}PO_4$ sample is linear, whereas the samples with high Ce contents are bent, with different slopes for $V<V_{OC}$ and $V>V_{OC}$. This shape is characteristic of a material with electronic conduction. Second, the V_{OC} decreases monotonically with increasing Ce content: this is also indicative of increased electronic conductivity. Finally, the percolation model described in Chapter 4 for this same series implies that at a critical Ce content, a connected network of Ce hosting sites is formed for electronic carriers to travel. The shape of the percolation curve for the series in oxidizing conditions is echoed here in the shape of the trend in I_{SC} with Ce content. If there is an enhancement of ionic conduction with electronic conduction, it makes sense that the critical formation of this

connected pathway for electronic conduction would have an extreme effect on ionic conduction.

The short-circuit current measured for the $Ce_{0.98}Sr_{0.02}PO_4$ material is higher than the conductivity of $La_{0.98}Sr_{0.02}PO_4$ in reducing conditions by about a factor of about 5. Thus, the combination of the ionic and electronic currents gives an enhancement in ionic conductivity. This enhancement cannot be attributed solely to increased carrier concentration. The carrier concentration measured by NMR (*14*) and the value estimated using the transient measurement in Chapter 3 are less than 0.5 mol% H^+. Both values multiplied by a factor of 5 would give >2 mol% protons, which would be larger than the nominal doping level of the material. In addition, since protons and holes compete for incorporation, it is unlikely that the level of protons in the material could reach this level. Other possible mechanisms for ionic current enhancement could be that electron-holes mediate dissociation of pyrophosphates in the sample to incorporate more protons. The electron-holes could also help to dissociate protons from electronic attraction to dopants. A combination of several of these different effects could be responsible for the current enhancement observed.

The large gradient in chemical potential imposed by the fuel cell configuration significantly changes the charge carrier profile in the cell—the simple model illustrated in Figure 5.1 predicts values of the V_{OC} more than an order of magnitude lower than the measured value. This, as well as the observed time lag in attaining steady-state current, supports our hypothesis that there may be a reduced layer of material with high proton content near the hydrogen side of the membrane, and a large gradient in proton content as a function of position in the membrane. This causes the total resistance of the membrane, the IR term in Equation (5.10), to be lowered substantially for samples containing large amounts of Ce. This contributes to the increased I_{SC} as well.

The concept of enhancing ion conduction by introducing a small amount of electronic conduction could fundamentally change the way that materials for electrolyte applications are designed.

References

References for Chapter 1

1. R. K. Pachauri, Reisinger, A. (Eds.), "Climate Change 2007: Synthesis Report Contribution of Working Groups I, II and III to the Fourth Assessment Report of the Intergovernmental Panel on Climate Change" (2007).
2. O. Edenhofer, Pichs-Madruga, R., Sokona,Y., Seyboth, K., Matschoss, P., Kadner, S., Zwickel, T., Eickemeier, P., Hansen, G., Schloemer, S., von Stechow, C. (Eds.), "Renewable Energy Sources and Climate Change Mitigation" (IPCC, 2011).
3. Z. Yang, Zhang, J., Kintner-Meyer, M.C.W., Lu, X., Choi, D., Lemmon, J.P., Liu, J., *Chemical Reviews*, (2012).
4. K. Kordesch, Simader, G., *Fuel Cells and Their Applications*. (VCH Publishers, Inc., New York, 1996).
5. R. O'Hayre, Cha, S.-W., Colella, W., Prinz, F. B., *Fuel Cell Fundamentals*. (John Wiley & Sons, Hoboken, NJ, 2006).
6. G. Harley, Yu, R., De Jonghe, L.C. , *Solid State Ionics* **178**, 769 (2007).
7. T. Norby, *MRS Bullletin* **34**, 923 (2009).
8. D. A. Boysen, Uda, T., Chisholm, C. R. I., Haile, S. M., *Science Online Express* **303**, 68 (2004).
9. L. Onsager, *Physical Review* **37**, 405 (1931).
10. C. Wagner, *Progress in Solid-State Chemistry* **10**, 3 (1975).
11. D.-K. Lee, Yoo, H.-I., *Physical Review Letters* **97**, 255901 (2006).
12. H.-I. Yoo, Yoon, J.-Y., Ha, J.-S., Lee, C.-E., *Physical Chemistry Chemical Physics* **10**, 974 (2008).
13. A. V. Virkar, *Solid State Ionics* **140**, 275 (2001).
14. M. Liu, *Journal of the Electrochemical Society* **144**, 1813 (1997).
15. N. Adelstein. (2012).
16. M. Sanders, O'Hayre, R., *Journal of Materials Chemistry* **20**, 6271 (2010).
17. A. V. Virkar, *International Journal of Hydrogen Energy* **35**, 9527 (2010).
18. K. Byrappa, *Prog. Crystal Growth and Charact.* **13**, 163 (1986).
19. E. Gomez del Moral, Fagg, D. P., Chinarro, E., Abrantes, J. C. C., Jurado, J. R., Mather, G. C., *Ceramics International* **35**, 1481 (2009).
20. T. Norby, Christiansen, N., *Solid State Ionics* **77**, 240 (1995).
21. K. Amezawa, Maekawa, H., Tomii, Y., Yamamoto, N., *Solid State Ionics* **145**, 233 (2001).
22. K. Amezawa, Tomii, Y., Yamamoto, N., *Solid State Ionics* **176**, 135 (2005).
23. N. Kitamura, Amezawa, K., Tomii, Y., Hanada, T., Yamamoto, N., Omata, T., Otuska-Yao-Matsuo, S., *Journal of the Electrochemical Society* **152**, A658 (2005).
24. N. Kitamura, Amezawa, K., Tomii, Y., Yamamoto, N., *Solid State Ionics* **162-163**, 161 (2003).
25. K. Amezawa, Tomiga, T., Yamamoto, N., Hanada, T., Tomii, Y., *Journal of the American Ceramic Society* **88**, 3211 (2005).
26. K. Amezawa, Uchimoto, Y., Tomii, Y., *Solid State Ionics* **177**, 2407 (2006).
27. G. Harley, De Jonghe, L. C., *Solid State Ionics* **181**, 424 (2010).

28. G. Harley, Kreuer, K. D., Maier, J., De Jonghe, L. C., *Journal of Non-Crystalline Solids* **355**, 932 (2009).
29. G. Zhang, Yu, R., Vyas, S., Stettler, J., Reimer, J. A., Harley, G., De Jonghe, L. C., *Solid State Ionics* **178**, 1811 (2008).
30. G. Zhang, Wang, R., De Jonghe, L. C., *Solid State Ionics* **180**, 941 (2009).
31. G. Zhang, Yu, R., De Jonghe, L. C., *Solid State Ionics* **217**, 34 (2012).
32. A. Unemoto, Kitamura, N., Amezawa, K., *Electrochemical and Solid State Letters* **12**, B43 (2009).
33. N. Kitamura, Amezawa, K., Tomii, Y., Hanada, T., Yamamoto, N., *Solid State Ionics* **176**, 2875 (2005).
34. H. D. Park, Kriedler, E. R. , *Journal of the American Ceramic Society* **67**, 23 (1984).
35. Y.-M. Chiang, Birnie, D., Kingery, W. D. , *Physical Ceramics - Principles for Ceramic Science and Engineering*. (John Wiley & Sons, New York, 1997).
36. H. L. Tuller, Bishop, S. R., *Annu. Rev. Mater. Res.* **41**, 369 (2011).
37. T. Norby, in *UCSB-ICMR Summer School on Inorganic Materials for Energy Conversion and Storage*. (University of California, Santa Barbara, 2012).
38. J. Solomon, Adelstein, N., Asta, M., De Jonghe, L. C. , *Electrochemical Society Transactions*, (2012).
39. R. Yu, De Jonghe, L. C., *Journal of Physical Chemistry* **111**, 11003 (2007).
40. K. Toyoura, Hatada, N., Nose, Y., Tanaka, I., Matsunaga, K., Uda, T., *J. Phys. Chem. C* **116**, 19117 (2012).
41. N. Adelstein, Neaton, J.B., Asta, M., De Jonghe, L.C., *Journal of Materials Chemistry* **22**, 3758 (2012).
42. K. Amezawa, Kjelstrup, S., Norby, T., Ito, Y., *J. Electrochem. Soc.* **145**, 3313 (1998).
43. N. Adelstein, Mun, B.S., Ray, H. L., Ross, P.N., Neaton, J.B., De Jonghe, L.C. , *Physical Review B* **83**, 205104 (2011).
44. K. L. Duncan, Lee, K.-T., Wachsman, E.D., *Journal of Power Sources* **196**, 2445 (2011).
45. I. Riess, *J. Phys. Chem. Solids* **47**, 129 (1986).

References for Chapter 2

1. K. Byrappa, *Prog. Crystal Growth and Charact.* **13**, 163 (1986).
2. S. Lucas, Champion, E., Bregiroux, D., Bernache-Assollant, D., Audubert, F., *J. Solid State Chem.* **177**, 1302 (2004).
3. K. Amezawa, Maekawa, H., Tomii, Y., Yamamoto, N., *Solid State Ionics* **145**, 233 (2001).
4. K. Amezawa, Kitajima, Y., Tomii, Y., Yamamoto, N., Wideroe, M., Norby, T., *Solid State Ionics* **176**, 2867 (2005).
5. K. Amezawa, Tomii, Y., Yamamoto, N., *Solid State Ionics* **176**, 135 (2005).
6. N. Kitamura, Amezawa, K., Tomii, Y., Hanada, T., Yamamoto, N., Omata, T., Otuska-Yao-Matsuo, S., *Journal of the Electrochemical Society* **152**, A658 (2005).
7. T. Norby, Christiansen, N., *Solid State Ionics* **77**, 240 (1995).
8. R. Yu, De Jonghe, L. C., *Journal of Physical Chemistry* **111**, 11003 (2007).
9. G. Harley, Yu, R., De Jonghe, L.C. , *Solid State Ionics* **178**, 769 (2007).
10. S. Lucas, Champion, E., Bernache-Assolant, D., Leroy, G., *J. Solid State Chem.* **177**, 1312 (2004).

11. D. Bregiroux, Lucas, S., Champion, E., Audubert, F., Bernache-Assollant, D., *Journal of the European Ceramic Society* **26**, 279 (2006).
12. H. D. Park, Kriedler, E. R. , *Journal of the American Ceramic Society* **67**, 23 (1984).
13. T. Hernandez, Martin, P., *Journal of Alloys and Compounds* **466**, 569 (2008).
14. X. Sun, Wang,S., Wang, Z., Ye, X., Wen, T., Huang, F., *Solid State Ionics* **179**, 1138 (2008).
15. H. Hirai, Masui, T., Imanaka, N., *Journal of Alloys and Compounds* **374**, 84 (2004).
16. K. Nahdi, Ferid, M., Ayadi, M. T., *Journal of Thermal Analysis and Calorimetry* **96**, 455 (2009).
17. N. Clavier, Podor, R., Dacheux, N., *Journal of the European Ceramic Society* **31**, 941 (2011).
18. G. Harley, Kreuer, K. D., Maier, J., De Jonghe, L. C., *Journal of Non-Crystalline Solids* **355**, 932 (2009).
19. R. N. Bell, *Inorganic Syntheses* **3**, 103 (1950).
20. O. A. Serra, Giesbrecht, E., *J. Inorg. Nucl. Chem.* **30**, 793 (1968).
21. Z. A. Munir, Anselmi-Tamburini, U., *Journal of Materials Science* **41**, 763 (2006).
22. H. L. Ray, Zhao, N., De Jonghe, L. C., *Electrochimica Acta* **78**, 294 (2012).
23. K. M. White, Lee, P.L., Chupas, P.J., Chapman, K.W., Payzant, E.A., Jupe, A.C., Bassett, W.A., Zha, C.-S., Wilkinson, A.P., *Chem. Mater.* **20**, (2008).
24. M. L. Einsla, Mukundan, R., Brosha, E., Garzon, F.H., *ECS Transactions* **11**, 347 (2007).
25. M. Nagao, Takeuchi, A., Heo, P., Hibino, T., Sano, M., Tomita, A. , *Electrochemical and Solid-State Letters* **9**, A105 (2006).
26. H. Onoda, Inagaki, Y., Kuwabara, A., Kitamura, N., Amezawa, K., Nakahira, A., Tanaka, I., *Journal of Ceramic Processing Research* **11**, 344 (2010).
27. N. K. Beck, De Jonghe, L.C., *Electrochemical and Solid-State Letters* **12**, B11 (2009).
28. C. R. Kreller, Wilson, M. S., Mukundan, R., Brosha, E. L., Garzon, F. H., in *PRiME 2012*. (The Electrochemical Society, Honolulu, HI, 2012), vol. Abstract #1964.
29. K. Amezawa, Tomiga, T., Yamamoto, N., Hanada, T., Tomii, Y., *Journal of the American Ceramic Society* **88**, 3211 (2005).
30. K. Amezawa, Uchimoto, Y., Tomii, Y., *Solid State Ionics* **177**, 2407 (2006).
31. G. Zhang, Yu, R., Vyas, S., Stettler, J., Reimer, J. A., Harley, G., De Jonghe, L. C., *Solid State Ionics* **178**, 1811 (2008).
32. G. Zhang, Wang, R., De Jonghe, L. C., *Solid State Ionics* **180**, 941 (2009).
33. G. Zhang, Yu, R., De Jonghe, L. C., *Solid State Ionics* **217**, 34 (2012).
34. R. S. Hay, Marshall, D. B., *Acta Materialia* **51**, 5235 (2003).
35. G. M. Begun, Beall, G.W., Boatner, L.A., Gregor, W.J., *Journal of Raman Spectroscopy* **11**, 273 (1981).

References for Chapter 3

1. W. Weppner, Huggins, R. A. , *Annual Reviews of Materials Science* **8**, 269 (1978).
2. G. J. Dudley, Steele, B. C. H., *Journal of Solid State Chemistry* **31**, 233 (1980).
3. H.-I. Yoo, Lee, C.-E., *Solid State Ionics* **180**, 326 (2009).
4. T. Norby, *Solid State Ionics* **28-30**, 1586 (1988).
5. M. Liu, *Journal of the Electrochemical Society* **144**, 1813 (1997).
6. M. Sanders, O'Hayre, R., *Journal of Materials Chemistry* **20**, 6271 (2010).

7. K. D. Kreuer, Schonherr, E., Maier, J., *Solid State Ionics* **70-71**, 278 (1994).
8. R. A. De Souza, Kilner, J. A., Walker, J. F. , *Materials Letters* **43**, 43 (2000).
9. J. Feng, personal communication, (2012).
10. G. Harley, Yu, R., De Jonghe, L.C. , *Solid State Ionics* **178**, 769 (2007).
11. H. L. Ray, Zhao, N., De Jonghe, L. C., *Electrochimica Acta* **78**, 294 (2012).
12. G. Zhang, Yu, R., Vyas, S., Stettler, J., Reimer, J. A., Harley, G., De Jonghe, L. C., *Solid State Ionics* **178**, 1811 (2008).
13. N. Adelstein, Neaton, J.B., Asta, M., De Jonghe, L.C., *Journal of Materials Chemistry* **22**, 3758 (2012).
14. G. Harley, Kreuer, K. D., Maier, J., De Jonghe, L. C., *Journal of Non-Crystalline Solids* **355**, 932 (2009).
15. J. E. Bauerle, *Journal of Physics and Chemistry of Solids* **30**, 2657 (1969).
16. J. Fleig, *Solid State Ionics* **150**, (2002).
17. K. D. Kreuer, *Chem. Mater.* **8**, 610 (1996).
18. N. Kitamura, Amezawa, K., Tomii, Y., Hanada, T., Yamamoto, N., Omata, T., Otuska-Yao-Matsuo, S., *Journal of the Electrochemical Society* **152**, A658 (2005).
19. K. Amezawa, Maekawa, H., Tomii, Y., Yamamoto, N., *Solid State Ionics* **145**, 233 (2001).
20. R. R. Heikes, Ure, R. W., *Thermoelectricity: Science and Engineering*. (Interscience Publishers, New York, 1961).
21. H. L. Tuller, Nowick, A. S., *J. Phys. Chem. Solids* **38**, 859 (1977).
22. P. M. Chaikin, Beni, G., *Physical Review B* **13**, 647 (1976).
23. M. R. Peterson, *Phys. Rev. B* **76**, (2007).
24. P. Marsh, *Physical Review B* **54**, (1996).
25. J. Nell, Wood, B. J., Dorris, S. E., Mason, T. O., *Journal of Solid State Chemistry* **82**, 247 (1989).

References for Chapter 4

[1] N. Kitamura, Amezawa, K., Tomii, Y., Hanada, T., Yamamoto, N., Omata, T., Otsuka-Yao-Matsuo, S., *Journal of the Electrochemical Society* **152**, (2005) A658.
[2] E. Gómez del Moral, Fagg, D. P., Chinarro, E., Abrantes, J. C. C., Jurado, J. R., Mather, G. C., *Ceramics International* **35**, (2009) 1481.
[3] D. Stauffer, *Physics Reports (Review Section of Physics Letters)* **54**, (1979) 1.
[4] D. Stauffer, Anthony, A., *Introduction to Percolation Theory*. (Taylor & Francis, London, ed. 2, 1992).
[5] A. L. Efros, Shklovskii, B. I. , *Physica Status Solidi (b)* **76**, (1976) 475.
[6] J. P. Clerc, Giraud, G., Laugier, J. M., Luck, J. M., *Advances in Physics* **39**, (1990) 191.
[7] T. Norby, Christiansen, N., *Solid State Ionics* **77**, (1995) 240.
[8] T. Norby, *MRS Bulletin* **34**, (2009) 923.
[9] K. Amezawa, Kjelstrup, S., Norby, T., Ito, Y., *Journal of the Electrochemical Society* **145**, (1998) 3313.
[10] K. Amezawa, Maekawa, H., Tomii, Y., Yamamoto, N. , *Solid State Ionics* **145**, (2001) 233.
[11] K. Amezawa, Nishikawa, Y., Tomii, Y., Yamamoto, N., *Journal of the Electrochemical Society* **152**, (2005) A1060.

[12] S. Gallini, Hansel, M., Norby, T., Colomer, M. T., Jurado, J. R., *Solid State Ionics* **162-163**, (2003) 167.
[13] N. Kitamura, Amezawa, K., Tomii, Y., Yamamoto, N., *Solid State Ionics* **162-163**, (2003) 161.
[14] N. Kitamura, Amezawa, K., Tomii, Y., Hanada, T., Yamamoto, N., *Solid State Ionics* **176**, (2005) 2875.
[15] G. Harley, Yu, R., De Jonghe, L. C., *Solid State Ionics* **178**, (2007) 769.
[16] R. Yu, De Jonghe, L. C., *Journal of Physical Chemistry C* **111**, (2007) 11003.
[17] J. G. Pepin, Vance, E. R., *J. Inorg. Nucl. Chem* **43**, (1981) 2807.
[18] J. E. Bauerle, *Journal of Physics and Chemistry of Solids* **30**, (1969) 2657.
[19] J. Fleig, *Solid State Ionics* **150**, (2002) 181.
[20] R. S. DeBiasi, Fernandes, A. A. R., Oliveira, J. C. S., *J. Appl. Cryst.* **20**, (1987) 319.
[21] N. Clavier, Podor, R., Dacheux, N., *Journal of the European Ceramic Society* **31**, (2011) 941.
[22] M. Berbon, Davis, J. B., Marshall, D. B., Housley, R. M., Morgan, P. E. D., *International Journal of Materials Research* **12**, (2007) 1244.
[23] H. Takahashi, Unemoto, A., Amezawa, K., Kawada, T., *Solid State Ionics* **192**, (2011) 275.
[24] T. Harter, *Physical Review E* **72**, (2005) 026120.
[25] L. J. Duckers, *Physics Letters* **67A**, (1978) 93.
[26] L. Kurzawski, Krzysztof, M., *Mathematical Physics* **arXiv:1111.3254v2**, (2011).

References for Chapter 5

1. H. L. Ray, Zhao, N., De Jonghe, L. C., *Electrochimica Acta* **78**, 294 (2012).
2. D. M. Smyth, *The Defect Chemistry of Metal Oxides*. (Oxford University Press, Oxford, 2000).
3. C. Wagner, Schottky, W., *Z. Phys. Chem. B* **11**, 163 (1930).
4. C. Wagner, *Z. Phys. Chem. B* **21**, 25 (1933).
5. M. Liu, in *Proceedings of the First International Symposium on Ionic and Mixed Conducting Ceramics,* T. A. Ramanarayanan, Tuller, H. L., Ed. (The Electrochemical Society, Inc., Pennington, N.J., 1991), vol. 91-12.
6. I. Riess, *J. Phys. Chem. Solids* **47**, 129 (1986).
7. M. Liu, *Journal of the Electrochemical Society* **144**, 1813 (1997).
8. L. Li, Iglesia, E., *Chemical Engineering Science* **58**, 1977 (2003).
9. K. L. Duncan, Lee, K.-T., Wachsman, E. D., *Journal of Power Sources* **196**, 2445 (2011).
10. N. Adelstein, Neaton, J.B., Asta, M., De Jonghe, L.C., *Journal of Materials Chemistry* **22**, 3758 (2012).
11. J. Solomon, Adelstein, N., Asta, M., De Jonghe, L. C. , *Electrochemical Society Transactions*, (2012).
12. K. Toyoura, Hatada, N., Nose, Y., Tanaka, I., Matsunaga, K., Uda, T., *J. Phys. Chem. C* **116**, 19117 (2012).
13. N. Adelstein, personal communication, (2012).
14. J. Feng, personal communication, (2012).